Doctoral Dissertation

Emerging Optical Functionalities through Direct Coupling between Quantum Dots and Metal–Organic Frameworks

（量子ドットと金属有機構造体の直接接合による新規光学的機能の開発）

Kohei Kumagai

April 2021

Department of Applied Chemistry

Graduate School of Engineering,

Osaka University

Preface

The studies presented in this thesis were carried out during 2016-2021 under the guidance of Professor Dr. Susumu Kuwabata at Department of Applied Chemistry, Graduate School of Engineering, Osaka University.

The object of this thesis is to develop a novel category of optical nanocomposite by directly bonding semiconductor quantum dots and metal–organic frameworks without using buffer layers between them. It involves exploring the variety of functionality of quantum dot newly emerged by the direct coupling with the framework.

The author strongly wishes that the finding obtained in this work will contribute the development of quantum dot-based applications that is essential to achieve Sustainable Development Goals.

Kohei Kumagai

Department of Applied Chemistry,
Graduate School of Engineering,
Osaka University
Suita, Osaka,
Japan

March 2021

List of Publications

1. Direct surface modification of semiconductor quantum dots with metal–organic frameworks

   Kohei Kumagai, Taro Uematsu, Tsukasa Torimoto, Susumu Kuwabata*

   CrystEngComm, **2019**, *21*, 5568–5577

   DOI: 10.1039/c9ce00769e

2. Photoluminescence Enhancement by Light Harvesting of Metal–Organic Frameworks Surrounding Semiconductor Quantum Dots

   Kohei Kumagai, Taro Uematsu*, Tsukasa Torimoto, Susumu Kuwabata*

   Chem. Mater. **2021**, *33*, 1607–1617

   DOI: 10.1021/acs.chemmater.0c03367

3. Variations in Photoluminescence Intensity of a Quantum Dot Assembly Investigated by its Adsorption on Cubic Metal–Organic Frameworks

   Kohei Kumagai, Taro Uematsu*, Tsukasa Torimoto, Susumu Kuwabata*

   J. Phys. Chem. C. **2021,** *in press*

List of Supplementary Publications

4. Epoxy-Containing Ionic Liquids with Tunable Functionality

   Tetsuya Tsuda*, Kazuki Iwasaki, Kohei Kumagai, Susumu Kuwabata

   Molecules, **2019**, *24(14)*, 2591.

   DOI: 10.3390/molecules24142591

Contents

General Introduction

From ultra-high resolution displays (4K, 8K) to high-speed optical communication, the importance of fundamental technologies for manipulating light is more and more increasing. Above all, semiconductor nanoparticles (NPs), or quantum dots (QDs), have attracted much attention as the next generation of light-emitting materials owing to the unique optical properties, which are different from organic dyes and rare earth phosphors.[1, 2] Firstly, the energy band structure of QDs peculiar to semiconductors allows to absorb light over a wide wavelength range (Figure I-a). Then, since electrons and holes generated by light irradiation are confined in a very small space, they proceed recombination with high probability to emit photoluminescence (PL) with a narrow emission linewidth corresponding to the band gap (Figure I-b). Of course, the energy gap of the QDs is tunable by changing their particle size or composition, covering visible to near infrared regions (Figure I-c).[3-5] In terms of emission intensity, almost unity PL quantum

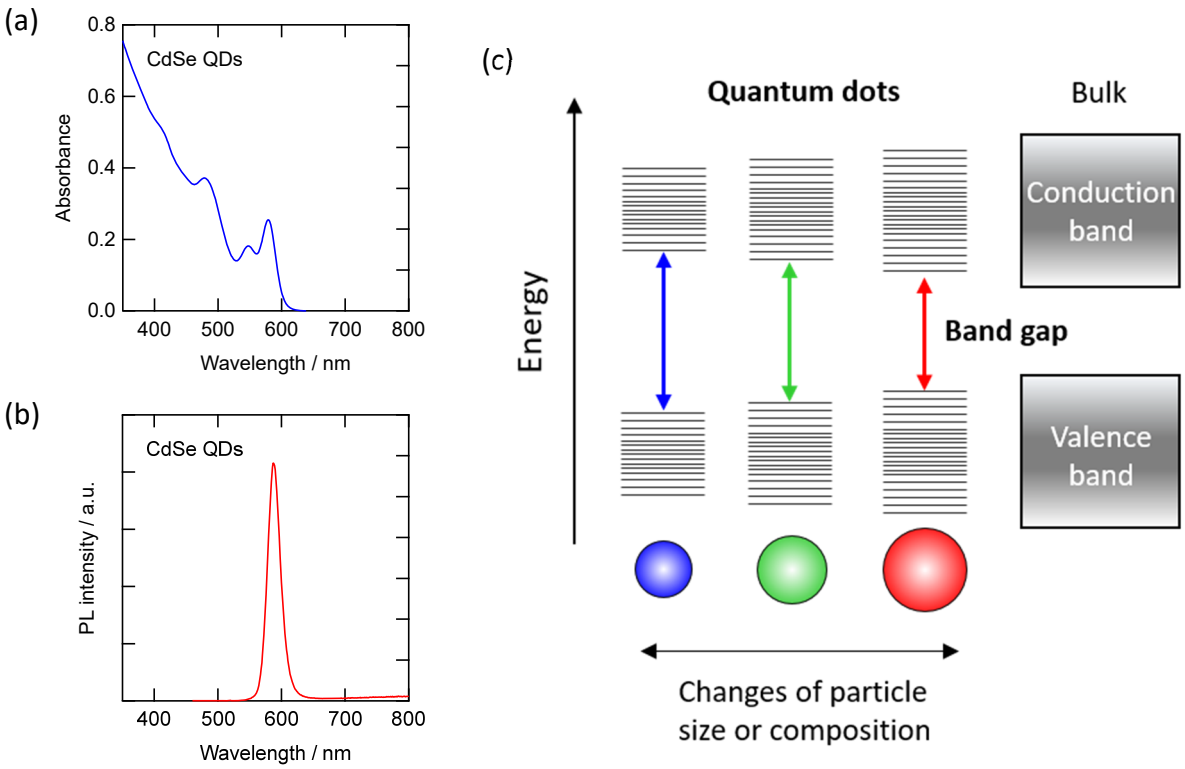

Figure I. UV−vis (a) and PL (b) spectra of octadecylphosphonic acid-capped CdSe QDs. Schematic illustration of energy band gap tuning of QDs depending on their size and composition (c).

yield (QY) has been reported by coating core QDs with an appropriate inorganic materials to form the core/shell structure.[6, 7] Owing to the above superior optical properties, QDs have been put to practical use in various fields such as fluorophores used in biomarkers[8, 9] and wavelength converters for liquid-crystal displays.[10, 11] In addition, their uses in severer conditions such as luminescent solar concentrators[12] and quantum dot light-emitting diodes are planned and investigated enthusiastically.[13-15]

Previous studies on the relationships between electronic structure and optical properties of QDs have revealed that an entire nanoparticle structure including a core, shell, and surface ligands is involved with the optical properties, and even a small variation to the structure possibly bring a significant change to its PL QY (Figure II).[3] Such a high susceptibility to surface conditions is not completely released even when the core is covered by inorganic shells,[16, 17] which demonstrates a necessity for further understanding of outermost ligands to make future optoelectronic devices promising. However, as QDs with high PL QY are demonstrated by limited types of ligands, such as oleylamine and oleic acid, giving further functionalities to the QDs by this method is difficult. That is, the use of other category of coordinating compounds as stabilizers should be considered.

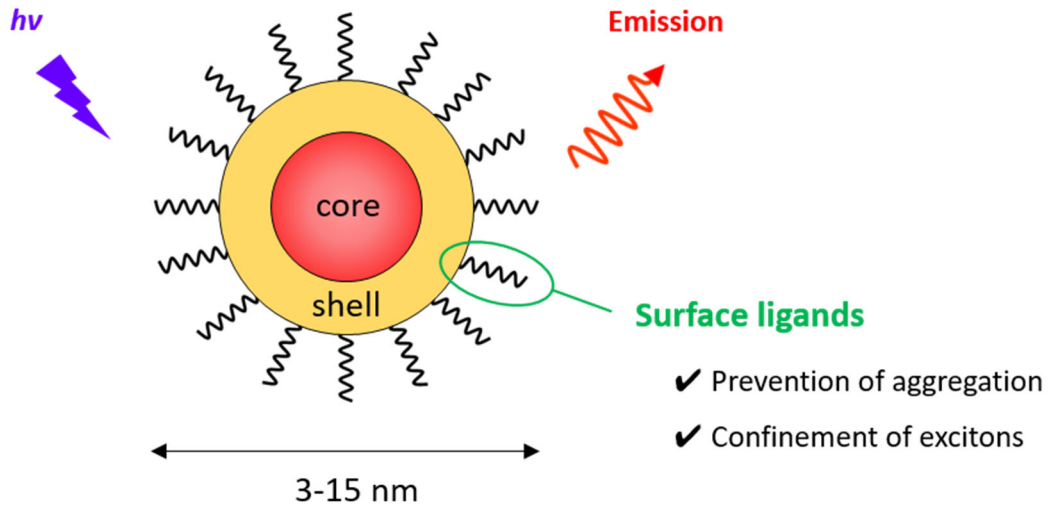

Figure II. Schematic illustration of highly fluorescent core/shell QDs in practical use.

Metal–organic frameworks (MOFs), or porous coordination polymers (PCPs), are a new class of microporous crystalline materials with infinite lattices formed by the self-assembly of unit structures (Figure III). The unit structure is called as secondary building unit (SBU) and usually consists of metal cations, salts, or clusters and polydentate organic ligands that are coordinating to them.[18, 19] Owing to the versatile architecture and adjustable functionality derived from the numerous combination of the components, more than 20,000 different types of MOFs have so far been reported, and some of them are even commercially available from the manufactures of chemical reagent.[20] In contrast to the conventional porous materials like active carbons and zeolites, the pore size and functionality can be systematically tuned by changing the length of organic linkers and/or introducing various organic groups (e.g. –Br, -NH_2, -OC_3H_7).[21] One of the most promising applications of MOFs is a selective absorption of gases relating to an energy production (CO_2, H_2, and CH_4) or those harmful to human or catalysts (CO and NH_3) using unprecedentedly high surface area and pore volume present in their structure with a strict control over size.[22] Furthermore, the usability of MOFs is not limited to such gas storage and separation,

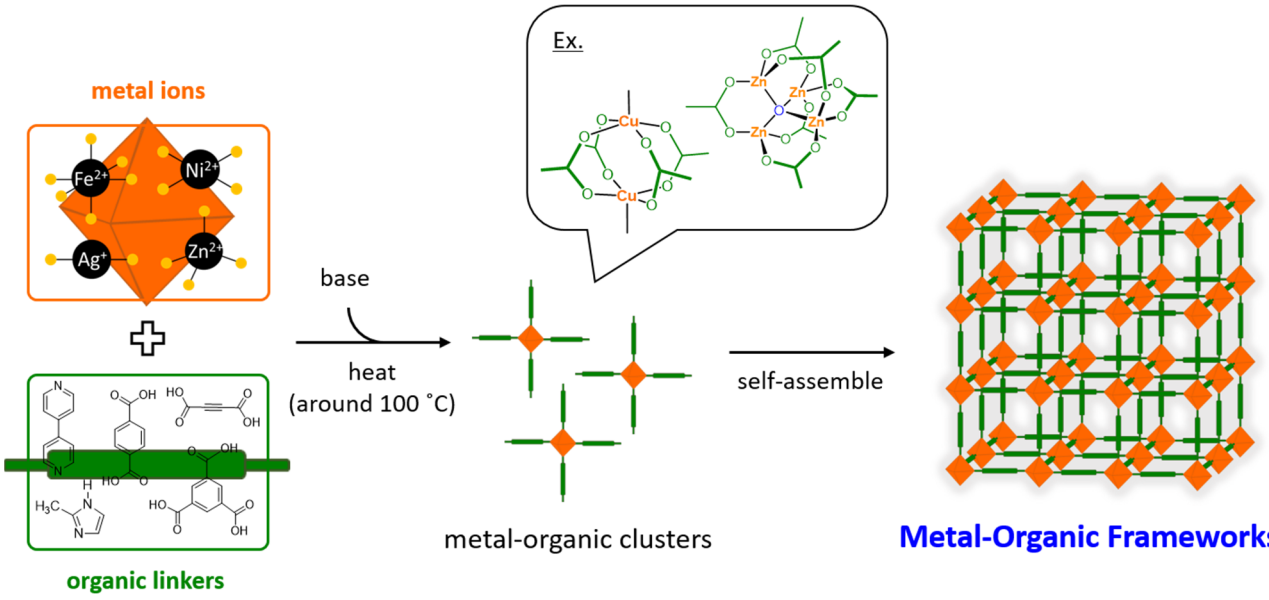

Figure III. Schematic illustration of MOFs synthesized by combining metal ions and organic

but they are promising for the use as catalysts and templates in the mass production of nanostructures.[23-26] Fabrication of the drug delivery systems is also promising because some of the MOFs having relatively large pore size can accommodate molecules whose size are larger than aforementioned gas molecule.[27] Even electron-conducting MOFs can be fabricated depending on the choice of metals as nodes and molecules as linkers.[28]

In fact, QDs and MOFs have many similarities with each other in their structure: for example, both two types of materials maintain their structure whose size is more than a few nanometers by the coordination bond of carboxyl and amino groups and other heterocyclic molecules to zinc, copper, indium and other metal cations. In addition, such coordination bonds have an important role to determine the functions. This means that there are varieties of synergetic effects expected by creating QDs/MOFs composites. In the beginning, the fast and easy crystal growth of MOFs is favorable to obtain thick overlayers on the surface of QDs, which can be used as a protecting layer, too, if the overlayer is grown to encapsulate the QDs. At the same time, the structural flexibility of the end groups of MOFs expectedly helps the bonding between the two materials, which is contrasting with the coating by inorganic materials (core/shell structure in the conventional meaning) that need special cares on crystal phase and size matching.[29] When it comes to the functionalization by making composites, an emergence of new photocatalytic activities and photoluminescence properties is expected due to energy and electron transfer between the two materials because some of the MOFs have been reported to serve as light harvesting materials.[30, 31]

When thinking about a method to make composites of MOFs and nanoparticles including QDs, there are two different approaches that are friendly called as “ship in a bottle” and “bottle around the ship” approaches (Figure IV).[32] In the former case, small molecules or metal complexes incorporated in MOFs are reacted to grow nanoparticles, and the particle sizes are

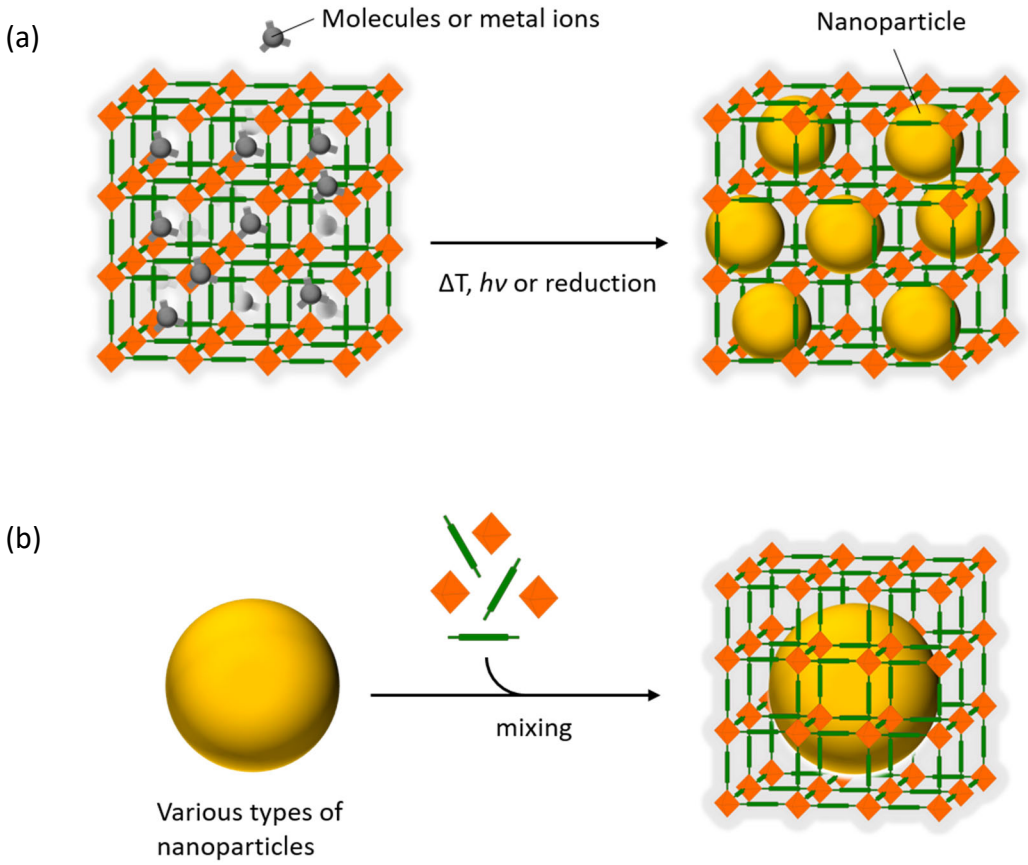

Figure IV. Schematic illustration of main approaches for the fabrication of nanoparticles/MOFs core/shell composites, named as "ship in a bottle" (a), and "bottle around the ship" (b).

restricted by the cavities of frameworks (Figure IV-a). Metal nanoparticles (e.g. Pd, Co, Au, Cu, Mg)[33-36], semiconductor core QDs (CdSe, CdTe)[37, 38], and lead halide perovskite QDs ($CsPbBr_3$)[39] were synthesized in the cavities of MOFs in mild conditions without causing the decomposition of the MOFs. However, the incorporated nanoparticles have a limitation of volume (less than one cavity of the MOF), and complex structures like the core/shell structure cannot be generated due to the restrictions on the reaction conditions that can be used without destroying the structure of the host MOF. On the other hand, the latter, the bottle around the ship approach, is the method that use nanoparticles as nucleation centers, i.e., heterogeneous nucleation of MOFs, after which crystals of the MOFs are grown further (Figure IV-b). This approach allows the incorporation of various types of nanoparticles including metals, oxides,

polymers, carbons, and core/shell semiconductor QDs into MOFs.[40-50] However, in exchange for the freedom of material selection, either polymers or long-chain organic linkers needed to be sandwiched between MOFs and nanoparticles to improve the adhesion between the two materials.

Although these attempts using buffer layers were successful in the development of beautiful composites whose TEM images have been reported in several early papers, the lack of descriptions on functionality acquired by the complex formation in these papers anticipates the need for more direct connection between QDs and MOFs. Actually, an attempt by H. Kitagawa *et al*. to cover palladium nanocubes with a copper-based MOF (HKUST-1) was done by using weakly adsorbing ligands for palladium nanocubes rather than using them as a buffer layer.[51] In such conditions, the two materials were partially in contact, and such an environment allowed the charge transfer from the Pd nanocube to the MOF. In consequence, they reported the doubling of hydrogen storage characteristics.[52] Similar synergetic effects are expected for the composite of QDs and MOFs, because the PL properties of QDs are very susceptible to the surface conditions that can expectedly be transformed into unprecedented situation by binding with MOF.

Present work

In the present study, I develop a new category of optical nanocomposite by directly bonding semiconductor QDs and MOFs without using buffer materials between them, which is one of the greatest features of this research. The strategy is to bind the multidentate linker molecules of MOFs directly with QDs, demonstrating an ideal environment to facilitate synergetic effects. The key technology to demonstrate the growth of MOFs on QDs are the optimization of the surface ligands of QDs whose binding force is sufficiently strong to keep them dispersed but weak enough not to interfere with the linker molecules of MOFs to bind. This approach is successful to obtain QD/MOF core/shell composite, in which the MOF shell as large as 50 nm thickness firmly protects the QDs in place of inorganic materials and also enhances the PL intensity of the QDs by a light harvesting function according to the selection of MOFs as shells. In addition, a very strong adsorptive force is found between the ligand-exchanged QDs and certain types of preformed MOFs. By using this side effect, a new system to understand the photochemical aspects of QD assembly is fabricated by making an ideal two-dimensional assembly of QDs on a cubic MOF.

Chapter 1 describes a new strategy for developing an ideal QDs/MOFs core/shell structure in which the two types of the materials are directly in contact. As an initial attempt, ZIF-8, one of the representative MOFs possessing a high structural stability and a large HOMO–LUMO gap (>5.5 eV) is selected as a robust protecting material for QDs. The gradual growth of the ZIF-8 crystal from the surface of QDs is visually confirmed by TEM observation. Complete inclusion of QDs in ZIF-8 is confirmed by tilted TEM images in which QDs always locate at the center of the structure and the fact that PL quenching does not occur when an electron acceptor is added.

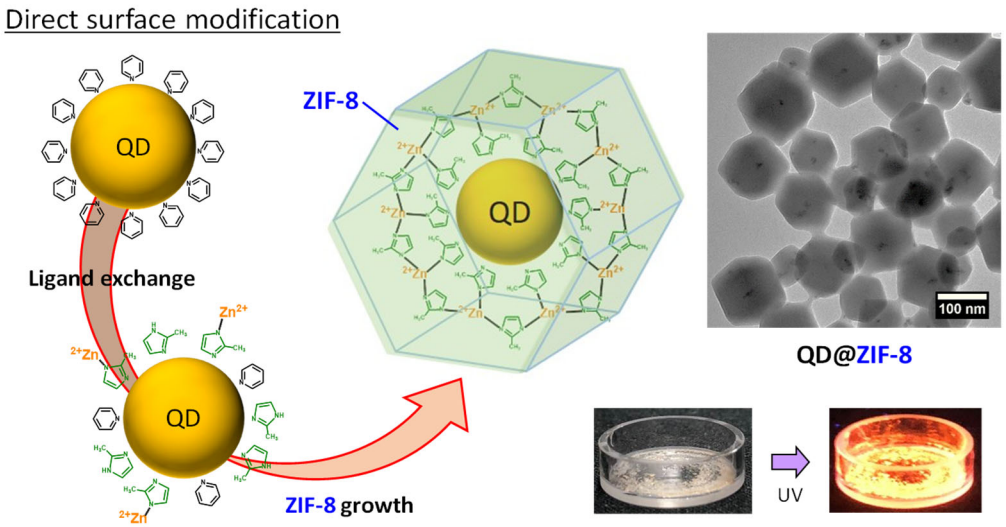

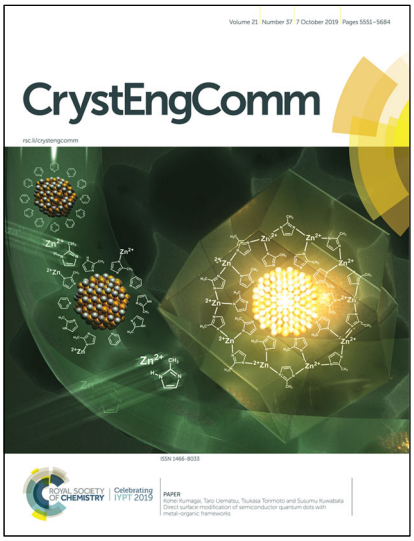

Chapter 2 describes an efficient energy transfer from the photoluminescent MOF (IRMOF-3) to the QDs in QD/MOF core/shell composites similar to that described in Chapter 1. The efficiency of energy transfer in QD/IRMOF-3 core/shell composites is discussed based on the theory of Förster resonance energy transfer (FRET), and it is compared with another system having a different three-dimensional configuration (QD-supported IRMOF-3).

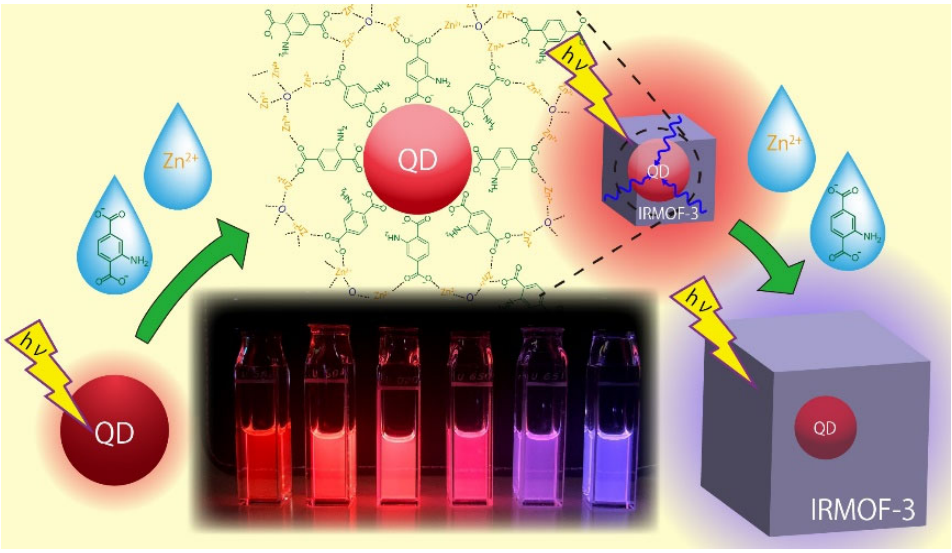

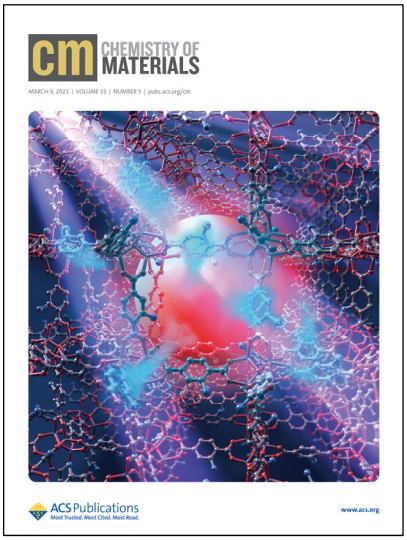

Chapter 3 describes the development of a new system to investigate the energy transfer between QDs in close distance by using a strong adsorptive force working between QDs and MOFs. Either a single type of QDs or a mixture of different types of QDs are mixed with a preformed nanosized cubic crystals of MOF-5 to make two-dimensional array of the QDs on the MOFs. Photoluminescence intensity variations, when different amounts of the QDs are loaded on the MOFs, are discussed in relation to the occurrence of hetero- and homo-FRET. The results predict that the presence of non-emissive particles decreases the PL intensity of QDs assembly more than their abundance ratio due to the crosstalk between the assembled QDs.

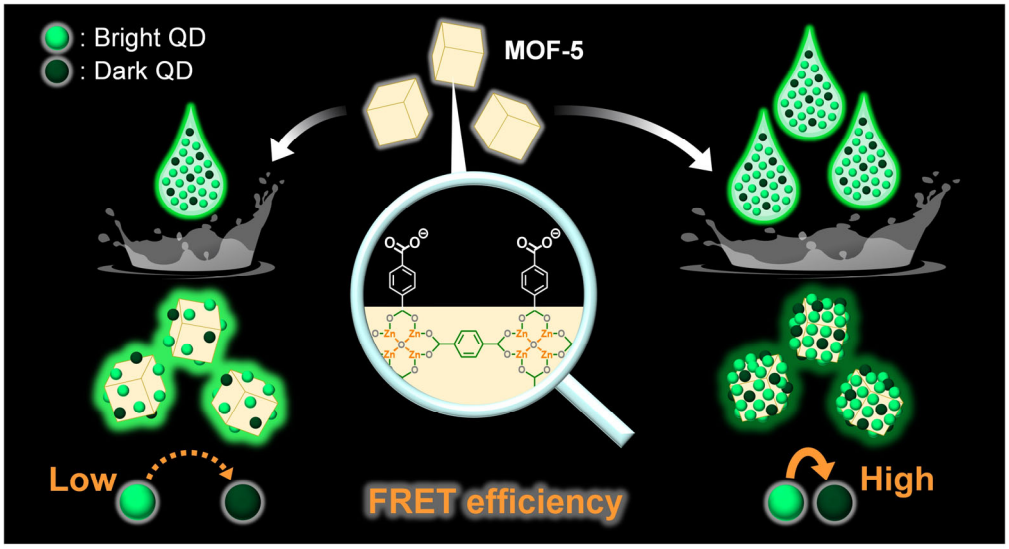

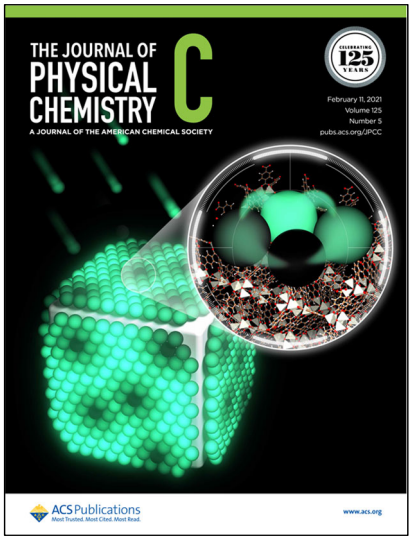

Chapter 1

Metal–Organic Frameworks as Novel Surface Stabilizers for Semiconductor Quantum Dots

1-1. Introduction

QDs are spreading in a wide range of fields such as displays and lighting, and are one of the important materials that support our daily lives. However, in order to be comparable and to compete with common rare-earth phosphors, the durability of QDs against oxygen, moisture, light and heat must be improved.[53-55] The instability against slight changes in the external environment comes from the band structure of semiconducting materials, in which photoexcited carriers are delocalized over the particle of nearly 10 nm in diameter. Especially, outermost organic ligands play an important role to prevent the oxidization and corrosion of the QD surfaces, while satisfying the good dispersibility in solvents. However, most of the surfactants are weakly coordinated to the surface atoms on QDs, thus easily altered or damaged in the process of introducing optoelectronic devices.[56, 57] As a result, surface trap sites are generated inside the band gap, and photoluminescence quenching usually occurs. Variation in their PL intensity cannot be easily avoided by core/shell structure unless shells are exceptionally thick (>10 nm), which is known to have a giant shell.[58] Therefore, the development of robust and easily grown surface protective materials for the QDs, which take the place of conventional organic surfactants, is important to further develop QD-based optical and optoelectronic applications. One of the promising candidates for surface stabilizers is an insulating MOF, which is easily grown on the surface of QDs owing to its structural flexibility derived from its organic component. If QDs are embedded with a MOF of sufficient thickness, it is expected that the stability of QDs against changes in the external environment must be dramatically improved.

In this study, I explored the possibility of MOFs as new classes of surface protecting materials for

fluorescent QDs. CdSe/CdS core/shell QDs were attempted to be covered by zeolitic imidazolate framework-8 (ZIF-8) through a direct link between the two without using any auxiliary substances that act as scaffolds or buffer layers. ZIF-8 is known as a material with relatively high thermal and chemical stability among MOFs, which is advantageous to use QDs in harsh conditions such as wavelength conversion materials in white LED.[59] In addition, a rapid room-temperature production of nanocrystals (finely tuned in size between ~10 and 65 nm) and microcrystals (~1 μm) has been reported by J. Cravillon *et al*.[60] Direct contact between QDs and a ZIF-8 modifier seems to be easily achieved, considering that imidazole derivatives (organic linkers of ZIF materials) are working as electron-donating ligands for QDs.[61]

Here, a new strategy for developing a QD/MOF core/shell composite is proposed without any bonding materials between the QD and MOF like polymers (Fig. 1-1). Firstly, the native ligand (oleylamine) of the QDs was exchanged for pyridine in advance of the covering reaction by ZIF-8. The pyridine-capped QDs underwent a ligand exchange in situ with 2-methylimidazole, one of the components of ZIF-8, during the reaction. By controlling the concentration of ZIF-8 precursors in the reaction media, nearly monodispersed ZIF-8 crystal was grown directly on the surface of CdSe/CdS core/shell QDs. The QDs were observed to be fully incorporated into the ZIF-8 crystal and were photoluminescent with a solid-state PL QY as high as 40%.

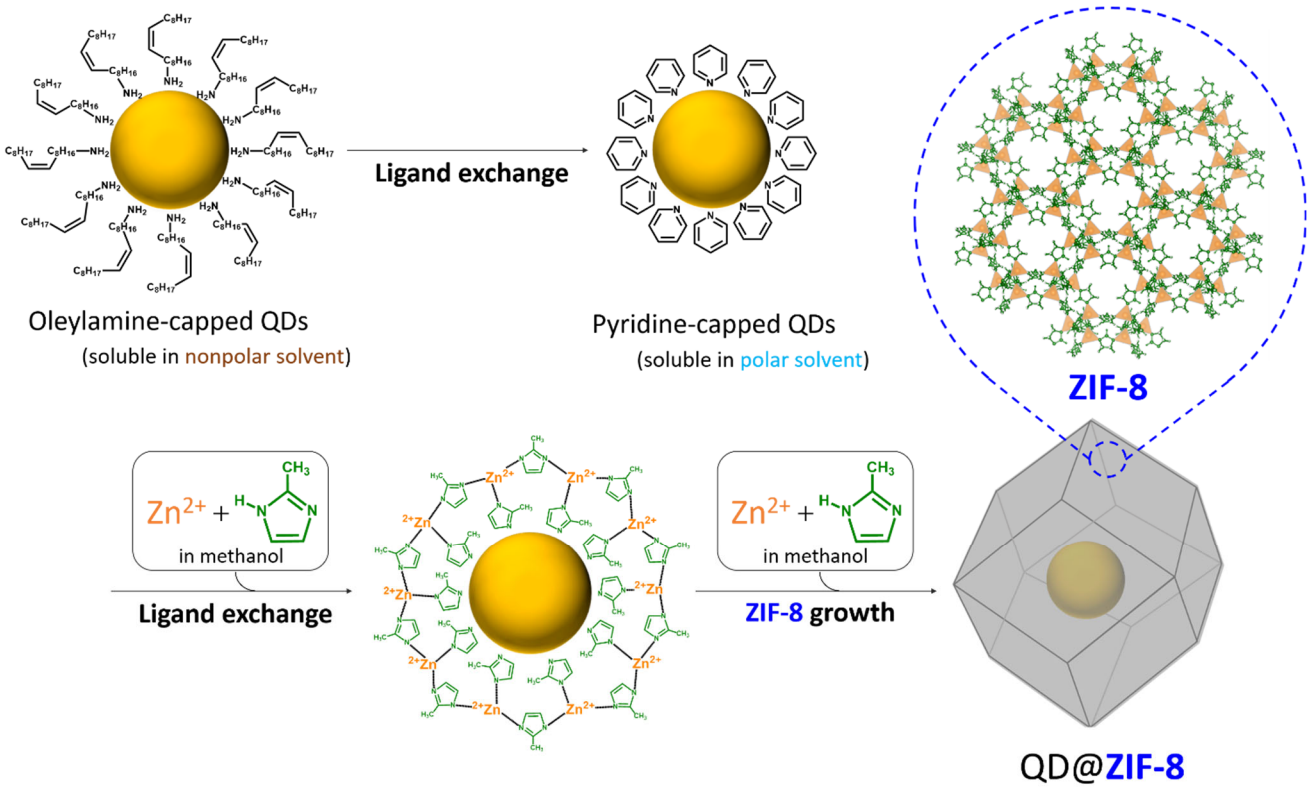

Figure 1-1. Schematic illustrations for the growth process of QD@ZIF-8 composite. ZIF-8 crystal is grown directly on the metal site of QDs.

1-2. Experimental section

1-2-1. Materials

Stearic acid (HSt), cadmium acetate dihydrate ($Cd(Ac)_2 \cdot 2H_2O$), sodium diethyldithiocarbamate trihydrate ($NaDDTC \cdot 3H_2O$), pyridine, zinc nitrate hexahydrate ($Zn(NO_3)_2 \cdot 6H_2O$), and *1,4*-benzoquinone were purchased form Wako Pure Chemical Industries and used without further purification. Tetramethylammonium hydroxide pentahydrate, 1-octadecene (ODE), octylamine, tributylphosphine (TBP), dodecane, and 2-methylimidazole were purchased from TCI. Selenium powder (Se) was purchased from Nacalai Tesque. 4-*tert*-Butylpyridine was purchased from Aldrich. Oleylamine (Wako) was purified by vacuum distillation in the presence of calcium hydride. Cadmium stearate ($Cd(St)_2$) and cadmium diethyldithiocarbamate ($Cd(DDTC)_2$) were synthesized using a procedure reported by X. Peng *et al.*[6]

1-2-2. Synthesis of CdSe/CdS core/shell QDs

Briefly, $Cd(St)_2$ (0.271 g, 0.4 mmol), HSt (0.569 g, 2 mmol), and ODE (8 mL) were mixed in a two-necked flask and evacuated at 80 °C for 30 min. The temperature was then increased to 240 °C under an Ar atmosphere and maintained for 10 min. Selenium powder (0.0316g, 0.4 mmol) dispersed in ODE (2 mL) was swiftly injected into the flask, and the temperature was held at 220 °C for 5 min before cooling to room temperature. The orange CdSe QDs solution was obtained and an excess amount of acetone was added to the solution to precipitate the QDs. The suspension was centrifuged, and the solid QDs were re-dispersed into chloroform.

For each CdS shell growth reaction, a 5 mL of $Cd(DDTC)_2$-amine-octane solution (0.1 M) was prepared by dissolving of $Cd(DDTC)_2$ (0.122 g, 0.3 mmol) in a mixture of octane (1.5 mL), oleylamine (0.45 mL), and octylamine (1.05 mL). In a two-necked flask, 100 nmol of CdSe QDs in a chloroform

solution (1.27 mL), dodecane (2 mL), octylamine (1.7 mL), and oleylamine (0.5 mL) were evacuated at 60 °C for 30 min. The temperature was then increased to 80 °C under Ar and maintained for 10 min. The 0.1 M solution of $Cd(DDTC)_2$-amine-octane solution (0.26 mL) was injected into the flask, and the temperature was increased to 140 °C at a rate of 10 °C/min and then maintained for 10 min. The flask was then cooled to 80 °C, and the second precursor solution was added. The procedures were repeated three times to obtain four monolayers of CdS shell. The amount for three consecutive injections of the $Cd(DDTC)_2$-amine-octane solution was calibrated as 0.34, 0.44, and 0.56 mL, respectively. An excess amount of acetone was added to the solution to precipitate the QDs. The suspension was centrifuged, and the solid QDs were re-dispersed into chloroform.

1-2-3. Ligand exchange of QDs

The CdSe/CdS QDs were precipitated by the addition of methanol and dispersed in pyridine. The suspension was heated to 100 °C and stirred for 3 h in a pressure tube (Aldrich). After the suspension became clear, the solution was cooled to room temperature, and an excess of hexane was added to precipitate the QDs. The solid QDs obtained by centrifugation were re-dispersed in pyridine. The ligand exchange to 4-*tert*-butylpyridine was done with the same procedure by using 4-*tert*-butylpyridine instead of pyridine.

1-2-4. Synthesis of QD@ZIF-8 composite by instantaneous mixing

Pyridine-capped CdSe/CdS QDs solution (0.5 nmol in terms of particle) were diluted with methanol (25 mL), and methanolic solutions of $Zn(NO_3)_2 \cdot 6H_2O$ (4 mM, 10 mL) and 2-methylimidazole (40 mM, 10 mL) were added simultaneously into the QDs solution. The mixture was vigorously stirred for 1 h at room temperature, during which small portions were taken for optical measurements and TEM observations. The residual solution was incubated at

room temperature for another 24 h. The precipitate in the solution was recovered by filtration, washed with methanol, and dried under reduced pressure.

1-2-5. Synthesis of QD@ZIF-8 composite by dropwise addition

Pyridine-capped or 4-*tert*-butylpyridine-capped CdSe/CdS QDs solution (0.5 nmol in terms of particle) was diluted with methanol (25 mL), and methanolic solutions of $Zn(NO_3)_2 \cdot 6H_2O$ (4 mM, 10 mL) and 2-methylimidazole (40 mM, 10 mL) were separately prepared as a precursor for ZIF-8. The precursor solutions were injected into the QDs solution at a rate of 10 mL/h using two sets of syringes operated by a syringe pump at room temperature. Portions of the suspension were taken intermittently during the injection and submitted to optical measurements and TEM observations. The suspension was stirred for another 24 h at room temperature, and then the QD@ZIF-8 composites were recovered by filtration, washed with methanol, and, finally, dried under reduced pressure.

1:1 QD@ZIF-8 composite was synthesized in further dilute conditions. 4-*tert*-Butylpyridine-capped CdSe/CdS QDs solution (0.025 nmol in terms of particle) was diluted with methanol (25 mL), and methanolic solutions of $Zn(NO_3)_2 \cdot 6H_2O$ (4 mm, 1.0 mL) and 2-methylimidazole (40 mm, 1.0 mL) were separately prepared as a precursor for ZIF-8. The precursor solutions were injected into the QDs solution at a rate of 10 mL/h using two sets of syringes operated by a syringe pump at room temperature. Portions of the suspension were taken intermittently during the injection and submitted to optical measurements and TEM observations.

1-2-6. PL quenching tests of fluorescent QDs and QD@ZIF-8 composite

The QDs solution and QD@ZIF-8 composite suspension were diluted with methanol to be 70 nM (in terms of particle). The solutions or suspensions were mixed with 1,4-benzoquinone (~100 μM) in a 1 × 1 cm quartz cuvette and PL intensity variations were measured.

1-2-7. Characterization

UV-vis and PL spectra were recorded with a spectrometer (JASCO, V-670) and fluorospectrometer (Horiba Jobin Yvon, Fluoromax-4), respectively. Photoluminescence QY was measured by a spectrometer equipped with an integrating sphere (Hamamatsu, PMA-12). TEM images were taken by a Hitachi H-7650 TEM with an acceleration voltage of 100 kV using a carbon coated copper grid. X-ray diffraction (XRD) patterns were recorded using a Rigaku Ultima IV operating at 40 kV and 40 mA with Cu Kα radiation. Thermogravimetric analyses (TGA) were performed using Bruker TG-DTA2000SA. Samples were placed on alumina crucibles and heated from room temperature to 800 °C at a rate of 5 °C min^{-1} under air flow. Particle sizes in solutions were estimated with a dynamic light scattering (DLS) instrument (Otsuka Electronics, ELAZ-2000ZS).

1-3. Results and discussion

1-3-1. Structural characterization of core/shell QDs

Figures 1-2a and 2c show TEM images of CdSe QDs and CdSe/CdS core/shell QDs, respectively, and the corresponding UV-vis and PL spectra are shown in Fig. 1-2b and 2d. The average diameter of the nanoparticles was increased from 3.85 nm to 5.85 nm by the CdS shell formation, leading to a redshift in their photoluminescence and improvement of the PL quantum yield (QY) from 1.5% to 60%. The values of full width at half maximum for the PL peaks were 36 nm for both CdSe and CdSe/CdS core/shell QDs, indicating that the monodispersity of the QD ensembles was unchanged after shell formation.

Figures 1-2e and 2f show TEM images and optical spectra of the CdSe/CdS QDs after the ligand exchange reaction. As often seen in TEM images of pyridine-capped QDs, a substantial decrease in the interparticle distance was observed after ligand exchange. The shapes of absorption and emission spectra before (Fig. 1-2d) and after (Fig. 1-2f) the ligand exchange were mostly identical, whereas PL QY decreased from 60% to 19%, due to the partial aggregation of QDs,[62] and/or the hole-leaking from CdSe QDs to the pyridine ligand over the CdS shell.[63] Nevertheless, the ligand exchange to pyridine is indispensable for the growth of ZIF-8, not only because it is an easily removable weak base ligand (even weaker than 2-methylimidazole) but also because methanol, which is commonly used for the synthesis of ZIF-8, is highly compatible with pyridine-capped QDs.

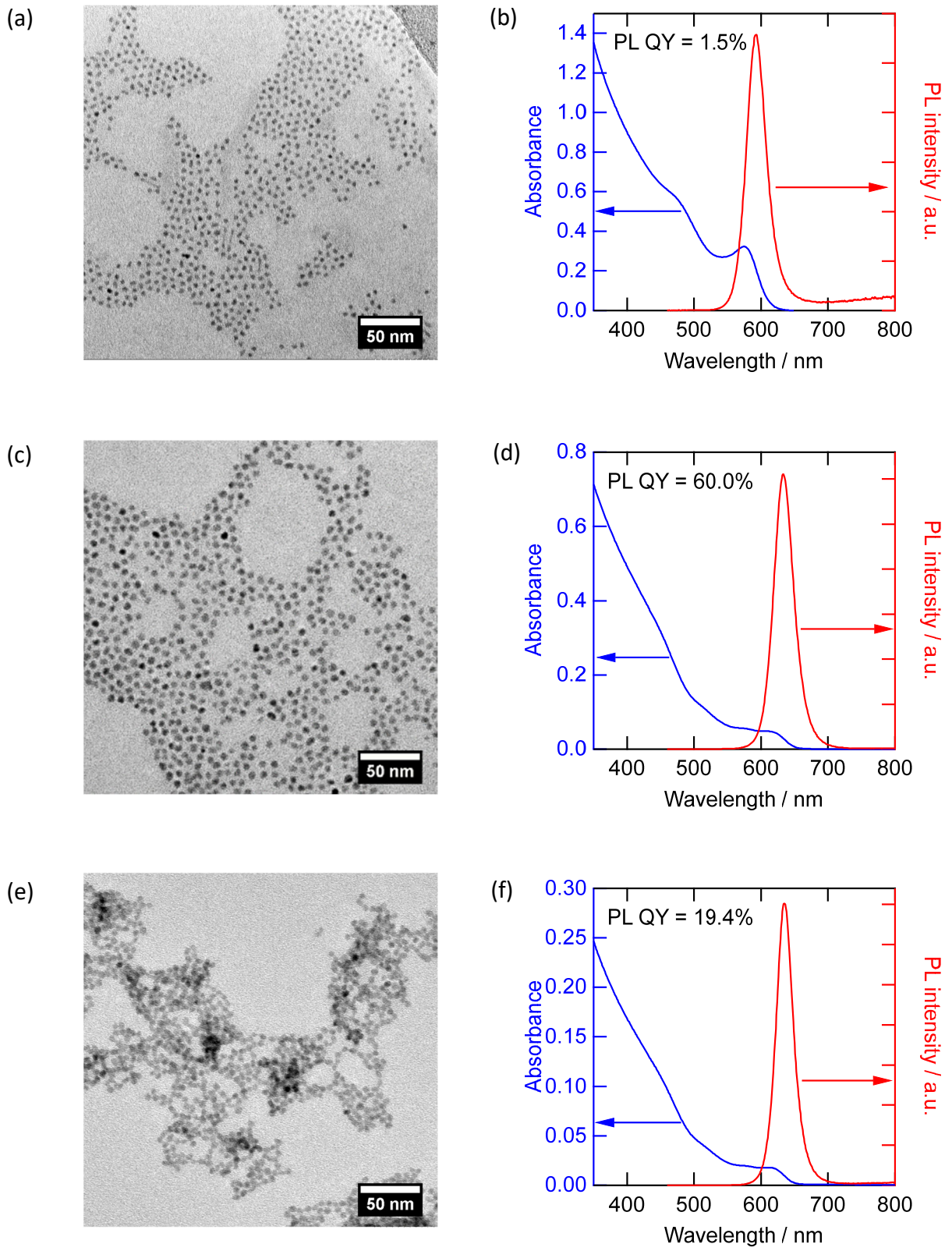

Figure 1-2. TEM images (a), UV−vis and PL spectra (b) of stearic acid-capped CdSe QDs. TEM images (c, e), UV−vis and PL spectra (d, f) of CdSe/CdS core/shell QDs stabilized by oleylamine (c, d) and pyridine (e, f). The excitation wavelength was 450 nm for all PL spectra.

1-3-2. Surface modification of QDs by ZIF-8

Figure 1-3a shows UV-vis absorption spectra of the reaction solution recorded at different timepoint after methanolic solutions of $Zn(NO_3)_2 \cdot 6H_2O$ (4 mM, 10 mL) and 2-methylimidazole (40 mM, 10 mL) were instantaneously mixed with the pyridine-capped CdSe/CdS QDs solution (25 mL containing 0.5 nmol of particles). The reaction solution remained clear after stirring for 1 h, indicating that ZIF-8 crystals have not enoughly grown nor were there QD aggregates large enough to produce light scattering (Fig. 1-3a, inset picture). The TEM image (Fig. 1-3b) shows many spherical objects with a diameter of around 20 nm that exist apart from the QDs displayed as smaller dark spots. Most likely, the instantaneous mixing of the ZIF-8 precursors causes an immediate nucleation of ZIF-8 particles with a consumption of most precursors, resulting in generation of only smaller ZIF-8 particles.[60] With this in mind, we suspect that the rate of ligand exchange from pyridine to 2-methylimidazole was slower than the homogeneous nucleation of ZIF-8, and consequently most of the QDs were not incorporated into the ZIF-8 crystals, but

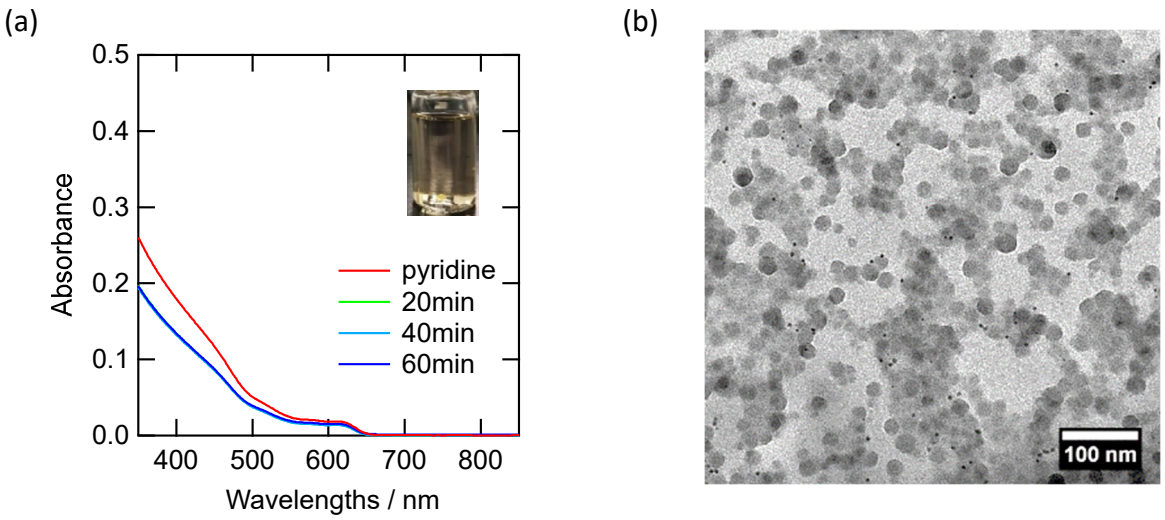

Figure 1-3. UV-vis spectra recorded at different timepoint during the synthesis of CdSe/CdS QD@ZIF-8 composites (a), and TEM images corresponding to the samples of 60 min (b). ZIF-8 precursors were immediately mixed with pyridine-capped CdSe/CdS QDs solution. The inset pictures are photographs at 60 min.

rather just adsorbed onto the ZIF-8 surface. On the other hand, if the stirring was stopped after 1 h, the transparent solution gradually became opaque due to the spherical ZIF-8 undergoing aggregation with involving the QDs around (Fig. 1-4a and 4b).

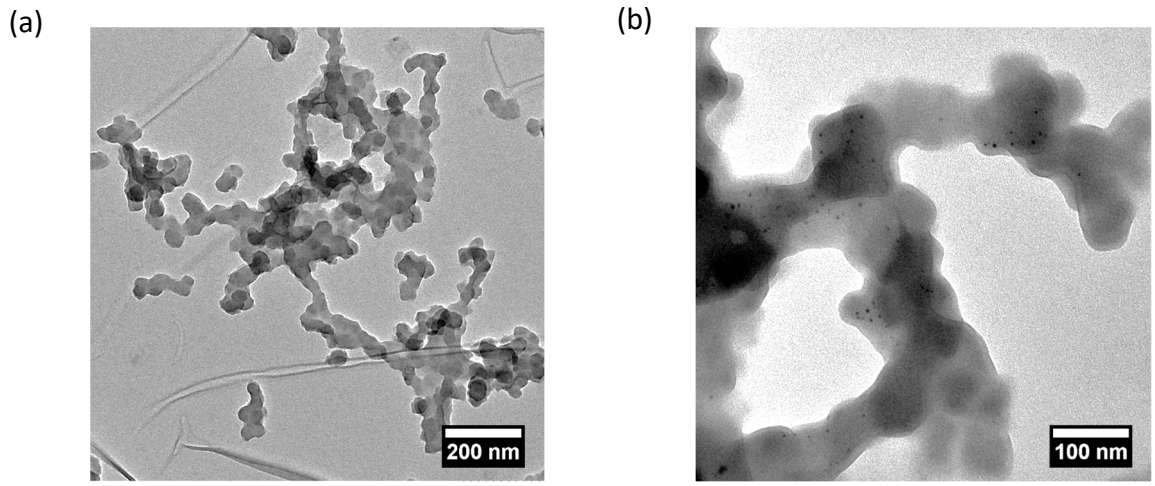

Figure 1-4. TEM images of QD@ZIF-8 composites: overall (a) and magnified (b) images. Samples were synthesized by immediately mixing ZIF-8 precursors with pyridine-capped CdSe/CdS QDs solution.

A simple but very reliable strategy to facilitate the epitaxial growth of ZIF-8 on the surface of QDs, without homogeneous nucleation of ZIF-8, is to keep the concentrations of ZIF-8 precursors low during the reaction. Fig. 1-5a shows time-course UV-vis absorption spectra when the methanolic solutions of $Zn(NO_3)_2 \cdot 6H_2O$ (4 mM, 10 mL) and 2-methylimidazole (40 mM, 10 mL), which is equal amount and concentration as used for the instantaneous mixing, were added dropwise to the pyridine-capped CdSe/CdS QDs solution (25 mL, 0.5 nmol) simultaneously using two sets of syringes over 60 min.

In contrast to instantaneous mixing, the reaction solution became cloudy during the early stages of the injection (ca. 20 min), and its opaqueness increased in proportion to the amount of precursors added. As a matter of fact, the absorption tail at longer wavelengths (>650 nm) arising from light scattering by the ZIF-8 crystals steadily increased with time as shown in Fig. 1-5a.

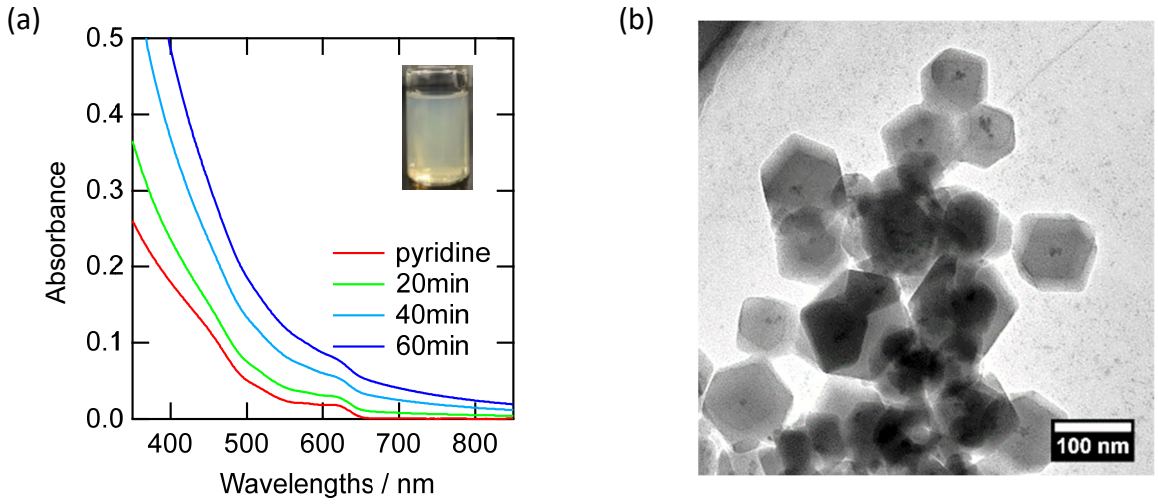

Figure 1-5. UV-vis spectra recorded at different timepoint during the synthesis of CdSe/CdS QD@ZIF-8 composites (a), and TEM images corresponding to the samples of 60 min (b). ZIF-8 precursors were synthesized by dropwise addition. The inset pictures are photographs at 60 min.

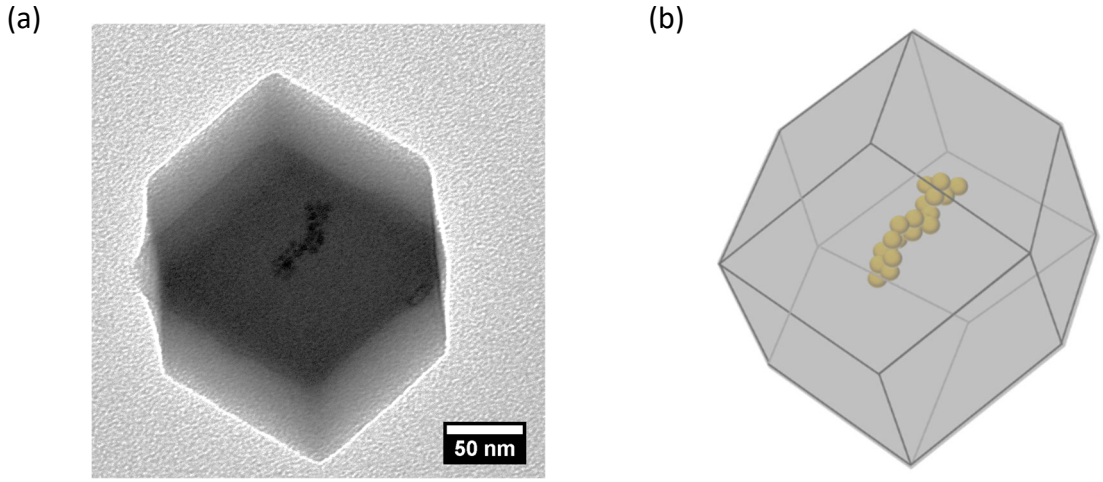

Figure 1-6. TEM images (a) and schematic illustration (b) of CdSe/CdS QD@ZIF-8 composite.

The TEM image obtained after the completion of the dropwise injection (Fig. 1-5b) clearly shows the existence of ZIF-8 crystals in a 100 nm scale that incorporates the CdSe/CdS core/shell QDs at their centers. A well-defined, rhombic dodecahedron with 12 surfaces indicates the ZIF-8 crystals have a high crystallinity.[60] However, the embedded QDs are comprised of 5–15 particles that likely aggregated before or during the embedding reaction (Fig.

1-6). ZIF-8 crystals without QDs embedded, and QDs that were not covered with ZIF-8, were not found over the entire observation field of the TEM grid. Thus, we hypothesize that the QDs served as seed crystals for the ZIF-8 to grow. The powdery QD@ZIF-8 composite (prepared by both the instantaneous mixing and the dropwise injection) were isolated by filtration, and XRD patterns were measured. As shown in Fig. 1-7, both samples showed patterns that coincide with the ZIF-8 reference (ICDD 062-1030, ZIF-8). Each peak in the powder XRD was narrower for the composite synthesized by the dropwise injection than by the instantaneous mixing, indicating that controlled growth produced samples with high crystallinity. The absence of signals from QDs are rational since volumetric ratio (ZIF-8/QDs) expected from the amount of raw materials was ca. 400, and since the short crystal length of QDs (<5.8 nm) broadened their signals.

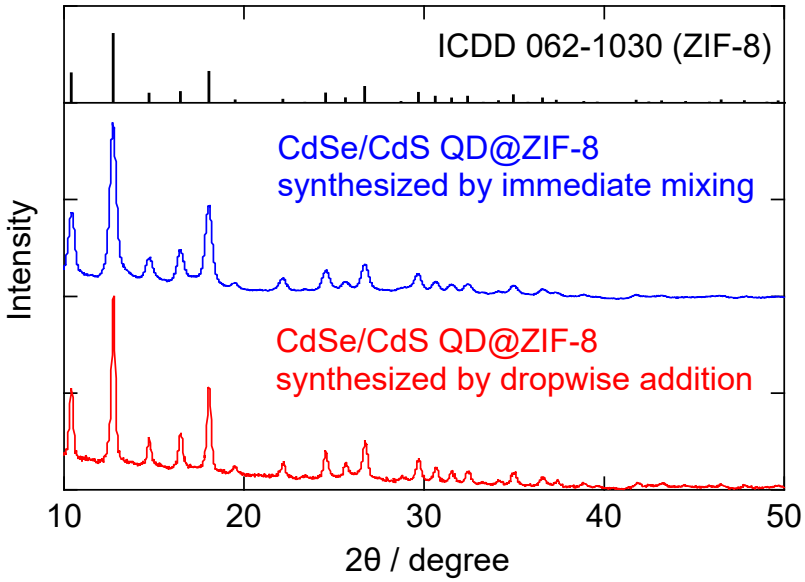

Figure 1-7. PXRD patterns of CdSe/CdS QD@ZIF-8 composites synthesized by immediately mixing or dropwise addition.

The TGA curves for pure ZIF-8 and the CdSe/CdS QD@ZIF-8 composite revealed that both of them had a high thermal stability up to 350 °C (Fig. 1-8). Small weight losses below that temperature may be deriving from the removal of methanol and 2-methylimidazole trapped in the cavities. The total weight loss of ZIF-8 between 350 °C and 600 °C was 63%, which was almost same as the calculated value (64%) assuming conversion of ZIF-8 to ZnO in air. On the other hand, the weight loss of CdSe/CdS QD@ZIF-8 composite was slightly smaller (59%) than the pure ZIF-8, indicating the existence of QDs that may remained unchanged or partly converted to CdO.

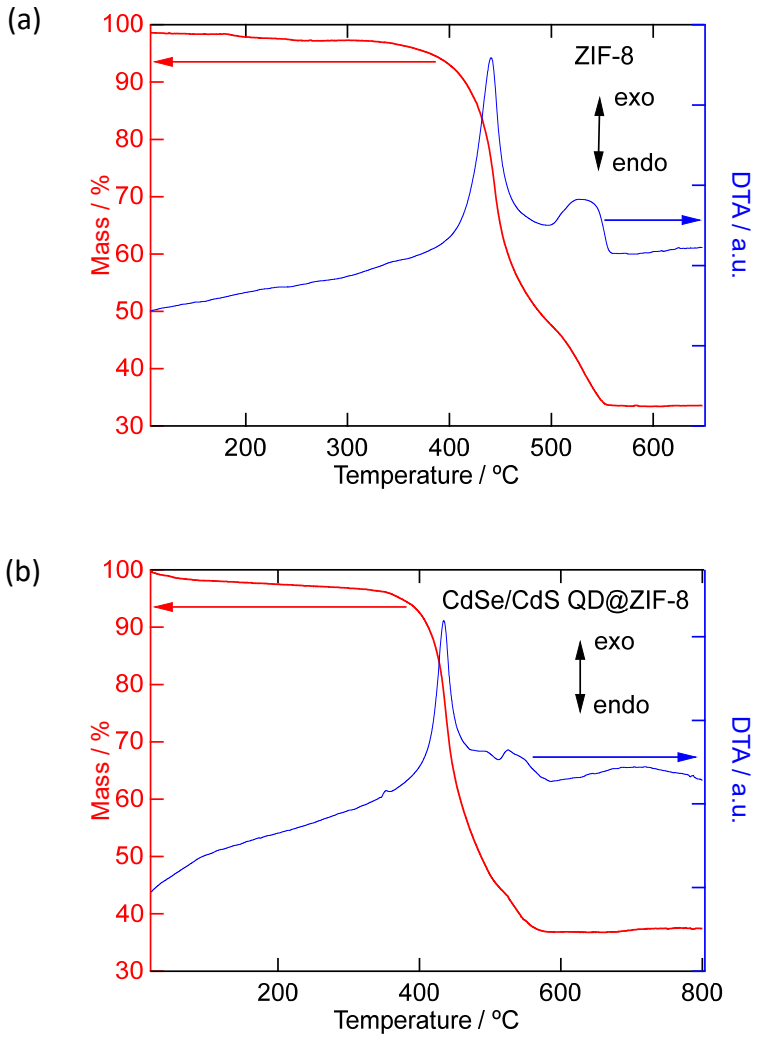

Figure 1-8. TG (red lines) and DTA curves (blue line) of ZIF-8 (a) and CdSe/CdS QD@ZIF-8 composite synthesized by dropwise addition.

Figure 1-9a shows PL spectra (normalized at PL maxima) of CdSe/CdS QDs before and after being modified by ZIF-8 through the dropwise synthesis. The PL peak shape was unchanged, and a redshift that is mostly observed by inorganic shell formation (CdS and ZnS) was not observed after ZIF-8 modification. That is, no detectable interfacial defects were generated and the large band gap of ZIF-8 (>5.5 eV) functioned well for exciton confinement. Photoluminescence QY decreased from 19% for the pyridine-capped QDs to 11% just after being modified by ZIF-8. However, when the suspension was kept stirred, PL QY was recovered with time, reaching 14% after 3 days and 36% after 3 weeks. Plus, the increase in PL QY was accompanied by a blueshift of the PL peak by ca. 5 nm (Fig. 1-9b). The blueshift may originate from the maturation of ZIF-8 structure near QDs surface to provide stronger quantum confinement and/or the rearrangement of molecules and ions at the QD/ZIF-8 solid/solid interface. Especially, if the cation exchange between the zinc in ZIF-8 and the cadmium in the CdS shell occurs, a noticeable change in quantum confinement would happen.[64] It is one of the characteristics of the binder-free approach to modify the surface of QDs by MOFs. Finally, when the sample after 3 weeks was filtered to recover the precipitate, pale orange powder was isolated. The powder emitted strong photoluminescence with the solid-state QY as high as 40% (Fig. 1-9c).

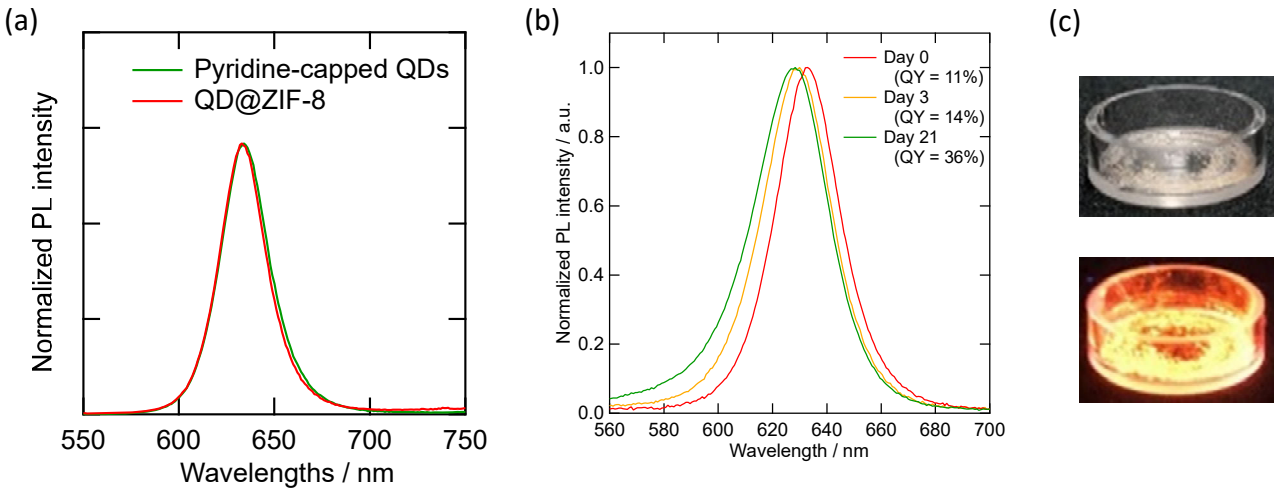

Figure 1-9. PL spectra of CdSe/CdS QDs before and after being embedded in ZIF-8 (a). Normalized PL spectra of CdSe/CdS QD@ZIF-8 composite recorded after the reaction, 3 days, and 3 weeks (b). Photographs of powdery CdSe/CdS QD@ZIF-8 composites under ambient light (upper) and UV light (lower) (c).

1-3-3. Observation of the ZIF-8 growth process from QD surface

In order to investigate the growth process of ZIF-8 crystals around QDs, TEM images of the QD@ZIF-8 composites were taken at different timepoints during the dropwise addition of ZIF-8 precursors (Fig. 1-10, a-d). After 2.5 mL of total (10 mL of each) precursors were introduced, traces of the ZIF-8 crystal were found around partially aggregated CdSe/CdS core/shell QDs (Fig. 1-10a). The shape of the ZIF-8 block was irregular but partially spherical, and some QDs remained uncoated. Presumably, the growth of the ZIF-8 initiated from the QDs surface through the ligand exchange from pyridine to 2-methylimidazole. As the amount of precursor added to the reaction solution was increased, the sizes of the ZIF-8 crystals gradually increased. Fig. 1-10e shows schematic illustrations of the ZIF-8 crystal growth process when more precursors are added to the reaction. After the addition of 5.0 mL of the precursors, most of the QDs were fully covered with ZIF-8 and some larger ZIF-8 crystals became faceted with smaller crystals remaining spherical (Fig. 1-10b). Further addition of raw materials made the ZIF-8 particles larger on average and obviously faceted (Fig. 1-10c), and finally, the structures of ZIF-8 crystals were fully transformed from spherical to rhombic dodecahedron (Fig. 1-10d). The rhombic dodecahedron shape is determined by facets since it is the most stable facet for a ZIF-8 crystal.[65]

In order to further demonstrate that the ZIF-8 growth happens exclusively on the surface of QDs without self-nucleation occurring, a similar experiment was carried out with the total amount of QDs reduced to 1/20th. Fig. 1-11a shows the TEM images of the CdSe/CdS QD@ZIF-8 composite prepared with the standard dropwise procedure (0.5 nmol of QDs with 40 μmol of $Zn(NO_3)_2 \cdot 6H_2O$ and 400 μmol of 2-methylimidazole), whereas Fig. 1-11c shows the composite prepared with 1/20th of the amount of QDs (0.025 nmol of QDs with 40 μmol of $Zn(NO_3)_2 \cdot 6H_2O$ and 400 μmol of 2-methylimidazole). The corresponding size histograms are provided in Fig. 1-11b and 11d, in which the size of the composite prepared using 1/20th of the

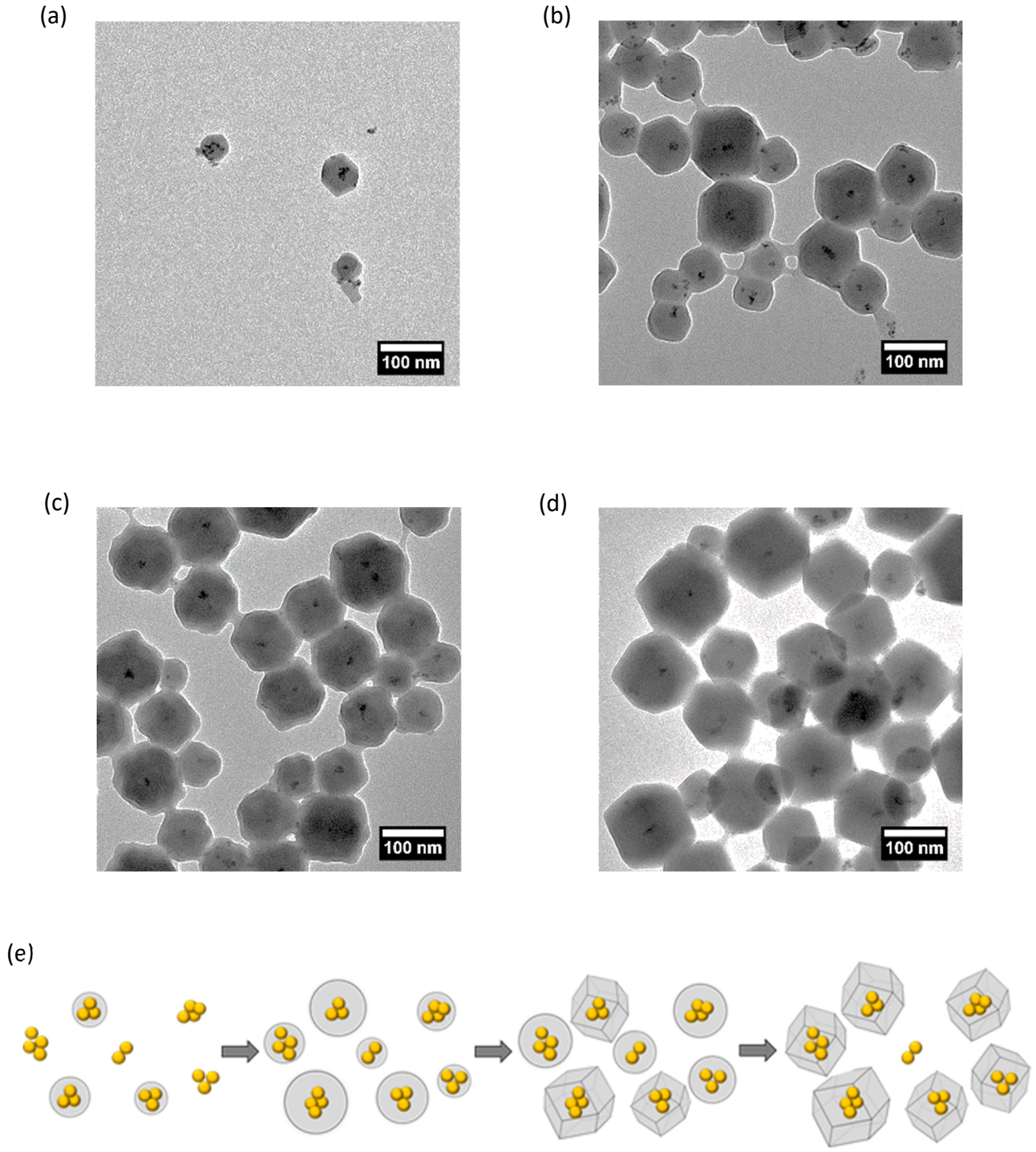

Figure 1-10. TEM images of CdSe/CdS QD@ZIF-8 composites taken at different timepoints during the dropwise addition of ZIF-8 precursors; 2.5 mL (a), 5.0 mL (b), 7.5 mL (c), and 10.0 mL (d). Schematic illustrations for the growth of ZIF-8 on CdSe/CdS QDs (e).

amount of QDs was apparently larger (volume-weighted average diameter, d_{av} = 438 nm) than the samples prepared with the standard condition (d_{av} = 136 nm). Although these data include some inaccuracy arising from the process of measuring the polyhedral object, the three times

difference in average size was found between the two samples. It is comparable to the expected 20 times difference in volume for one ZIF-8 crystal, providing the growth of ZIF-8 preferentially occurred from the QDs serving as seed crystals, when the fundamental relationship between size and volume is considered ($\sqrt{20} \approx 2.7$). On the contrary, when the dropwise addition of ZIF-8 precursors was conducted in the absence of the QDs, even the biggest ZIF-8 crystal was no larger than 200 nm (Fig. 1-11e and 11f). Together, these results indicate that the growth of ZIF-8 happens exclusively on the surface of the QDs when the precursors are added dropwise to the reaction media.

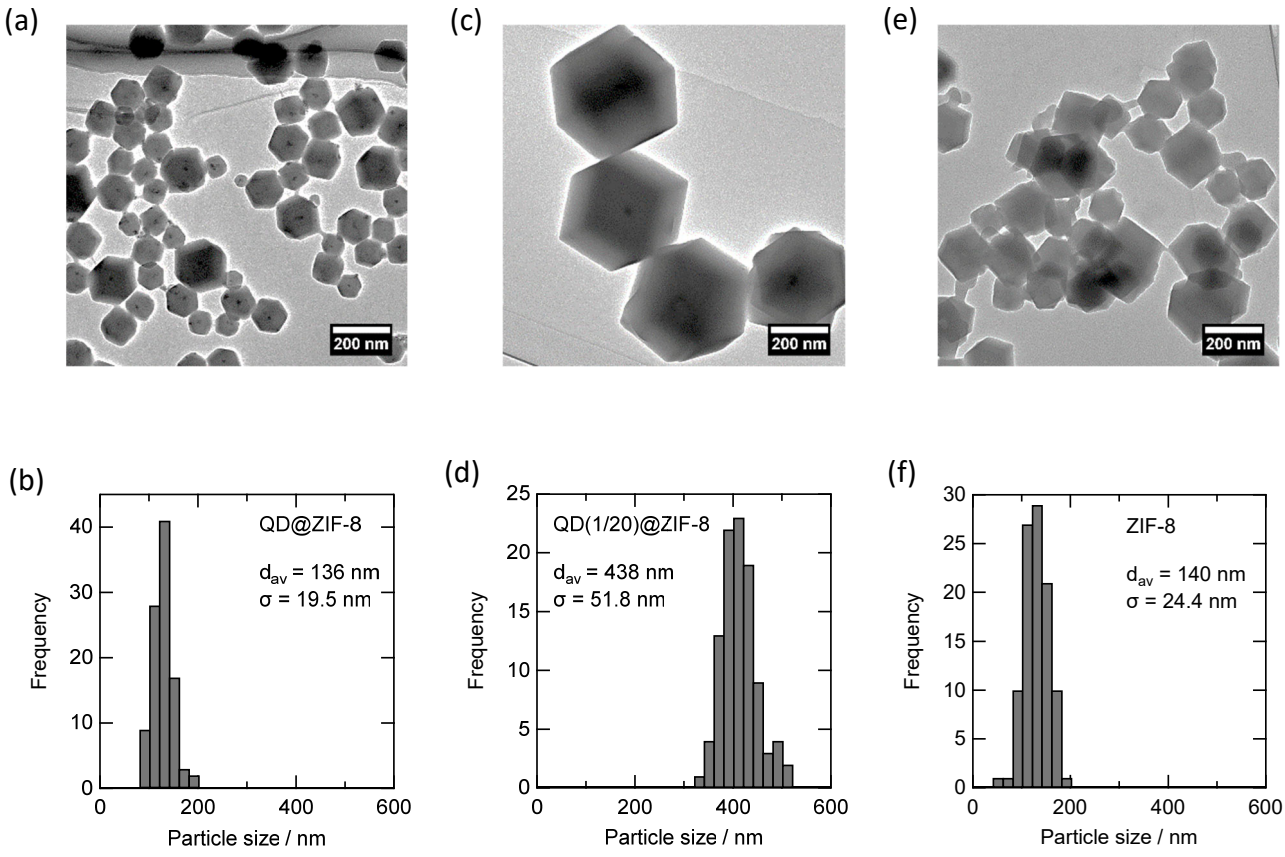

Figure 1-11. TEM images (a, c) and the corresponding size histograms (b, d) of CdSe/CdS QD@ZIF-8 composites prepared with 0.5 nmol (a, b) and 0.025 nmol (c, d) of CdSe/CdS QDs. TEM images (e) and the corresponding size histogram (f) of ZIF-8 synthesized in the absence of QDs.

1-3-4. Synthesis of a single QD-contained composite

Although synthesis of a QD@ZIF-8 composite was achieved without bonding materials between the two species, QDs embedded in the ZIF-8 were mostly agglomerated as shown in Fig. 1-6. Since the agglomeration in the ZIF-8 was not prevented even if the reduced amount of QDs were used for the reaction, we speculated that aggregated QDs were working as seed crystals for ZIF-8 epitaxial growth. To test this hypothesis, the dispersion of pyridine-capped CdSe/CdS QDs in methanol was measured by DLS (Fig. 1-12a). The mean effective diameter of the pyridine-capped QDs was 24.6 nm, substantially larger than 5.8 nm of the mean size of the core/shell QDs even considering that the hydrodynamic size is always larger the actual particle size. These results suggest that the pyridine ligand did not provide enough dispersibility to the core/shell QDs, resulting in agglomeration of the QDs in methanol.

To enhance dispersibility of the QDs and prevent agglomeration, 4-*tert*-butylpyridine was used instead of pyridine. The electron donating group in the para position increases the basicity

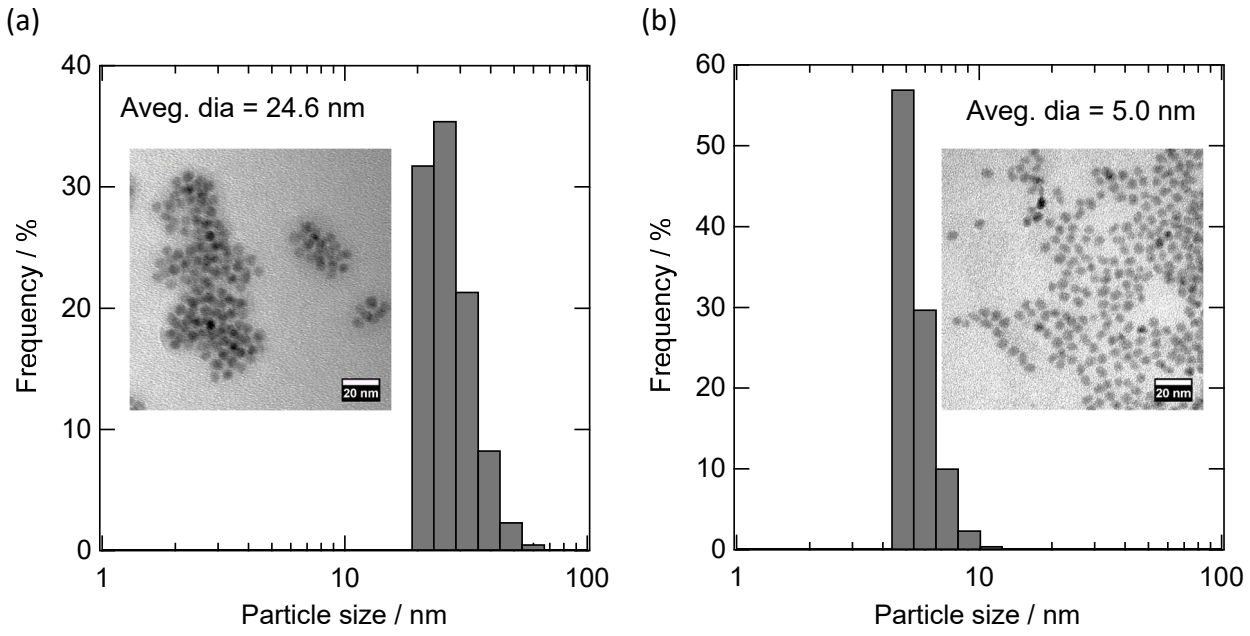

Figure 1-12. Size distribution measured by DLS (in methanol solution) for pyridine-capped (a) and 4-tert-butylpyridine-capped (b) CdSe/CdS QDs. Insets are TEM images of each sample.

of the coordinating pyridine nitrogen to the metal site of the QDs. The *tert*-butyl group also provides flexibility to the end of the QDs that is essential for solubility. As far as we know, there have not been any reports on the use of 4-*tert*-butylpyridine as a capping ligand for QDs, although it has been actively investigated for dye-sensitized solar cells as an electron donating reagent binding to TiO_2 to improve cell performance.[66] Fig. 1-12b shows the size distribution for 4-*tert*-butylpyridine-capped CdSe/CdS QDs in methanol analyzed by DLS. As expected, the new bulkier and more basic ligand greatly improved the dispersibility of QDs in methanol. TEM images in the inset of the Fig. 1-12b also showed an increase in the QDs–QDs distance compared with the pyridine-capped samples (Fig. 1-12a, inset).

Fig. 1-13a shows the TEM image of CdSe/CdS QD@ZIF-8 when 5.0 mL (out of 10 mL) of the precursors was added to 4-*tert*-butylpyridine-capped CdSe/CdS QDs solution by the dropwise method. In contrast to the pyridine-capped QDs used as starting materials (Fig. 1-10b), most of the QDs were separately embedded into the ZIF-8 crystals (Fig. 1-13a). The small portion of QDs partially exposed to the reaction solution at this stage was completely incorporated into the ZIF-8 when 10 mL of the precursor solutions was added to the reaction media (Fig. 1-13b). However, many QDs were still contained into each ZIF-8 crystal, contrary to my expectation that smaller ZIF-8 crystals were generated around each QD. The incorporation of multiple QDs can be explained by the temporal difference of ZIF-8 crystal growth, leading to the incorporation of uncoated QDs into the relatively larger QD@ZIF-8 composite and/or the coalescence between small, nearly spherical QD@ZIF-8 composites that possess higher surface energy. Therefore, the concentration of both QDs and the ZIF-8 precursors were decreased in order to reduce the collision frequency between materials. The synthesis was carried out again with 1/20th of the amount of QDs (0.025 nmol) and 1/10th of the ZIF-8 precursors (4 μmol of $Zn(NO_3)_2{\cdot}6H_2O$ and 40 μmol of 2-methylimidazole). Fig. 1-13c shows the TEM image of the

QD@ZIF-8 composite prepared by the diluted reaction condition. One QD was successfully incorporated into each angular ZIF-8 crystal. In addition, the tilted TEM images by +20° and −20° indicated that the QD was located at the center of the ZIF-8 crystal (Fig. 1-13d). Thus, the initiation of ZIF-8 crystal growth on the surface of QDs and the subsequent isotropic growth was successfully demonstrated.

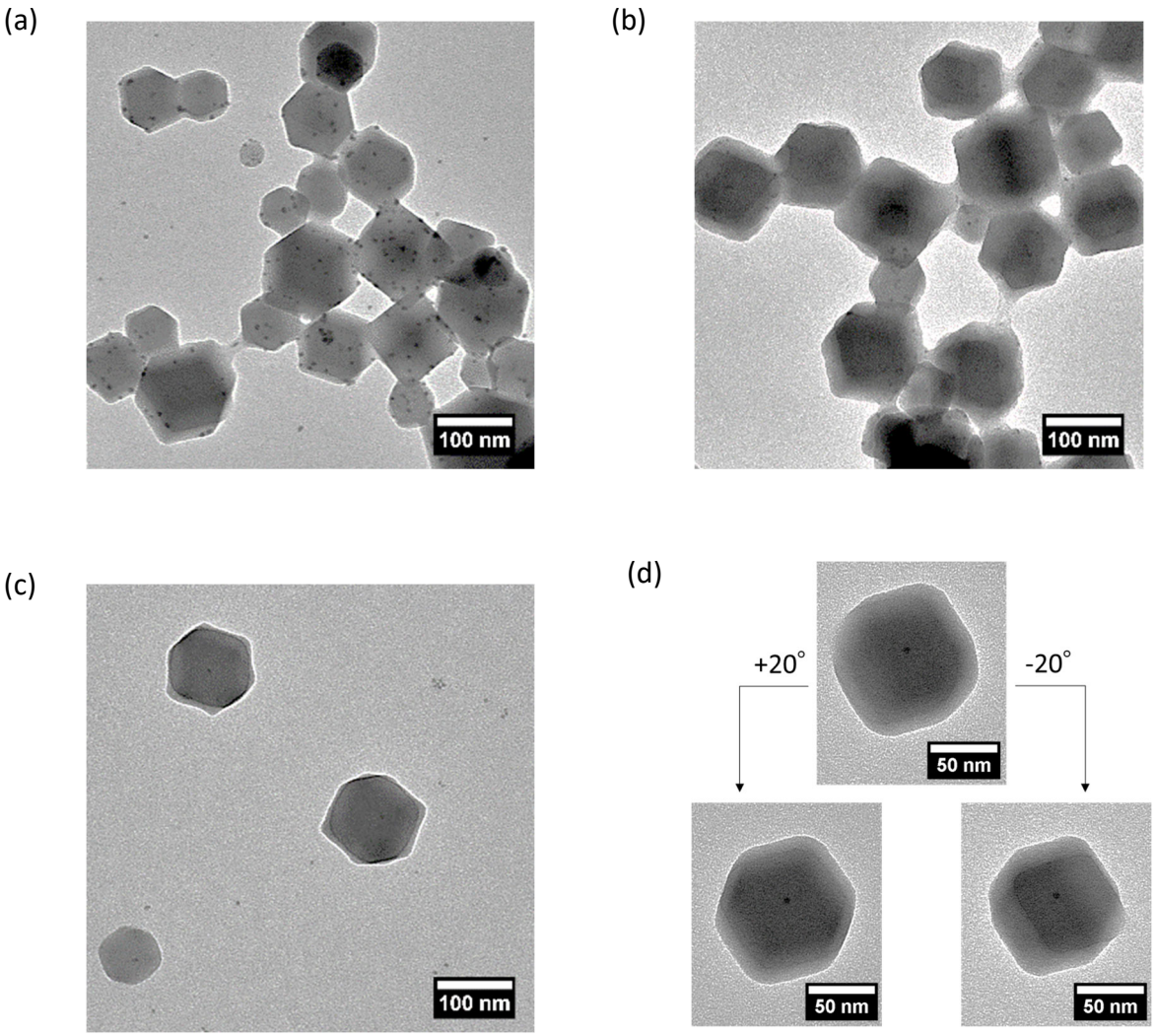

Figure 1-13. TEM images of CdSe/CdS QD@ZIF-8 composites when 5.0 mL (a) and 10.0 mL (b) of the precursors was added to 4-tert-butylpyridine-capped CdSe/CdS QDs solution. TEM images of 1:1 CdSe/CdS QD@ZIF-8 composites prepared by mixing 1.0 mL of the precursor solutions and 1/20th the amount of QDs (c), and the corresponding tilted TEM images (+20˚, 0˚, and -20˚, d).

1-3-5. MOFs as protecting materials for QDs

To evaluate the potential of ZIF-8 as a protecting shell for QDs, *1,4*-benzoquinone, one of the efficient electron acceptors that can quench the PL from both the CdSe core and the CdSe/CdS core/shell QDs, was added to the solution of pyridine-capped CdSe/CdS core/shell QDs as well as a suspension of CdSe/CdS QD@ZIF-8 composite (Fig. 1-5a, inset picture). As shown in Fig. 1-14a, *1,4*-benzoquinone served as an efficient quencher for the pyridine-capped CdSe/CdS core/shell QDs, and the PL intensity was significantly decreased when the concentration of the quencher was increased. On the other hand, when the CdSe/CdS QD@ZIF-8 composites were used instead, PL quenching was hardly observed even in the presence of *1,4*-benzoquinone over the same concentration range (Fig. 1-14b). MOFs are well known for absorbing organic molecules into their cavities, but the pore diameter of the ZIF-8 is limited to ca. 0.3 nm. The size of the *1,4*-bonzoquinone molecule is large enough so that it cannot go through the cavities of ZIF-8; thus, the embedded QDs became unaffected to the added quenchers.

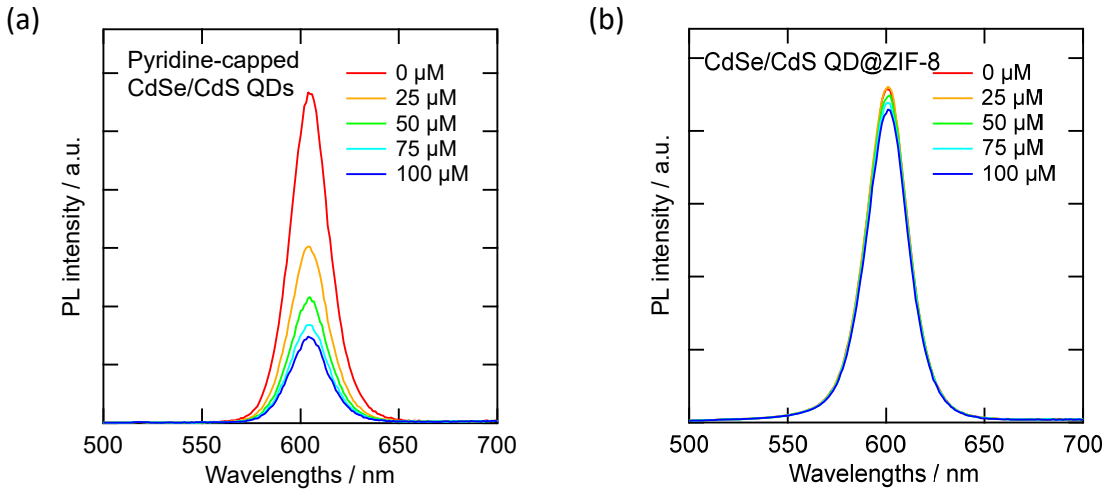

Figure 1-14. Changes in PL spectra for pyridine-capped CdSe/CdS QDs solution (a) and CdSe/CdS QD@ZIF-8 composite suspension (b) in the presence of 1,4-benzoquinone with different concentrations (450 nm excitation).

1-4. Summary

Quantum dots were successfully incorporated into ZIF-8 without using any bonding materials, such as polymers. By slowly increasing the amount of ZIF-8 precursors added to the reaction media, nearly monodispersed ZIF-8 crystals were grown directly on the surface of CdSe/CdS core/shell QDs. We visually observed the structure of ZIF-8 crystals gradually transform from a roughly spherical shape to rhombic dodecahedrons. Narrow band-edge emission unique to the QDs was maintained during and after the modification with ZIF-8. The PL QY of CdSe/CdS QD@ZIF-8 composite exceeded 40% even in the solid state. In addition, the incorporation of a single QD into a ZIF-8 crystal was successfully accomplished by changing the ligands on the QDs from pyridine to 4-*tert*-butylpyridine. Complete incorporation of the QDs into ZIF-8 crystals was demonstrated by both TEM images and PL quenching tests, where the addition of *1,4*-benzoquinone hardly affected the PL from the CdSe/CdS QD@ZIF-8 composite.

Chapter 2

Photoluminescence Enhancement of Quantum Dots through Energy Transfer from Light Harvesting Metal–Organic Frameworks

2-1. Introduction

The photochemical aspects of MOFs have been the topic of interest, aiming to use them as photocatalysts and chemical sensors.[31, 67, 68] However, for greater scientific meanings, MOFs should possess more controllable photochemical properties than amorphous materials (e.g., chromophores) because the distances and angles between the chromophores are determined by the crystal forms of MOFs.[31] Sometimes, MOFs are regarded as analogues of chlorophyll in leaves that collect light energy for subsequent photosynthetic reactions. As a method to utilize the energy collection properties, recent studies have demonstrated an efficient energy transfer system from photoluminescent MOFs to organic dyes included as guest molecules[69-71] or to coexisting dyes embedded in polymer matrix.[72] More recently, Y. Yang *et al.* reported the fabrication of the core/shell-like hierarchical structure of hybrid MOFs with different PL energies and successful observation of energy transfer between core and shell moieties.[73] Of course, the transferred energy can be used to drive chemical reactions with the assistance of photocatalysts.[74] Many previous studies have employed the Förster resonance energy transfer (FRET), which is one type of energy transfer induced by dipole–dipole coupling, in which the energy excited in a donor molecule is non-radiatively transferred to an acceptor molecule in the ground state.[75, 76] Together with the spectral overlap that is essential for FRET, the efficiency of FRET is strongly affected by the donor–acceptor distance, and the distance transferring 1/2 of the excitation energy (R_0) typically ranges from 20 to 90 Å depending on the strength of dipole coupling.[77] Therefore, when nanomaterials as large as the critical distance of FRET are utilized as donors and/or acceptors, the three-dimensional

configuration between the donor and acceptor (core/shell architecture) should considerably affect the efficient energy transfer.[76]

Owing to the precise controllability of luminescent color by changing the size and composition of QDs is attractive and useful,[3, 5, 78] which allows them to be built into upcoming optoelectronic devices as promising components.[13, 79, 80] A key technology for the fabrication of such QD-based solid devices is matrices between particles, which need to maintain the electronic independence of each QD (not to lose the quantum size effect) while satisfying the optical characteristics and/or electronic conductivity required for each device. Even for a very primitive application (e.g., wavelength conversion films), a certain distance between QDs is required to prevent self-quenching caused by energy collection to non-luminescent QDs via dipole coupling between the particles (homo-FRET).[62, 81] Technologies for embedding QDs (including conventional semiconductor QDs and lead halide perovskites) into solid materials (either inorganic crystalline materials[82-84] or polymer materials[85, 86]) have been developed to protect QDs from the possible damage (e.g., surface defects) generated by oxygen species, and these attempts have been very successful. In 2019, I demonstrated a new approach to ensure the long-term stability of QDs by utilizing a zeolite-based MOF (ZIF-8) as a surface modifier.[87] The robust matrices were also useful to suppress the aforementioned self-quenching. Plus, the proposed strategy for the fabrication of the QD/ZIF-8 core/shell structure without any intermediate layer (e.g., polymers) must be ideal for further applications that exploit the synergistic effects of both materials via energy transfer.

Previous studies on the energy transfer between QDs and MOFs reported by S. Jin *et al.* have been conducted using CdSe/ZnS core/shell QDs and porphyrin-containing MOFs. QDs were linked to the surface of MOF crystals by short organic molecules containing $–NH_2$ terminals that bind to Zn elements that exist on the surfaces of both QDs and MOFs. The energy transfer from QDs to MOFs was validated by steady-state and time-dependent PL data.[88] More recently, S. Bhattacharyya *et al.* synthesized perovskite QDs that were incorporated in the frame of luminescent MOFs (the MOF-related technique

is categorized as a ship-in-the-bottle approach), and efficient FRET from the host framework to QDs was achieved with an increase in the stability of perovskite QDs.[39] Thus, embedding nanometer-size QDs in MOF matrices is beneficial to both materials, providing synergetic effects to enhance the functions that these materials originally have, not only increasing chemical stability of QD materials. Of course, the energy transfer between MOFs and QDs by itself is of interest because both materials have unique electronic structures that are different from any molecular fluorophores. Whether the energy transfer between them almost follow the conventional Förster-type theory based on point charge or I need to develop a totally new theory is not even clear.

In this study, I performed the facile synthesis and characterization of a new QD–MOF composite whose surface of QD is directly modified by a light-harvesting MOF. This core/shell-like structure can be regarded as the configuration where an acceptor material is surrounded by a donor material without any specific linkers between them. This should provide an ideal situation to achieve a highly efficient energy transfer. To optically observe energy transfer, I focused on IRMOF-3 that has high absorbance in the UV-A region and emission in the blue region. Then, attempts were made to observe energy transfer from IRMOF-3 to CdSe/CdS/ZnS core/multishell QDs. The direct growth of IRMOF-3 on QDs was developed on the basis of my previous study, where the precursors of MOFs were added dropwise to the solution of QDs whose ligands were changed to weakly adsorbing pyridine.[87] As shown in Figure 2-1, I tested two types of QD–IRMOF-3 composites to compare their energy transfer efficiencies. The PL intensity from QDs was almost doubled under optimal conditions, which indicated the advantage of the system for the development of QD devices.

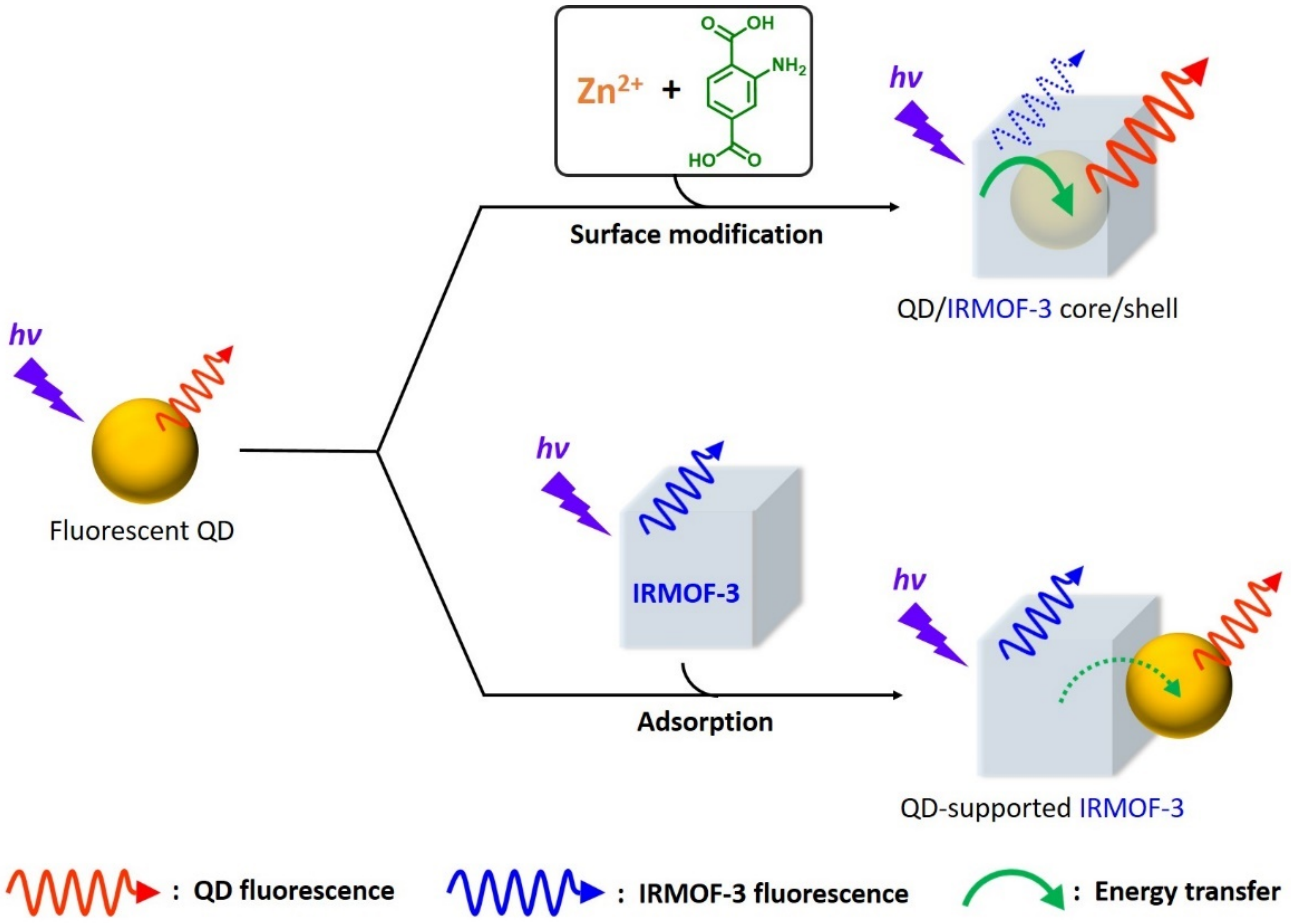

Figure 2-1. Schematic illustration of luminescent materials composed of semiconductor QD and light-harvesting MOF: a QD/IRMOF-3 core/shell composite (above) and QD-supported IRMOF-3 (below).

2-2. Experimental section

2-2-1. Chemicals

Cadmium oxide (CdO) was purchased from Sigma-Aldrich. Oleic acid (OA), 1-octadecene (ODE), sulfur powder (S), zinc acetate [$Zn(OAc)_2$], pyridine, triethylamine (TEA), and zinc acetate dihydrate [$Zn(OAc)_2 \cdot 2H_2O$] were purchased from FUJIFILM Wako Pure Chemical Corporation. Trioctylphosphine (TOP), 1-dodecanethiol, tributylphosphine (TBP), and 2-aminoterephthalic acid ($H_2BDC\text{-}NH_2$) were purchased from TCI. Selenium powder (Se) was purchased from Mitsuwa Chemicals Co., Ltd.

2-2-2. Synthesis of CdSe/CdS/ZnS QDs

Red fluorescent CdSe/CdS/ZnS core/multishell QDs were synthesized using the multiple injection method reported by J. Kwak *et al*.[89] Briefly, CdO (0.128 g, 1.0 mmol), OA (1.27 mL, 4 mmol), and ODE (20 mL) were mixed in a 100 mL two-necked flask and evacuated at 80°C for 30 min. Then, the temperature was increased to 300°C under Ar atmosphere and maintained for 10 min to generate a clear solution containing $Cd(OA)_2$. Se (19.74 mg, 0.25 mmol) dissolved in TOP (0.25 mL) was quickly injected into the flask, and the temperature was held at 300°C for 90 s to grow CdSe core QDs. Then, dodecanethiol (0.16 mL, 0.75 mmol) was added dropwise to the CdSe solution, and the reaction solution was held at 300°C for 30 min to form a CdS shell. Finally, $Zn(OAc)_2$ (0.734 g, 4.0 mmol) dissolved in OA (2.54 mL, 8.0 mmol) and S (0.128 g, 4.0 mmol) dissolved in TBP (0.2 mL) were sequentially injected into the reaction solution to form a ZnS shell. After 10 min of heating at 300°C, the flask was cooled to room temperature, and an excess amount of acetone was added to precipitate QDs. The suspension was centrifuged, and solid QDs were re-dispersed into hexane (100 mg/mL or 70 nmol/mL in terms of particles).

2-2-3. Ligand exchange of QDs

CdSe/CdS/ZnS core/multishell QDs (1 mL) were purified by precipitating with acetone and re-dispersed in hexane, and this procedure was repeated three times. Then, solid QDs were dispersed in pyridine (1 mL) and heated at 80°C for 24 h in a glass tube to complete ligand exchange to pyridine. After the suspension became clear, the solution was cooled to room temperature, and excess hexane was added to precipitate QDs. Completeness of the ligand exchange was confirmed by NMR. Powdery QDs obtained by centrifugation were re-dispersed in 1 mL of pyridine to a concentration of 100 mg/mL, which was used as a standard QD stock solution in subsequent experiments.

2-2-4. Synthesis of nanosized IRMOF-3

Blue fluorescent cubic IRMOF-3 with a 100–200 nm size was synthesized at room temperature using the method reported by A. Ranft *et al*.[90] $Zn(OAc)_2 \cdot 2H_2O$ (35.12 mg, 0.16 mmol) dissolved in DMF (2 mL) was quickly added to $H_2BDC\text{-}NH_2$ (10.86 mg, 0.059 mmol) dissolved in DMF (3 mL), and the mixture was stirred for 30 min at room temperature. The product was collected by centrifugation, washed with DMF/ethanol three times, and dried under reduced pressure to obtain a white powder.

2-2-5. Synthesis of the QDs/IRMOF-3 core/shell composite

$H_2BDC\text{-}NH_2$ (18.12 mg, 0.10 mmol) was deprotonated in advance by mixing with TEA (28 μL, 0.20 mmol) in DMF (10 mL), and the neutralized organic linker $[(NEt_3H)_2BDC\text{-}NH_2]$ was used as the precursor for IRMOF-3. The DMF solutions of $Zn(OAc)_2 \cdot 2H_2O$ (30 mM) and $(NEt_3H)_2BDC\text{-}NH_2$ (10 mM) were separately prepared as IRMOF-3 precursor solutions. In a typical synthesis, a pyridine-capped CdSe/CdS/ZnS core/multishell QD stock solution (10 μL, 0.7 nmol) was diluted with DMF (9 mL), and DMF solutions of $Zn(OAc)_2 \cdot 2H_2O$ (0.5 mL) and $(NEt_3H)_2BDC\text{-}NH_2$ (0.5 mL) were injected into the QD solution at a rate of 1.0 mL/h using two syringes attached to a syringe pump. Portions of the

suspension were taken after 1 h of stirring, and optical measurements and TEM observations were performed. The suspension was stirred for another 24 h at room temperature, and then, the obtained QDs/IRMOF-3 core/shell composites were collected by centrifugation. The precipitate was washed with DMF/ethanol three times and dried under reduced pressure. The QDs/IRMOF-3 core/shell composites with different IRMOF-3 volumes were synthesized by changing the amount of IRMOF-3 precursor solutions (i.e., 0.02, 0.05, 0.10, 0.25, and 0.50 mL) injected into the QD solution while keeping the total volume of the solutions at 5 mL, while the amount of the QDs in the system was kept at 0.7 nmol for each sample. After injection, the solutions were stirred for another 1 h at room temperature. During the reaction, aliquots (0.2 mL) were taken for optical measurements.

2-2-6. Synthesis of QD-supported IRMOF-3

Powdery nanosized IRMOF-3 was dispersed in DMF (5 mL) using an ultrasonic treatment. Then, pyridine-capped CdSe/CdS/ZnS core/multishell QDs (100 μL, 7 nmol) were quickly injected into the abovementioned solvent under stirring. The suspension was stirred for another 5 min at room temperature, and QD-supported IRMOF-3 was separated by centrifugation, washed with DMF/ethanol three times, and re-dispersed in DMF (5 mL) for TEM observation and optical measurements.

2-2-7. Characterization

UV–vis absorption spectra were recorded in the same manner described in Chapter 1. Photoluminescence (PL) and photoluminescence excitation (PLE) spectra were recorded using a fluorospectrometer (JASCO, FP-8600). Photoluminescence quantum yield (PL QY) was measured in the same manner described in Chapter 1. PL lifetimes were recorded using a time-correlated single-photon counting instrument (Hamamatsu, Quantaurus-Tau). TEM images were acquired in the same

manner described in Chapter 1. Powder X-ray diffraction (PXRD) patterns were collected using a powder X-ray diffractometer (Rigaku, SmartLab) equipped with a parallel beam/parallel slit analyzer.

2-3. Results and discussion

2-3-1. Characterization of the QDs/IRMOF-3 core/shell composite and QD-supported IRMOF-3

Figure 2-2a shows the TEM image of pyridine-capped CdSe/CdS/ZnS core/multishell QDs used as starting QDs to fabricate subsequent QD–IRMOF-3 composites. After the ligand exchange, the gap between particles became smaller than that of the original particles while maintaining the shape of individual particles. Figure 2-2b shows the UV–vis and PL spectra of pyridine-capped QDs dispersed in DMF. The UV–vis absorption profile and narrow-band emission were mostly preserved, but PL QY was slightly decreased from 87.5% to 60.9%. A decrease in PL may be caused by the partial aggregation of QDs in solution phase[81] and/or hole-leaking from the CdSe core to pyridine over the shell.[63] Nevertheless, pyridine-capping is essential for the growth of IRMOF-3 because pyridine is an easily removable weak base ligand and pyridine-capped QDs are highly soluble in DMF. Because IRMOF-3 (which is used in this study and has organic linkers of *p*-benzoic acid derivatives) can be synthesized in DMF, we have a limited choice of solvent to dissolve both species.

Nanosized IRMOF-3 without QDs was successfully prepared by mixing $Zn(OAc)_2 \cdot 2H_2O$ and $H_2BDC\text{-}NH_2$ in DMF at room temperature, and the formation of cubic IRMOF-3 crystal (100–200 nm) was confirmed by TEM observation (Figure 2-2c). Figure 2-2d shows the UV–vis and PL spectra of the IRMOF-3 crystal suspended in DMF. The suspension had high absorbance in the UV-A region and emission in the blue region, which indicated that IRMOF-3 could work as a light-harvesting material for QDs.

Figures 2-2e and 2f show the TEM image and optical spectra of the QDs/IRMOF-3 core/shell composite. By comparing three TEM images (Figures 2-2a, 2c, and 2e), it is clear that the small dark spots representing QDs are mostly surrounded by the rounded cubic crystals of IRMOF-3. The fact that

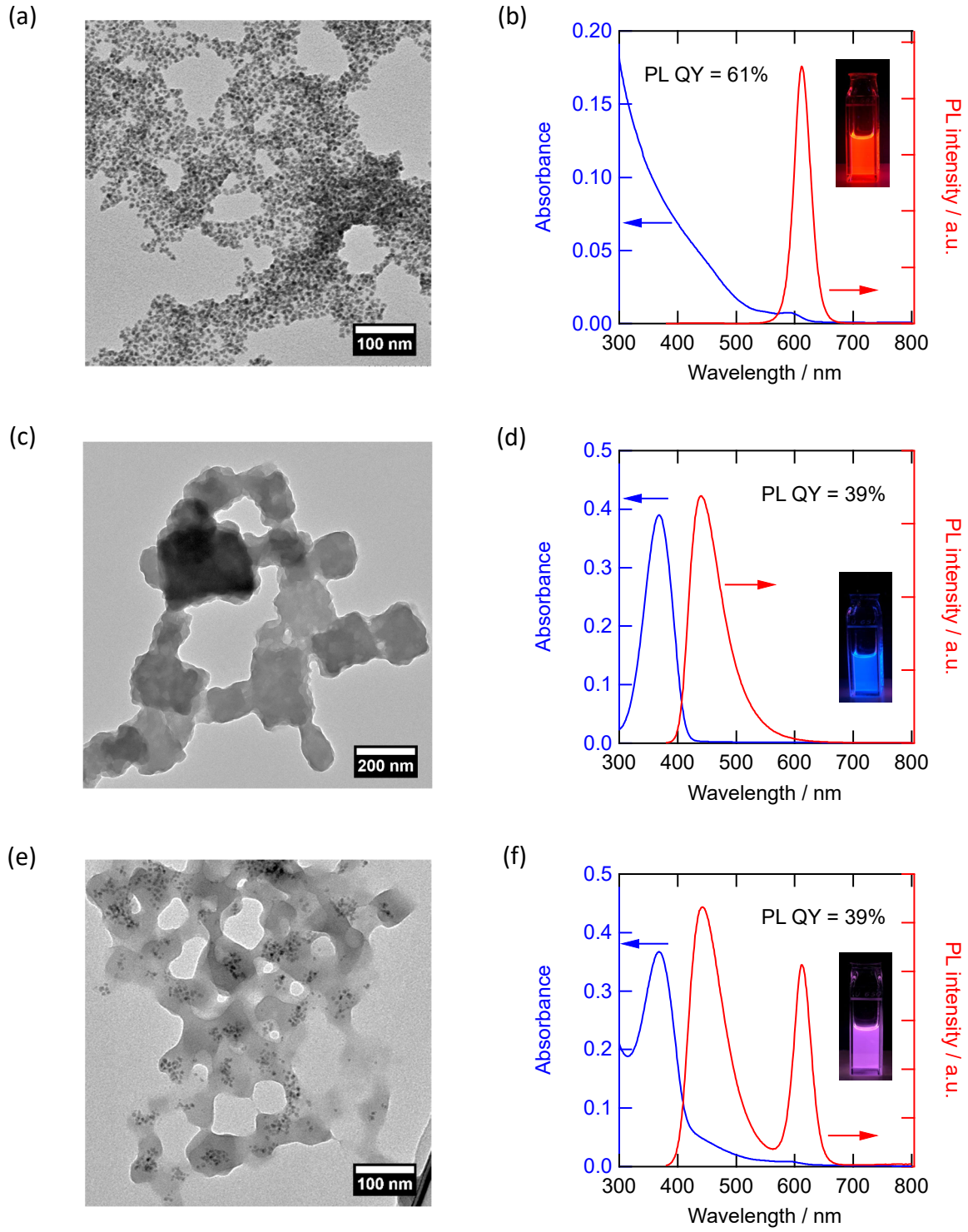

Figure 2-2. TEM images (a, c, e) and UV−vis and PL spectra (b, d, f) of pyridine-capped CdSe/CdS/ZnS core/multishell QDs (a, b), nanosized IRMOF-3 (c, d), and QDs/IRMOF-3 core/shell composite prepared by the addition of 0.5 mL of precursor solutions (e, f). For optical measurements, samples were dispersed in DMF. The excitation wavelength was 370 nm for all PL spectra, and the inset photographs of each sample were obtained under UV irradiation.

each crystal contains plural QD particles confirms the growth of IRMOF-3, which is initiated on the surface of QDs in a similar manner to the case of ZIF-8 on QDs that I have previously reported.[87] The

possible mechanism for the formation of the QDs/IRMOF-3 core/shell composite was illustrated in Figure 2-3. The pyridine-capped QDs firstly underwent a ligand exchange in situ to 2-aminoterephthalic acid, one of the components of IRMOF-3, upon initiation of injection. Then, IRMOF-3 crystals were preferentially grown from the surface of the QDs rather than causing self-nucleation in the bulk solution. Figure 2-2f shows the UV–vis and PL spectra of the QDs/IRMOF-3 core/shell composite suspended in DMF. As can be predicted from the TEM image, the UV-vis spectrum involves features of both QDs and IRMOF-3, in which a single absorption band deriving from IRMOF-3 overlapped the absorption of QDs. The PL spectrum showed two peaks (Figure 2-2f, red): the longer wavelength peak (612 nm) corresponds to QDs, and the shorter wavelength peak (443 nm) corresponds to IRMOF-3.

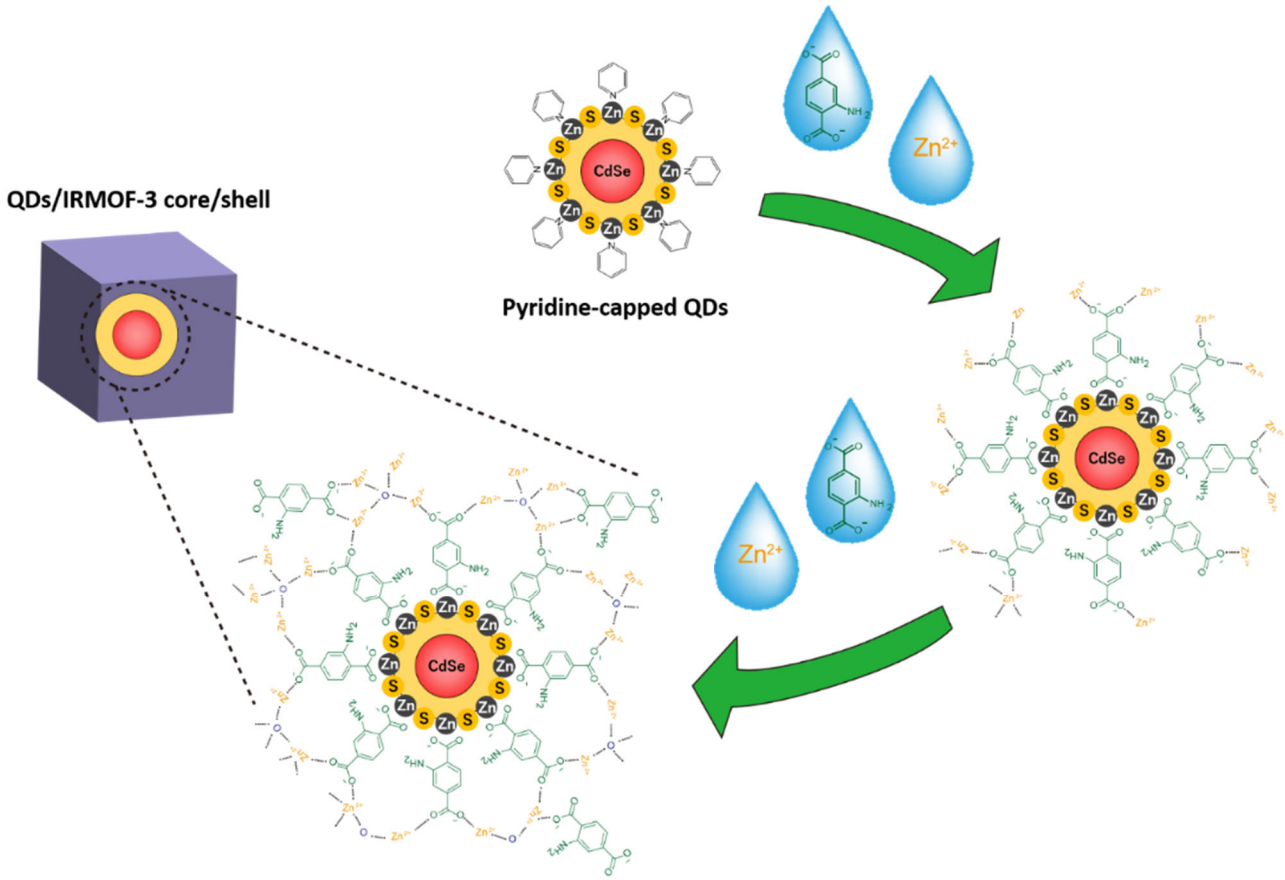

Figure 2-3. Schematic illustration for the growth process of QD/IRMOF-3 core/shell composite. IRMOF-3 crystal is grown directly on the metal site of QDs.

As shown in Figure 2-4, both nanosized IRMOF-3 and QDs/IRMOF-3 core/shell composite showed an identical PXRD pattern. Plus, they were in good agreement with the simulated pattern of the IRMOF-3 single crystal (CCDC no. 175574).[21] This result implies that the dropwise addition of precursors into the QD solution successfully grew crystalline IRMOF-3 around QDs. However, signals from QDs were completely hidden because the volumetric ratio of QDs is considerably smaller than that of IRMOF-3, as observed in the TEM image (Figure 2-2e), and the PXRD peaks of QDs must be broad owing to the limited crystal length.[42]

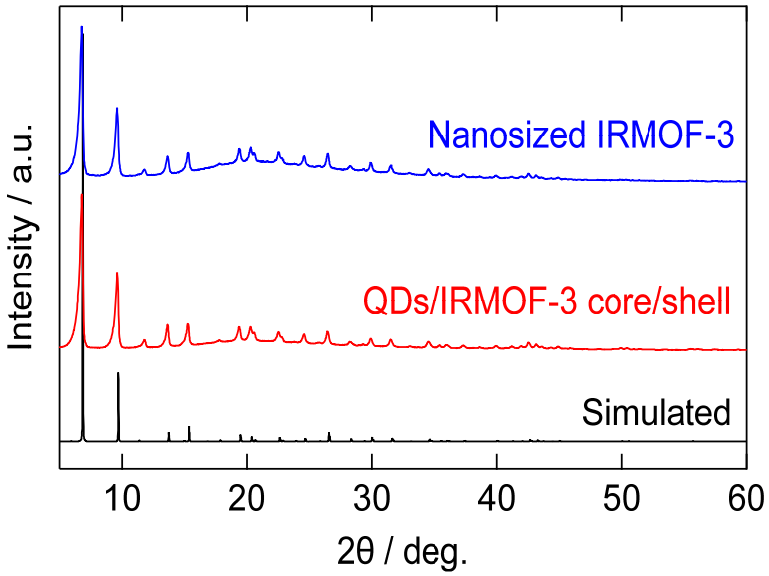

Figure 2-4. PXRD patterns of nanosized IRMOF-3 without including QDs (blue) and QDs/IRMOF-3 core/shell composites prepared by the addition of 0.5 mL of precursor solutions (red) compared to the simulated pattern of IRMOF-3 (black)

Figure 2-5 shows the TEM image of the sample prepared by the swift addition of IRMOF-3 precursors into the QD solution, which was performed as a control experiment. Compared to the samples obtained by dropwise addition, it is clear that QDs and IRMOF-3 are located separately, which indicates that IRMOF-3 grew independently of QDs. This fact confirms the effectiveness of dropwise addition for the epitaxial growth of IRMOF-3 on the surface of QDs. Thus, QD served as a seed crystal for the IRMOF-3 shell to grow on when IRMOF-3 precursors were added dropwise.

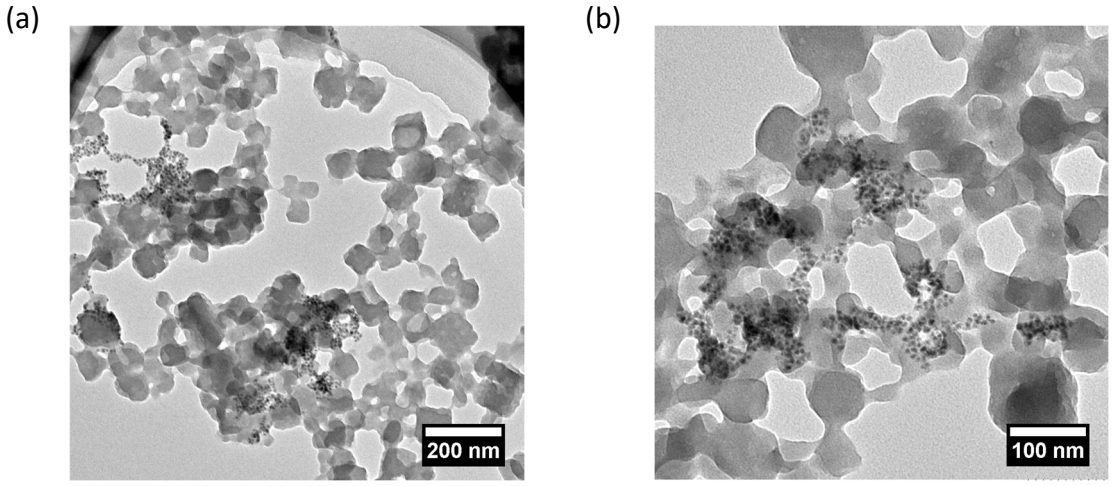

Figure 2-5. TEM images of nanosized IRMOF-3 existing separately from CdSe/CdS/ZnS core/multishell QDs: overall (a) and magnified (b) images. The samples were synthesized by quickly adding IRMOF-3 precursors into the QD solution.

Another type of QD–IRMOF-3 composite was prepared by attaching pyridine-capped CdSe/CdS/ZnS core/multishell QDs (Figure 2-2a) onto the surfaces of nanosized IRMOF-3. When the nanosized IRMOF-3 suspension was mixed with the QD solution, it was observed that all QDs were spontaneously adsorbed on cubic IRMOF-3 surfaces. Figure 2-6a shows the TEM image of the resulting QD-supported IRMOF-3, which clearly indicates the existence of many QDs on the surface of cubic IRMOF-3 crystals. The QD-supported IRMOF-3 sample showed an absorption feature that was the sum of the respective spectrum of QDs and IRMOF-3, as shown by the blue line in Figure 2-6b, which was similar to the

absorption spectrum of the QDs/IRMOF-3 core/shell composite. The PL spectrum, as shown by the red line in Figure 2-6b that includes both PL peaks owing to IRMOF-3 and QDs, also resembles the PL spectrum obtained for the QDs/IRMOF-3 core/shell composite.

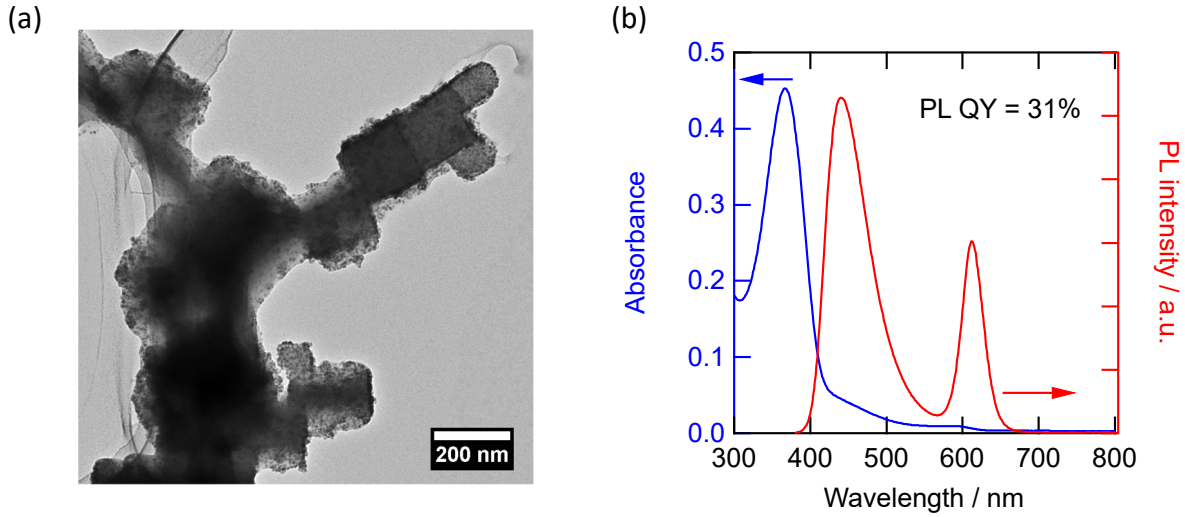

Figure 2-6. TEM image (a) and UV−vis and PL spectra (b) of CdSe/CdS/ZnS core/multishell QD-supported IRMOF-3. The sample was dispersed in DMF for optical measurements, and the excitation wavelength was 370 nm for the PL spectrum measurement.

2-3-2. PL enhancement of QDs by the IRMOF-3 shell

QDs/IRMOF-3 core/shell composites with different shell volumes were prepared by changing the amount of IRMOF-3 precursors added dropwise to the QD solution while keeping the QD concentration constant. Figures 2-7a and 7b show the UV–vis and PL spectra of CdSe/CdS/ZnS core/multi-shell QDs and QDs/IRMOF-3 core/shell composites with a different amount of the IRMOF-3 shell dispersed in

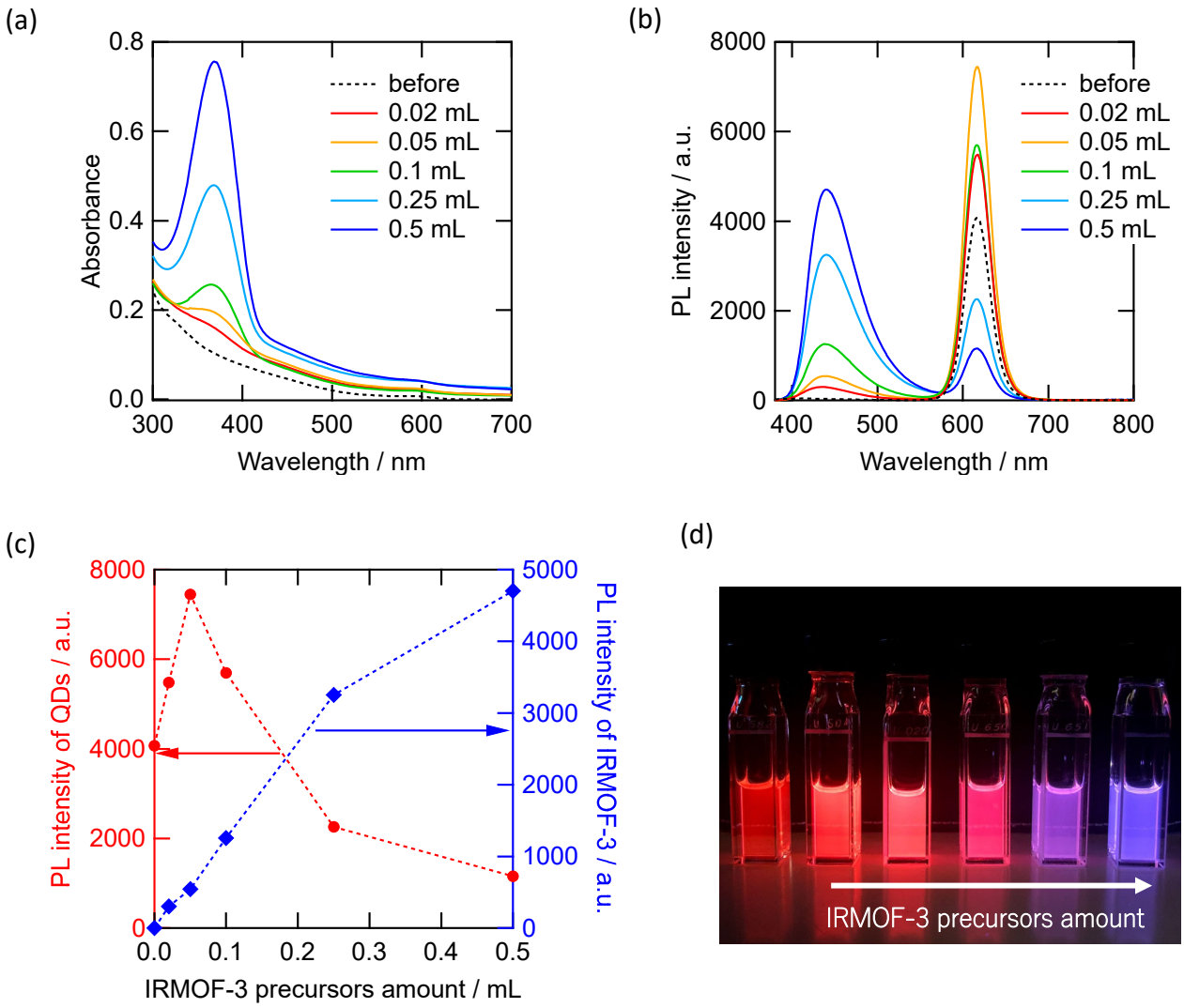

Figure 2-7. UV−vis spectra (a) and PL spectra (b) of pyridine-capped CdSe/CdS/ZnS core/multishell QDs (black dotted line) and QDs/IRMOF-3 core/shell composites prepared using different amounts of precursor solutions (colored solid line). The samples were diluted with DMF to 20 μg/mL in terms of QDs upon measurements. The excitation wavelength was 370 nm for PL spectra measurements. The plots of PL intensity derived from QDs (left axis) and that from the IRMOF-3 shell (right axis) of pyridine-capped QDs and QDs/IRMOF-3 core/shell composites, respectively, as a function of the amount of precursor solutions for the preparation of composites (c). The corresponding photograph of QDs and QDs/IRMOF-3 core/shell composites under UV irradiation (d)

DMF. Because it was difficult to accurately express the amount of IRMOF-3 shell on QDs, the volumes of each precursor solution added to the QD solution during their syntheses are specified here. With an increase in the amount of added precursor solutions, a new absorption peak derived from IRMOF-3 emerged and increased at 368 nm. The PL spectrum also showed an increase in blue fluorescence (440 nm), and its intensity increased with an increase in the amount of precursor solutions. Of note, the intensity of the PL peak at 612 nm originating from CdSe/CdS/ZnS core/multishell QDs was enhanced for the QDs/IRMOF-3 composites prepared by the addition of 0.02 and 0.05 mL of precursor solutions, although the concentration of QDs was the same for all cases, as mentioned above. In the latter case, the peak intensity was almost doubled compared to that of CdSe/CdS/ZnS core/multishell QDs. The TEM images of the composites which exhibited enhancement of PL from the QDs were shown in Figure 2-8. Although multiple QDs were included in a unit of IRMOF-3 shells, these particles kept a certain distance with each other. This was coincided with the absence of self-quenching when these composites were excited at the wavelength irrelevant to the absorption of IRMOF-3, as discussed later. The tendency of QD's PL enhancement by IRMOF-3 ceased when the amount of precursor solutions was increased to 0.1 mL (3 μmol of the zinc node and 1 μmol of the organic linker), above which the PL intensity gradually decreased without any change in the spectral shape (Figures 2-7b and 7c). The TEM image of the quenched core/shell composite (the amount of IRMOF-3 precursor solutions was 0.25 mL) showed 100-nm-sized cubic IRMOF-3 crystals over the entire observation field (Figure 2-9). These large crystals could be observed when the precursor concentration was higher than a certain level. The observed dramatic shape change is known to occur to minimize the Gibbs free energy of a particle.[91] Figure 2-7d shows the photograph of pyridine-capped QDs and QDs/IRMOF-3 core/shell composites obtained under UV irradiation. The changes in color and PL brightness are well reflected by their optical characteristics shown in Figures 2-7b and 7c.

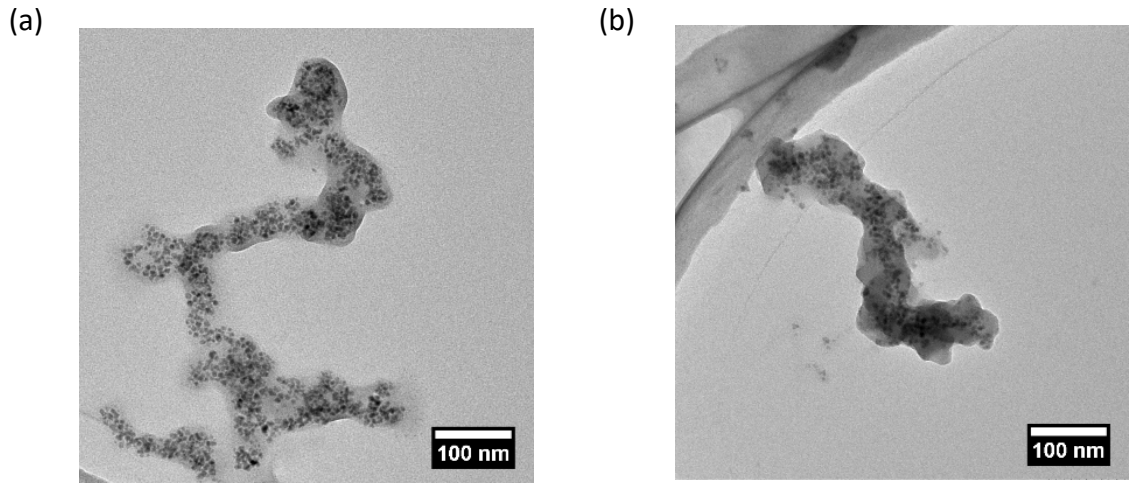

Figure 2-8. TEM images of the QDs/IRMOF-3 core/shell composite prepared by adding 0.05 mL (a) and 0.1 mL (b) of IRMOF-3 precursors to pyridine-capped CdSe/CdS/ZnS core/multishell QDs in DMF.

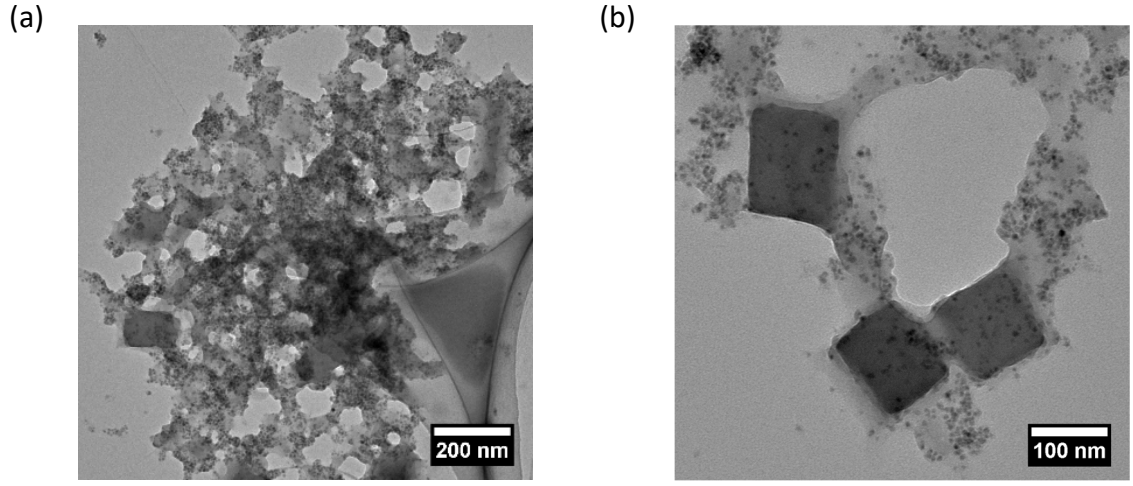

Figure 2-9. TEM images of the QDs/IRMOF-3 composite prepared by adding 0.25 mL of IRMOF-3 precursors: overall (a) and magnified (b) images

These results invoke the idea that IRMOF-3 has two crucial roles. The first role is an antenna, which receives light energy and sends the excitation energy to neighboring QDs. The second role is the shield against the photoexcitation of QDs. When the thickness of the IRMOF-3 modifier is relatively thin, the energy absorbed by IRMOF-3 can be effectively transferred to the QD acceptor, which results in the considerable enhancement in the PL intensity from QDs. However, when the IRMOF-3 unit becomes considerably larger, in which many parts of IRMOF-3 cannot provide excitation energy to QDs owing to the energy transfer limit determined by Förster distance, PL intensity began to decrease with an increase in the volume of IRMOF-3. Of note, PL quenching originating from the changes in the QD/IRMOF-3 interface was not observed at all. This was demonstrated by the PL decay curves of QDs that became longer rather than shorter after being incorporated in IRMOF-3 (Figure 2-10). The elongation of PL decay indicates the presence of exciton that was fed from IRMOF-3 (donor) to QDs (acceptor).[92]

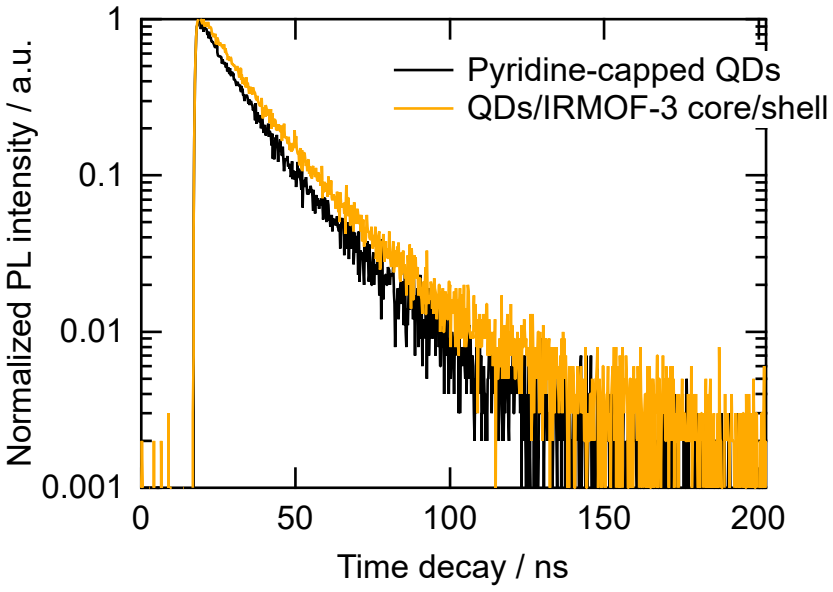

Figure 2-10. PL decay curves for pyridine-capped CdSe/CdS/ZnS core/multishell QDs (black line) and the QDs/IRMOF-3 core/shell composite (orange line) dispersed in DMF. The curves were recorded at an excitation wavelength of 365 nm, and an emission wavelength of 612 nm was derived from QDs

2-3-3. Energy transfer from IRMOF-3 to QDs

To verify whether the enhancement of PL from QDs in the QDs/IRMOF-3 core/shell composite was resulted from the energy transfer from IRMOF-3 to CdSe/CdS/ZnS core/multishell QDs, the PL properties of the QDs/IRMOF-3 core/shell composite and QD-supported IRMOF-3 were investigated in detail. Figure 2-11a shows the PLE spectrum recorded with an excitation light at 612 nm. The intensity was normalized at 450 nm, where IRMOF-3 did not have an absorbance. The comparison

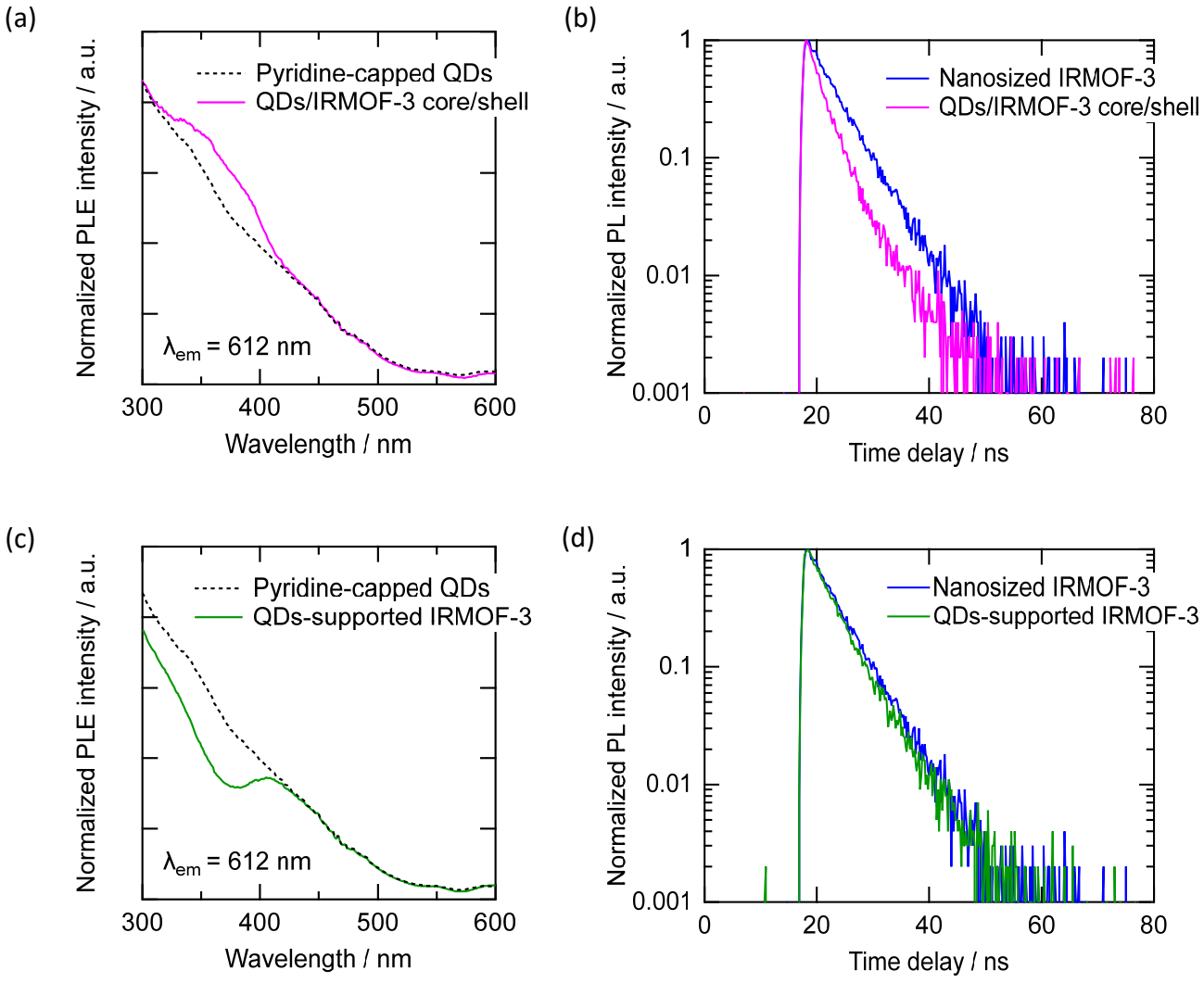

Figure 2-11. Normalized PLE spectra of the QDs/IRMOF-3 core/shell composite (amount of IRMOF-3 precursors = 0.1 mL) (a) and QD-supported IRMOF-3 (c) detected at 612 nm. Black dotted line represents the normalized PLE spectrum of pyridine-capped CdSe/CdS/ZnS QDs. Donor PL decay curves for the QDs/IRMOF-3 core/shell composite (b) and QD-supported IRMOF-3 (d) recorded at an excitation wavelength of 365 nm and emission wavelength of 440 nm derived from IRMOF-3. The blue solid line represents the PL decay curve of nanosized IRMOF-3 in the absence of the QD acceptor.

between two spectra revealed a considerable PL enhancement in the wavelength region where IRMOF-3 has an absorption. Figure 2-12 showed the differential PLE spectrum (QDs/IRMOF-3 core/shell composite – pyridine-capped QDs) together with the corresponding differential absorption spectrum. The shapes of the two spectra were very similar to each other, which indicated that the photons absorbed excessively by IRMOF-3 were eventually transferred to QDs. The occurrence of the energy transfer was also proven by time-dependent measurements of PL from IRMOF-3 at 440 nm. The PL decay rate obtained for the core/shell composite was clearly faster than that for nanosized IRMOF-3 with a similar size and shape (Figure 2-11b). Then, the decay curves were fitted with the following equation:

$$I(t) = \sum_i A_i \exp\left(-\frac{t}{\tau_i}\right), \quad (1)$$

where $I(t), A_i$, and τ_i are the PL intensity at time t, amplitude, and lifetime, respectively. i is the least number of terms needed to obtain sufficient fitting. The fitting parameters for the two curves are summarized in Table 1. Nanosized IRMOF-3 had a single decay component ($\tau = 4.77$ ns), whereas

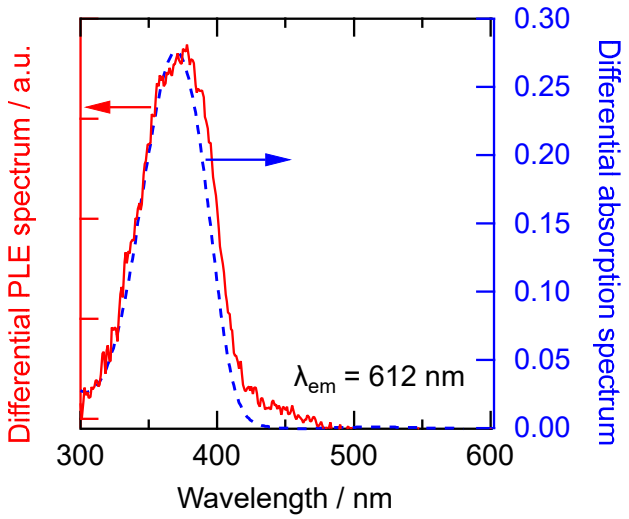

Figure 2-12. Differential PLE spectrum (QDs/IRMOF-3 core/shell composite – pyridine-capped QDs) detected at 612 nm originating from QDs (left axis) and the corresponding differential absorption spectrum (right axis)

Table 1. Fitting parameters for the PL decay curves of nanosized IRMOF-3, QDs/IRMOF-3 core/shell composite, and QD-supported IRMOF-3 shown in Figures 2-11b and 11d (λ_{ex} = 365 nm and λ_{em} = 440 nm)

Sample	A_1	τ_1 (ns)	A_2	τ_2 (ns)	A_1/A_2
Nanosized IRMOF-3	1.00	4.77	—	—	—
QDs/IRMOF-3 core/shell composite	0.69	1.86	0.31	4.41	2.23
QDs-supported IRMOF-3	0.17	1.72	0.83	4.59	0.20

the core/shell composite showed two components ($\tau_1 = 1.86$ ns and $\tau_2 = 4.41$ ns) with an intensity ratio of 0.69:0.31. These results clearly indicated that the energy transfer to QDs occurred from the portion of IRMOF-3,[76] which shortened the lifetime compared to the original one, while the other moiety remained almost unchanged. HOMO and LUMO are basically localized in IRMOF-3, and there is a significant spectral overlap between the PL spectrum of IRMOF-3 and the absorbance spectrum of QDs. Therefore, energy transfer was mainly caused by the Förster mechanism rather than by the electron/hole transfer,[93, 94] which means that the energy excited at the moiety of IRMOF-3, which is located in a few nanometer distance from the QD surface, can be transferred to QD, which enhances the PL intensity. However, an IRMOF-3 moiety located farther than a certain distance from QDs emits by itself. Of course, the scattering of the excitation light is one of the factors causing a change in PL intensity from QDs, and the excitation efficiency is expected to increase when QDs are surrounded by a material with a large refractive index. However, considering the refractive index of IRMOF-3 ($n_{\mathrm{IRMOF-3}} = 1.21$) and DMF ($n_{\mathrm{DMF}} = 1.43$) used for the dispersion medium, this effect is either negligible or lowers the PL intensity by reducing the excitation light coming into QDs (Figure 2-13).[90]

Interestingly, the PLE spectrum of QD-supported IRMOF-3 was completely different from that of the core/shell composite, as shown in Figure 2-11c. The PLE intensity was clearly reduced at the wavelength range where IRMOF-3 has an absorption. The PL intensity for the QD-supported IRMOF-3 normalized by the QDs' absorption was 33% lower than that expected for the pristine QDs, when they

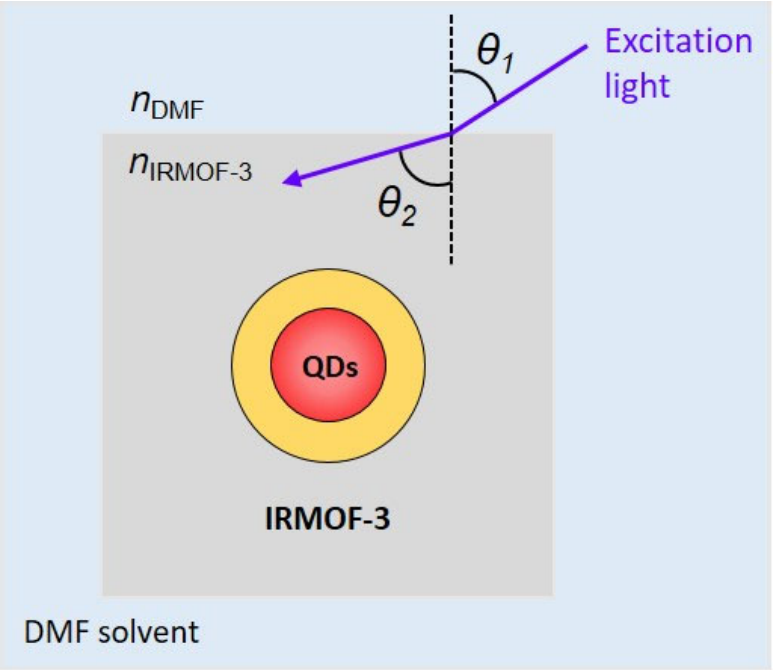

Figure 2-13. Schematic illustration of light reflection at the liquid–solid interface between DMF and IRMOF-3. The refractive index of DMF ($n_{\mathrm{DMF}} = 1.43$) is larger than that of IRMOF-3 ($n_{\mathrm{IRMOF-3}} = 1.21$). Thus, refraction angle (θ_2) is larger than incident angle (θ_1).

were excited at 370 nm, which is the absorption maximum of IRMOF-3. The IRMOF-3 crystals in both QD-supported IRMOF-3 and QDs/IRMOF-3 core/shell composite are very similar to each other (similar shape and size, and same crystal structure), whereas the positional relationship between the two materials is different. Therefore, the decrease in the PLE intensity observed in Figure 2-11c is considered to be caused by the shielding effect of IRMOF-3 against QD photoexcitation. In fact, when the absorption-normalized PL intensities (when excited at 500 nm) were compared between the three samples, PL intensity of both core/shell composite and QD-supported IRMOF-3 was definitely 2–17% higher than that of the pristine pyridine-capped QD solution. Although these data include some degree of uncertainty due to light scattering by the surrounding IRMOF-3, I cannot find any traces of PL quenching originating from the conditions of the QDs themselves. That is, the formation of nonradiative trap states by making contact with IRMOF-3 and/or self (concentration) quenching often observed for aggregated nanoparticles was negligible in the current experimental condition. Thus, the inconsistency

in PLE intensity at 300 nm (where IRMOF-3 barely absorbs) is attributed to Mie scattering originating from larger IRMOF-3 crystals. Figure 2-11d shows a PL decay curve of the emission from the IRMOF-3 moiety of QD-supported IRMOF-3 and that from pristine nanosized IRMOF-3. Although the two decay curves looked very similar to each other, the analysis of the PL decay obtained for the QD-supported IRMOF-3 sample produced two lifetimes ($\tau_1 = 1.72$ ns and $\tau_2 = 4.59$ ns). These values are similar to those obtained for the core/shell composite (Table 1), but the intensity ratio of 0.17:0.83 between shorter and longer lifetime components showed a diametrically opposite trend compared to that of the core/shell composite (0.69:0.31). Regarding the A_1/A_2 value, which represents the ratio of the excitation energy consumed by the energy transferred from IRMOF-3 to QDs to that consumed by PL generation from IRMOF-3, QD-supported IRMOF-3 showed a considerably smaller value (0.20) than that of the core/shell composite (2.23). The decrease in PLE intensity at the wavelength range where IRMOF-3 has an absorption was also observed when higher amounts of IRMOF-3 precursors were mixed with the QD solution (Figure 2-14). Since QDs were embedded deep in the IRMOF-3 shells, the shielding effect overwhelmed the emission enhancement brought by the energy transfer.

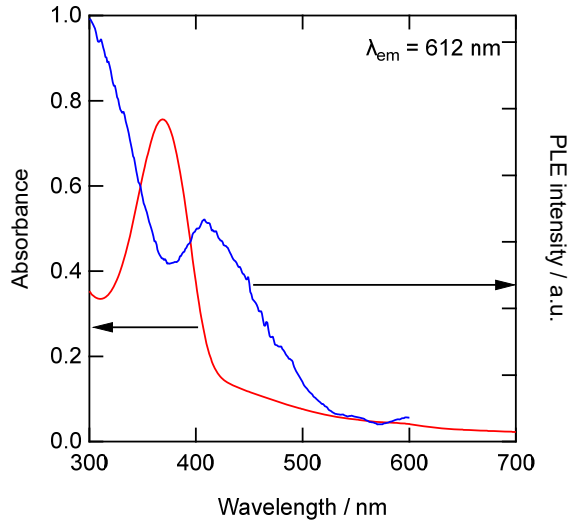

Figure 2-14. UV-vis absorption and PL excitation spectra for QDs/IRMOF-3 core/shell composite when 0.5 mL of IRMOF-3 precursors were introduced into DMF solution of pyridine-capped QDs.

2-3-4. Theoretical evaluation for energy transfer

The energy transfer efficiencies (η_{ET}) from IRMOF-3 to QDs in the two configurations (QDs/IRMOF-3 core/shell composite and QD-supported IRMOF-3) were estimated by

$$\eta_{ET} = (\tau_D - \tau_{DA})/\tau_D , \quad (2)$$

where τ_D and τ_{DA} are the PL lifetime of fluorophore itself and that of the donor–acceptor pair, respectively. If the shorter (τ_1) and longer (τ_2) lifetime components observed for the two samples were attributed to τ_{DA} and τ_D, respectively, the values of η_{ET} were calculated to be 0.58 and 0.62 for the QDs/IRMOF-3 core/shell composite and QD-supported IRMOF-3, respectively, which suggested that the distance and dipole coupling related to energy transfer were similar between two configurations. However, intensity factor (A_{DA}/A_D) corresponding to τ_{DA} and τ_D was 11 times higher for the core/shell composite than for the QD-supported IRMOF-3, as mentioned in the previous section. These results indicate that the ratio of the amount of IRMOF-3 from which excitation energy can transfer to the neighboring QDs was totally different between two configurations, while the efficiency of energy transfer was similar.

As mentioned above, Förster resonance energy transfer (FRET) is the main pathway of energy transfer between IRMOF-3 and QDs. In the theoretical description of FRET, the distance dependence of energy transfer rate (k_{RET}) is described by

$$k_{RET} = \frac{1}{\tau_D}\left(\frac{R_o}{R}\right)^6 , \quad (3)$$

where R is the distance (nm) between the donor and acceptor, and R_o is the Förster distance (nm), where k_{RET} becomes equal to $1/\tau_D$, i.e., the distance giving PL intensity half of the original. The value of Förster distance is described as

$$R_{\mathrm{o}} = \left(\frac{9(\ln 10)\kappa^2\eta_{\mathrm{D}}}{N_{\mathrm{A}}128\pi^5 n^4}J\right)^{1/6}, \quad (4)$$

where $\kappa, \eta_{\mathrm{D}}, N_{\mathrm{A}}, and\ n$ are the relative orientation of dipoles between the donor and acceptor, PL quantum yield of donor, Avogadro number (mol^{-1}), and refractive index of the medium (IRMOF-3 in this case), respectively. J is the factor representing the magnitude of the spectral overlap between the PL of IRMOF-3 (donor) and absorption of QDs (acceptor), which is usually described in the unit of $\mathrm{M}^{-1}\ \mathrm{cm}^{-1}\ \mathrm{nm}^4$.[94] When the Avogadro number and J ($\mathrm{M}^{-1}\ \mathrm{cm}^{-1}\ \mathrm{nm}^4$) = $10^{17} \times J$ ($\mathrm{mol}^{-1}\ \mathrm{nm}^6$) are applied, eq. 4 can be simplified as

$$R_0 \ = \ 0.0211(\kappa^2\eta_D n^{-4} J)^{1/6}[\mathrm{nm}]. \quad (5)$$

The essence of J is

$$J \ = \ \int_0^\infty f_{\mathrm{D}}(\lambda)\varepsilon_{\mathrm{A}}(\lambda)\lambda^4 d\lambda, \quad (6)$$

where $f_{\mathrm{D}}(\lambda)$ in $[\mathrm{nm}^{-1}]$ is the normalized emission spectrum of the donor as a function of λ, which is described as $f_{\mathrm{D}} = F_{\mathrm{D}}(\lambda)/\int F_{\mathrm{D}}(\lambda)\mathrm{d}\lambda$ using PL spectrum $F_{\mathrm{D}}(\lambda)$. $\varepsilon_{\mathrm{A}}(\lambda)$ $[\mathrm{M}^{-1}\ \mathrm{cm}^{-1}]$ is the molar extinction coefficient of the acceptor as a function of λ nm. Figure 2-15 shows the values of $f_{\mathrm{D}}(\lambda)$ of IRMOF-3 and $\varepsilon_{\mathrm{A}}(\lambda)$ of CdSe/CdS/ZnS core/multishell QDs. The latter was calculated by treating one core/shell QD as a large molecule. The integration of two spectra using eq. 6 gave a value of $J = 1.49 \times 10^{17}\ \mathrm{M}^{-1}\ \mathrm{cm}^{-1}\ \mathrm{nm}^4$ or $1.49 \times 10^{34}\ \mathrm{mol}^{-1}\ \mathrm{nm}^6$. After determining other parameters for the calculation of R_{o}, it became clear that we did not have enough evidence to expect the value of dipole orientation factor, κ. However, because acceptor QDs are spherical and while there is no evidence of anisotropy between the IRMOF-3 crystal and incorporated (or adsorbed) QDs, it is still reasonable to use the value of $\kappa^2 = 2/3$, which is commonly adopted when the positional (or orientational) relationship between a donor and an acceptor is random. The intrinsic quantum yield (η_{D}) of the

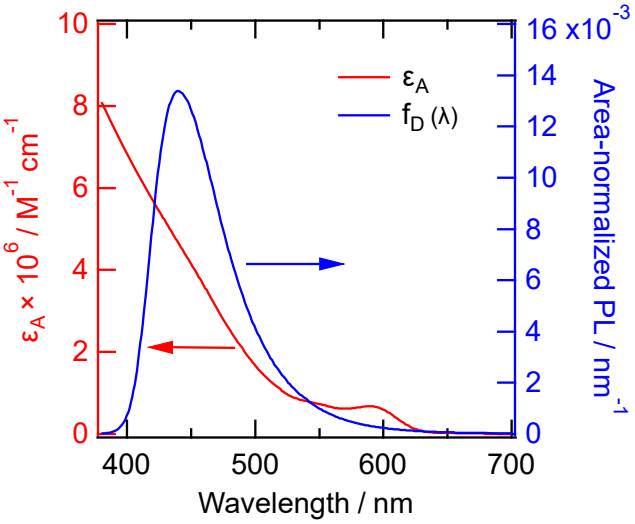

Figure 2-15. Molar extinction coefficient, $\varepsilon_A(\lambda)$, of pyridine-capped CdSe/CdS/ZnS core/multishell QDs acting as an acceptor (left axis) and the area-normalized emission spectrum (excited at 370 nm) of IRMOF-3 acting as a donor (right axis) used to calculate the overlap integral *J*.

IRMOF-3 donor in the absence of the QD acceptor was 39%. As the value of the refractive index n of the CdS/ZnS multishell, we used volume-weighted average refractive indices of CdS and ZnS that were calculated to be $n = 2.5$.[95, 96] The substitution of the abovementioned parameters into eq. 5 gave a Förster distance of $R_0 = 6.67$ nm.

On the basis of the values estimated above, I attempted to evaluate how much of the IRMOF-3 moiety in the sample acted as a light-harvesting antenna in the two different systems (QDs/IRMOF-3 core/shell composite and QD-supported IRMOF-3). However, the theory of FRET targets small molecules that can be regarded as points, C. Chen *et al.* proposed the use of an effective Förster distance by subtracting nanoparticle radius from the theoretical R_0 value when they investigate energy transfer in a nanoparticular system.[97] In my experiments, because CdSe/CdS/ZnS core/multishell QDs with a diameter (d_{QDs}) of 8 nm were used as an acceptor, the effective Förster distance of $R_0' = R_0 - d_{QDs}/2 = 2.67$ nm was used to estimate the volumetric parameters for IRMOF-3 that works as an antenna. When QD is completely embedded in IRMOF-3, the volume of IRMOF-3, which transfers its excitation energy to neighboring QDs and results in over 50% efficiency ($V_{RET,50}$), corresponds to the black-latticed area shown in Figure 2-16a. By subtracting the volume of QDs ($(4\pi/3){r_{QDs}}^3 =$

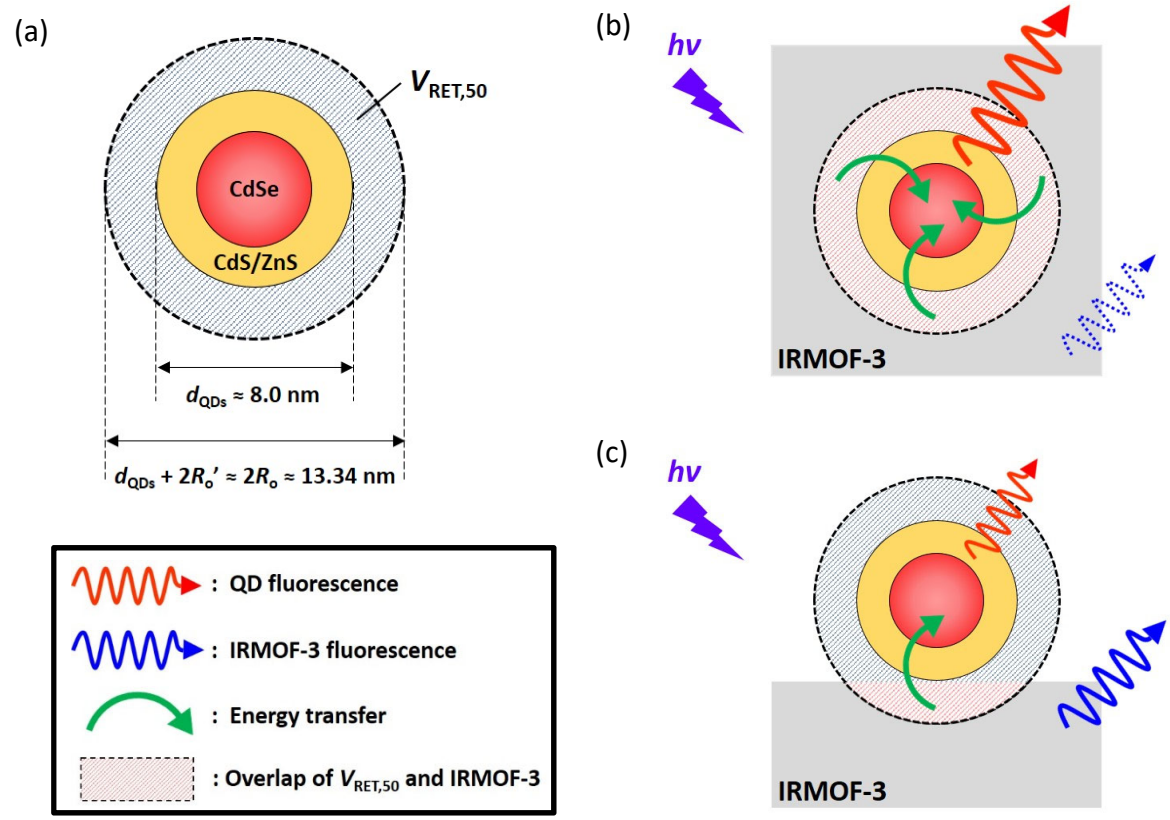

Figure 2-16. Sectional drawing of CdSe/CdS/ZnS core/multishell QD with a diameter of 8 nm used as an acceptor (a). The inorganic shell (CdS/ZnS) is approximately 2 nm. The black-latticed area represents the region where 50% of excitation energy of the IRMOF-3 donor is transferred to neighboring QDs ($V_{RET,50}$). This value was estimated by subtracting the radius of QDs from the Förster distance R_0 = 6.67 nm. Schematic diagrams of the QDs/IRMOF-3 core/shell composite (b) and QD-supported IRMOF-3 (c). The red area represents the overlap of $V_{RET,50}$ and IRMOF-3 acting as a donor.

268 nm^3) from that of the Förster volume ($(4\pi/3){R_0}^3 = 1243$ nm^3), $V_{RET,50}$ was calculated to be 975 nm^3. This value is applicable without any modifications to the QDs/IRMOF-3 core/shell composite (Figure 2-16b). However, when it is assumed that QD and IRMOF-3 come in contact with each other at one point, as in the case of the QD-supported sample, the volume of IRMOF-3 that can give its excitation energy over 50% efficiency is identical to the red area shown in Figure 2-16c. By calculating the volume of the corresponding spherical cap ($V = (\pi/3)(3R_0 - R_o')R_o'^2$), the value was calculated to be 129 nm^3. If it is assumed that the same number of QDs makes the core/shell composite and QD-

supported MOF with IRMOF-3 of similar size and shape, $V_{\mathrm{RET},50}$ of the former is larger than that of the latter by 7.6 times. However, the intensity ratios of shorter and longer lifetime components ($A_{\mathrm{DA}}/A_{\mathrm{D}}$), which represent the ratios of the donor material working as a donor to that consuming the excited energy by itself, obtained for the core/shell composite were 11 times larger than those for QD-supported IRMOF-3 (Table 1). The fact that both numbers are similar to each other implies that the discussion based on the volumetric factor is reasonable to some extent. More accurately, however, I need to consider the energy transfer in the framework of IRMOF-3. Figure 2-17a shows the distances between the neighboring aminoterephthalate linkers, and Figure 2-17b shows the estimated energy transfer rate between the linkers (homo-FRET) and between the QD and linker. Since the spectral overlap integral for the absorption and PL of the linker in IRMOF-3 was 60,000 times smaller than that for the emission of the linker and absorption of the QDs, the energy transfer rate between the linkers are small considering the closeness of the distance. Only the energy transfer between the nearest ligands (0.93 nm) is competing to that from the linker to QD, which means that the antenna effect may be extended by ca. 1–2 nm due to the energy migration in the IRMOF-3. In any case, the obtained results clearly indicate the advantages of my strategy in making direct bonds between QDs and MOFs.

(a)

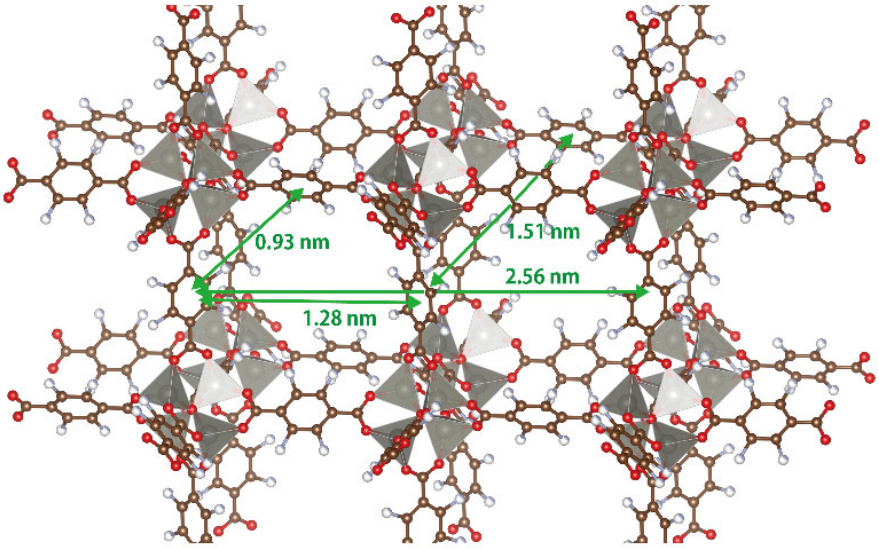

(b)

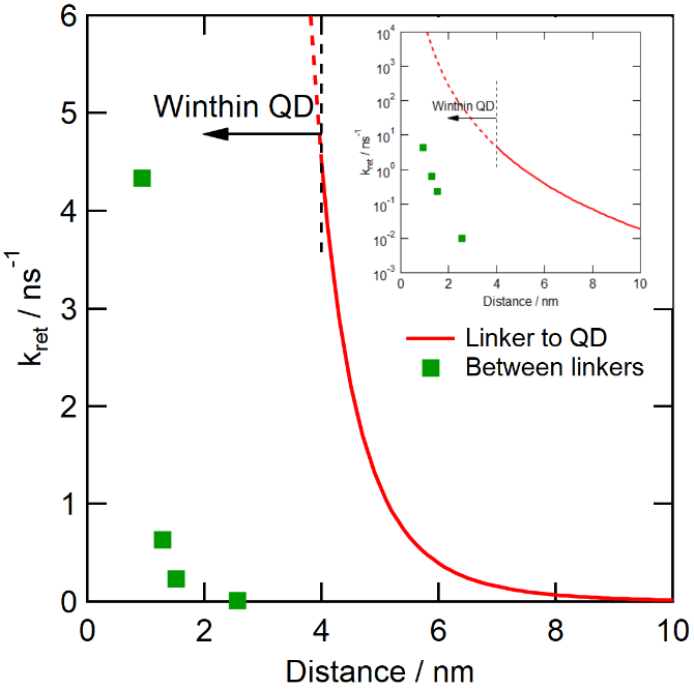

Figure 2-17. Crystal structure of IRMOF-3 indicating the distance between neighboring 2-aminoterephthalate linkers (a), and the comparisons of energy transfer rate calculated from Förster equation using spectral overlap between the linkers (green filled square, corresponding to the distances in a) and between QDs and linkers (red line) (b). Dipole orientation factor was fixed to κ^2=2/3 for simplicity. Since point charge model (see discussion in the last paragraph of main text) was adopted, the distance blow 4 nm (radius of QDs including ZnS shell) was excluded from consideration. The inset shows single logarithmic version of the same plot.

2-4. Summary

I demonstrated the PL enhancement of semiconductor QDs owing to the energy transfer from a light-harvesting IRMOF-3 surrounding each QD as a surface modifier. The efficiency of the energy transfer was 11 times higher when CdSe/CdS/ZnS core/multishell QDs were fully covered by IRMOF-3 (QDs/IRMOF-3 core/shell composite) compared to when QDs were only attached to the surface of IRMOF-3 (QD-supported IRMOF-3). The advantage of the acceptor/donor core/shell structure for efficient energy transfer was explained by the volumetric factor of IRMOF-3 from which excitation energy was transferred to QDs, and the PL intensity of the QDs when excited at the absorption maximum of IRMOF-3 shell was almost doubled from the pristine QDs. This work clearly shows the usability of MOFs not only as matrices that can secure necessary distance between QDs to suppress self-quenching[87] but also as light-harvesting materials to enhance the photoluminescence emitted from QDs. This fascinating optical function is useful when QDs/MOF core/shell materials are applied for the fabrication of optical devices such as wavelength convertor and solar cell.

Chapter 3

Variations in Photoluminescence Intensity of a Quantum Dot Assembly Investigated by its Adsorption on Cubic Metal–Organic Frameworks

3-1. Introduction

An entire nanoparticle, including a core, a shell, and surface ligands, contributes to the luminescence of QDs. Thus, even a minor variation in the structure can significantly alter its optical properties. Besides directly damaging the structure of the nanoparticle, a decrease in the PL intensity and the red-shift of QDs upon aggregation have been frequently reported and is becoming a common consideration in the development of QDs and QD-based devices.[98, 99] However, since aggregation is generally triggered by the damage to the surface ligands, and conversely, it may cause changes in the surface states, it is usually difficult to distinguish the factor that primarily affects the decrease in PL intensity. Another cause of PL quenching in aggregated QDs may be the loss of electrical independence, which is inevitable during emission.[98] The close-packed nature of the QD aggregate also changes the effective electric field that is experienced by the individual QDs, which causes the red-shift in PL spectra via the Stark effect.[100] In addition, even the excitation light that is unable to reach the center of the agglomerate would decrease the apparent PL intensity and reabsorption of PL by the neighboring particles generally causes the red-shift in the apparent PL spectra.

The aforementioned decrease and red-shift in the PL spectra (except the reabsorption of PL) are generally due to the changes in the state of the individual particles due to variations that are attributable to the electronic structure of QDs. Concurrently, the Förster resonance energy transfer (FRET), which is known to be an efficient energy transfer process that is induced by dipole–dipole coupling between a donor and an acceptor located within 10-nm distance, is a factor that causes a significant change in PL of QDs upon aggregation.[94] Efficiency of FRET depends on the distance between the donor and acceptor

and the spectral overlap between the emission from the donor and absorption by the acceptor.[101] Therefore, many researchers have focused on energy transfer between two materials (precisely referred to as hetero-FRET) because it is more remarkable and involves an exchange of the substantial quenching of the PL intensity of the donor fluorophore with an increase in the PL intensity of the acceptor.[102-108] Conversely, FRET between fluorophores of a single type is referred to as homo-FRET. Homo-FRET has been employed as a technique for bioimaging that enables observation of the assembly state by analyzing loss of the fluorescence anisotropy.[109, 110] However, homo-FRET is largely neglected in the research for fluorescent dyes because it does not theoretically exert any effect on PL intensity and lifetime,[101] i.e., the variation in fluorescence anisotropy is the only method for observing the interactions among fluorophores; hence, homo-FRET is not relevant for research aimed at the development of good fluorophores.

Nevertheless, the peculiar behavior of the emission from QDs in an assembled state regarding energy transfer between particles via optical techniques, which enable the observation of individual or a small number of nanoparticles, have been reported.[111-113] D.P. Shepherd *et al.* observed the second (shorter lifetime) component in the PL decay curves and the decrease in the "on" duration of the PL intermittency in the assembly of two to four QDs compared to a single QD.[111] They employed an *in situ* atomic force microscope to correlate the PL blinking data, which was recorded by a fluorescence microscope, with the actual number of QDs in the cluster and attributed the observed phenomena to the energy transfer from the nanoparticles with larger bandgap to that with a smaller one, considering the residual size distribution of QDs that were utilized in their study. More recently, D.P. Ryan *et al.* conducted similar measurements by performing a follow-up observation with a scanning electron microscope to count the nanoparticles in the cluster more accurately.[113] They confirmed that the PL intensity that was integrated within the mean time was weaker when QDs formed a cluster consisting of several nanoparticles than that expected when the PL intensity of a single particle was multiplied by the number of QDs in the

cluster. They also predicted that such a decrease in the PL intensity was caused by dark particles, in which particles that are never emissive and/or temporarily in an off state of blinking are included. These investigations on QD clusters by well-devised individual particle observation systems provided beneficial insights into energy transfer between QDs and predicted the limitations in the efficiency of QD-based electronic devices that adopt a condensed system to the extent that energy transfer occurs between QDs.

Thus, an interest area for researchers of QD devices is to what extent a QD assembly can affect their luminous efficiency under light irradiation of normal intensity. In this regard, a two-dimensional (2D) array of QDs is an ideal environment to answer and elucidate this phenomena, since it can deliver sufficient excitation light to all QDs as well as minimize the reabsorption of the generated PL.[114] In addition, the utilization of nanosized structures, which are dispersible in the solution, is favorable to obtain higher signal intensity than utilizing planar glass substrates. In fact, silica particles have often been utilized as supports for QDs during the analysis of energy transfer between QDs and different optical materials, such as metal nanoparticles and organic dyes.[77, 106, 115-117] However, QDs are hardly adsorbed on silica without special surface treatments, and the application of such surface modifications significantly changes the optical properties of QDs. The utilization of metal–organic frameworks (MOFs) is an attractive and alternative method of binding QDs to a support. First, MOFs are coordinating polymers that intrinsically expose many coordinating groups on their surfaces.[19, 20, 118] The functional groups, such as carboxylates and amines, which are arranged at equal intervals of ~1 nm, provide an ideal environment for binding metal and semiconductor nanoparticles. Further, the chemical similarity of these coordinating groups with the as-prepared QDs is advantageous to minimize the electronic effects on the body of the QDs. In addition, well-crystallized MOFs generally possess cubic or polyhedral shapes, which are positionally closer to a 2D plane than the curved surface of spherical silica beads.

This study investigates the changes in the PL properties of blue-, green-, and red-luminescent cadmium selenide (CdSe)-based core/shell QDs, when they are aligned two-dimensionally on MOF supports. MOF-5, which is one of the most chemically stable cubic MOFs that consist of nodes of octahedral zinc oxide cluster and terephthalate linkers, was utilized as the support.[21] Hetero-FRET was apparently observed when two different-colored QDs were supported together on MOF-5, and the magnitude of energy transfer correlated with the amount of QDs that was supported on the MOF. Interestingly, nonlinearity of the PL intensity with the loading amount of QDs was observed in all the cases where the same type of QDs was supported on the MOFs. However, the magnitudes of the deviation from the linearity were different among the various types of QDs. Further, these results were discussed for homo-FRET and the resulting "energy funnels" for temporarily or permanently dark nanoparticles.

3-2. Experimental section

3-2-1. Chemicals

Cadmium oxide (CdO), zinc oxide (ZnO), and 4-*tert*-butylpyridine were purchased from Sigma-Aldrich. Oleic acid (OA), 1-octadecene (ODE), S powder, zinc acetate [$Zn(OAc)_2$], pyridine, and zinc acetate dihydrate [$Zn(OAc)_2 \cdot 2H_2O$] were purchased from FUJIFILM Wako Pure Chemical Corporation. Further, trioctylphosphine (TOP), 1-dodecanethiol, tributylphosphine (TBP), zinc chloride ($ZnCl_2$), and terephthalic acid (H_2BDC) were purchased from Tokyo Chemical Industry Co., Ltd. Se powder was purchased from Mitsuwa Chemicals Co., Ltd. Zinc oleate [$Zn(OA)_2$] was synthesized by reacting ZnO in excess OA in an Ar atmosphere at 260°C and purifying the product with toluene/acetone.

3-2-2. Synthesis of blue CdZnS/ZnS QDs (QD440)

CdO (0.128 g, 1.0 mmol), $Zn(OAc)_2$ (1.835 g, 10 mmol), OA (7 mL, 22 mmol), and ODE (15 mL) were mixed in a 100-mL two-necked flask and evacuated for 30 min at 80°C. Thereafter, the temperature was increased to 300°C in an Ar atmosphere and maintained for 10 min to form a clear solution containing cadmium oleate [$Cd(OA)_2$] and $Zn(OA)_2$. Next, S (64.12 mg, 2.0 mmol), which was dissolved in ODE (3 mL), was quickly injected into the flask and the temperature was increased to 310°C to grow the CdZnS cores. After 8 min of reaction, S (256.48 mg, 8.0 mmol), which was dissolved in TBP (3 mL), was added dropwise to the CdZnS solution and the reaction solution was held at 310°C to form a ZnS shell. After 40 min of heating at 310°C, the flask was cooled to room temperature (25°C) and excess amount of acetone was added to precipitate QDs. The suspension was centrifuged, and the solid QDs were re-dispersed in hexane to attain CdZnS/ZnS QDs with a diameter of 8.6 nm, which was stabilized by OA.

3-2-3. Synthesis of green CdSe/ZnS QDs (QD525)

CdO (0.018 g, 0.14 mmol), $Zn(OAc)_2$ (0.626 g, 3.4 mmol), OA (7 mL, 22 mmol), and ODE (15 mL) were mixed in a 100-mL two-necked flask and evacuated for 30 min at 80°C. Thereafter, the temperature was increased to 300°C in an Ar atmosphere and maintained for 10 min to form a clear solution containing $Cd(OA)_2$ and $Zn(OA)_2$. Se (157.93 mg, 2.0 mmol) and S (64.12 mg, 2.0 mmol), which were dissolved in TOP (2 mL), were quickly injected into the flask and the temperature was increased to 310°C to grow CdSe/ZnS QDs. After 10 min of reaction, $Zn(OA)_2$ (2.512 g, 4 mmol), which was dissolved in ODE (8 mL), and S (128.24 mg, 4.0 mmol), which was dissolved in TOP (2 mL), were successively introduced into the CdSe/ZnS QD solution at the same temperature to overcoat the additional ZnS shell. After 10 min of heating at 300°C, the flask was cooled to room temperature and excess amount of acetone was added to precipitate the QDs. The suspension was centrifuged, and the solid QDs were re-dispersed in hexane to attain CdSe/ZnS QDs exhibiting a composition gradient and a diameter of 12.9 nm, which was stabilized by OA.

3-2-4. Synthesis of red CdSe/CdS/ZnS QDs (QD612)

CdO (0.128 g, 1.0 mmol), OA (1.27 mL, 4 mmol), and ODE (20 mL) were mixed in a 100-mL two-necked flask and evacuated for 30 min at 80°C. Thereafter, the temperature was increased to 300°C in an Ar atmosphere and maintained for 10 min to form a clear solution containing $Cd(OA)_2$. Next, Se (19.74 mg, 0.25 mmol), which was dissolved in TOP (0.25 mL), was quickly injected into the flask and the temperature was held at 300°C for 90 s to grow CdSe-core QDs. Subsequently, dodecanethiol (0.16 mL, 0.75 mmol) was added dropwise to the CdSe solution, and the reaction solution was held for 30 min at 300°C to form the CdS shell. Finally, $Zn(OAc)_2$ (0.734 g, 4.0 mmol), which was dissolved in OA (2.54 mL, 8.0 mmol), and S (0.128 g, 4.0 mmol), which was dissolved in TBP (0.2 mL), were sequentially injected into the reaction solution to form a ZnS shell. After 10 min of heating at 300°C,

the flask was cooled to room temperature, and excess amount of acetone was added to precipitate the QDs. The suspension was centrifuged, and the solid QDs were re-dispersed in hexane to attain CdSe/CdS/ZnS QDs with a diameter of 8.3 nm, which was stabilized by OA.

3-2-5. Nonpolar-to-polar ligand exchange

OA-capped QDs (QD440, QD525, and QD612) were purified by precipitating them with acetone/ethanol and re-dispersing them in hexane; this procedure was repeated three times. Thereafter, the solid QDs were dispersed in hexane (5 mg/mL). $Zn(OAc)_2 \cdot 2H_2O$ (87.8 mg, 0.4 mmol), $ZnCl_2$ (109.1 mg, 0.8 mmol), and dimethylformamide (DMF) (10 mL) were loaded into a flask and the mixture was held at 60°C with sonication until a clear and transparent solution was formed. For a typical ligand-exchange reaction, DMF solution containing hybrid ligands (2 mL) was obtained and mixed with hexane-dispersed QD solution (2 mL). The dual-layer solution was held at 50°C with stirring. After 60 min of heating, QDs were completely transferred from the upper hexane layer to the bottom DMF layer. The bottom QD suspension was centrifuged, and the solid QDs were mixed with the DMF solution containing the hybrid ligands (0.5 mL). Next, 4-*tert*-butylpyridine (0.5 mL) was added to the QD suspension and the mixture was heated at 80°C with stirring until a clear and transparent QD solution was obtained (QDs were stabilized by $Zn(OAc)_2$, $ZnCl_2$, and 4-*tert*-butylpyridine).

3-2-6. Synthesis of nanosized MOF-5

DMF solutions of $Zn(OAc)_2 \cdot 2H_2O$ (45 mM) and H_2BDC (22.5 mM) were separately prepared as MOF-5 precursor solutions. Pyridine (10 μL, 68 μmol), which was utilized as a modulating ligand, and DMF (12 mL) were mixed in a 50-mL flask and kept at room temperature with stirring. Thereafter, 45 mM $Zn(OAc)_2 \cdot 2H_2O$ (1 mL, 45 μmol) and 22.5 mM H_2BDC (1 mL, 22.5 μmol) were injected into the DMF solution by two syringes that were attached to a syringe pump with a flow rate of 5.0 mL/h. The

mixture was stirred for at least 1 h, after which portions of the MOF-5 suspension were utilized for subsequent experiments without any purification.

3-2-7. Synthesis of QD-supported MOF-5

The optical densities of the QD solution (QD440, QD525, and QD612), which were diluted 10 times, at 360 nm were adjusted to ~1.2 and utilized as standard QD stock solutions. For the hetero-FRET experiments, the QD mixture was prepared by mixing the QD525 and QD 612 stock solutions in the same ratios (QD525:QD612 = 1:1). In a typical synthesis process, the MOF-5 suspension (0.5 mL) was diluted with DMF (2 mL) and a predetermined amount of the QD stock solution (10, 30, or 50 μL) was injected into the MOF-5 solution. After the mixture was stirred for 30 min at room temperature, the obtained QD/MOF-5 composite, which was dispersed in DMF, was utilized for the optical measurements without any purification.

3-2-8. Characterization

All optical spectra (UV-vis, PL, PLQY, PLE, PL lifetime) were recorded in the same manner described in Chapter 2. TEM images were acquired in the same manner described in Chapter 1.

3-3. Results and discussion

3-3-1. Characterization of the QDs and QD-supported MOF-5

Cd-based high-fluorescent QDs with different emission wavelengths [440 (QD440), 525 (QD525), and 612 nm (QD612)] were prepared by one-batch methods with some modifications.[89, 119] The as-prepared oleic acid-capped QDs were ligand-exchanged with 4-*tert*-butylpyridine to make them soluble in dimethylformamide (DMF). In addition, a small amount of the mixture of zinc acetate [$Zn(OAc)_2$] and zinc chloride ($ZnCl_2$) was utilized as additives to facilitate the dissolution of QDs as *Z*-type ligands (Figure 3-1).[120] Notably, only PL QY of the green-emitting QD525 was significantly reduced from 65% to 21% after ligand exchange, whereas QD440 and QD612 largely maintained their initial values of 65% for QD440 and 71% for QD612, probably because the differences in their internal energy structures

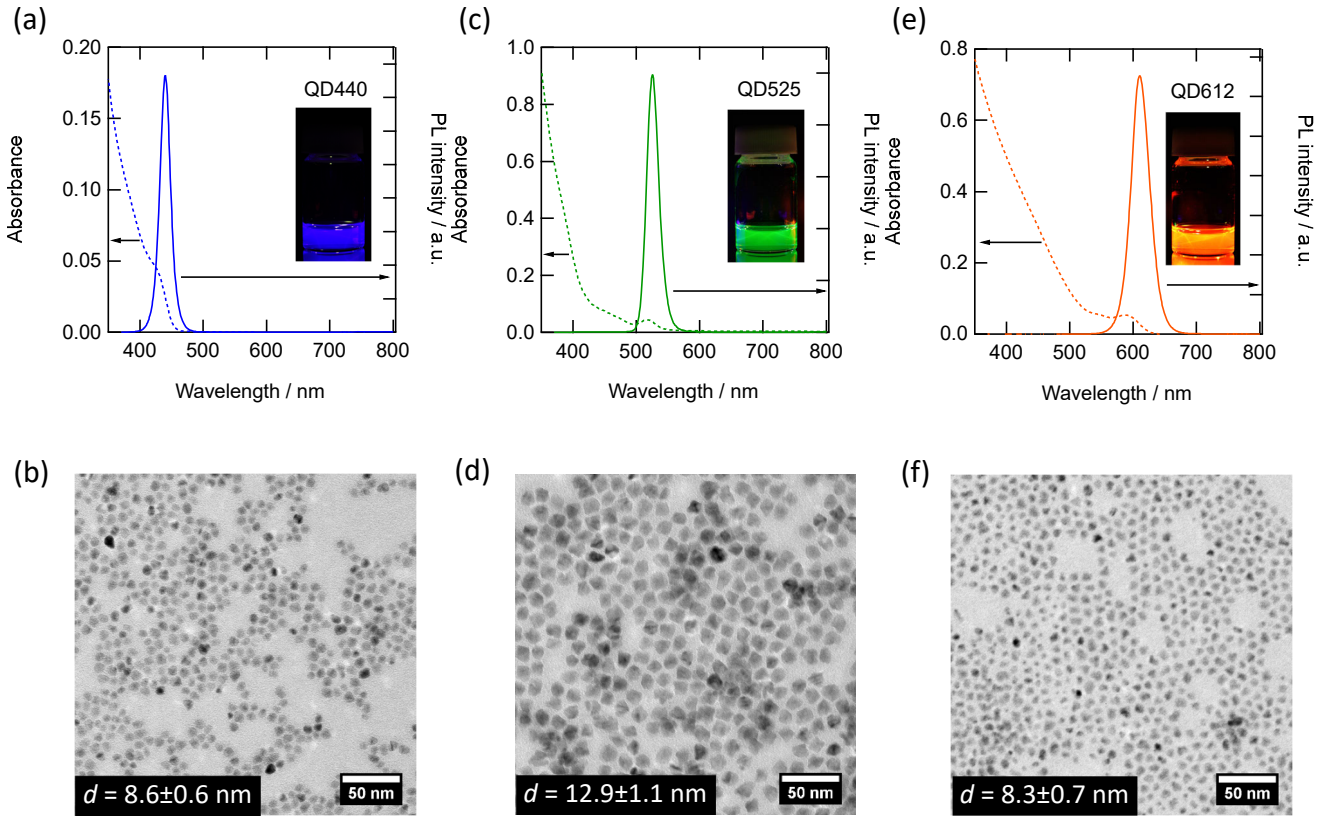

Figure 3-1. UV–vis and PL spectra (a, c, e) and TEM images (b, d, f) of QD440 (a, b), QD525 (c, d), and QD612 (e, f). The samples were dispersed in DMF for the optical measurements. The excitation wavelength was 360 nm for the PL spectra, and the inset photograph of each sample was obtained under UV irradiation.

affected their wave functions. The nanosized cubic MOF-5 crystals were synthesized by dropping DMF solutions of $Zn(OAc)_2$ and terephthalic acid separately into the prepared DMF solution containing pyridine, as reported by Wang *et al.*[121] The formation of nanosized MOF-5 with cubic shape (ca. 60 nm) was confirmed by TEM (Figure 3-2, Figure 3-3a).

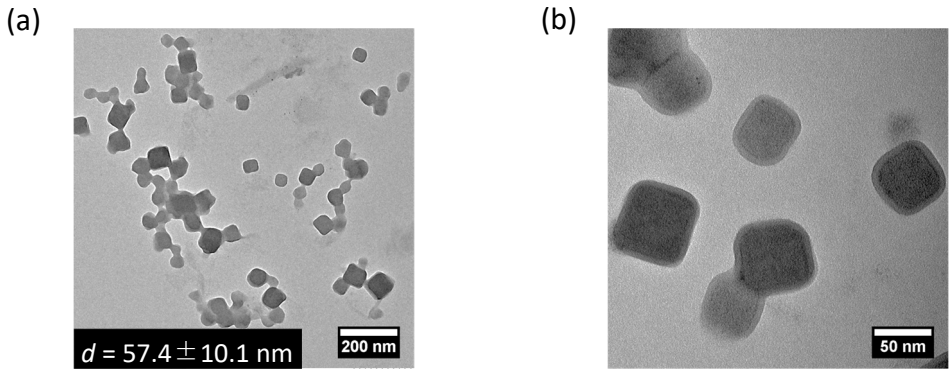

Figure 3-2. TEM images of the nanosized cubic MOF-5: overall (a) and magnified (b) images. The samples were synthesized by adding the MOF-5 precursors dropwise into DMF with a modulating ligand.

To reveal the adsorption of QDs on MOF-5 and the energy transfer in the adsorbed systems, two types of QDs (QD525 and QD612) were mixed in a ratio of equal optical densities at the excitation wavelength of 360 nm. Thereafter, 10, 30, and 50 μL of the mixture were added dropwise to the desired amount of DMF dispersion solution (0.5 mL each) of the nanosized cubic MOF-5. Figure 3-3b and 3c

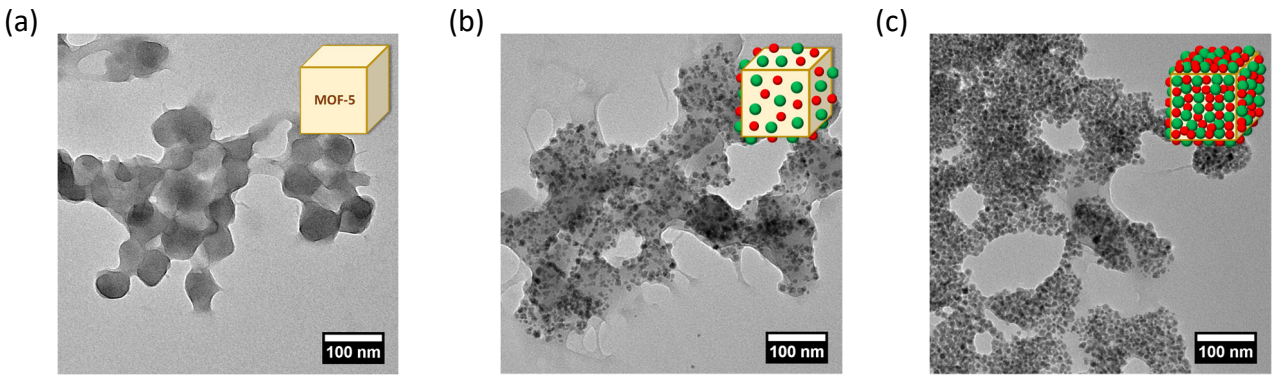

Figure 3-3. TEM images of the nanosized cubic MOF-5 (a) and QD-supported MOF-5 with different densities of QDs (b, c). To two-dimensionally align QDs on the MOF support, 10 (b) and 50 (c) μL of the QDs mixture were added into the DMF dispersion solution of the cubic MOF-5 crystals.

show the TEM images of the MOF-5 crystals on which QDs were firmly adsorbed when 10 µL (Figure 3-3b) and 50 µL (Figure 3-3c) of the QD mixture were dropped. The density of QDs that were adsorbed on MOF-5 increased when an increased amount of QDs was added to the cubic MOF-5 crystals, thereby reducing the distance between QDs. Notably, neither the separation of QDs and MOF-5 crystals nor the multilayered adsorption of QDs could be visually confirmed over the observation field of the TEM grid. Therefore, the spontaneous adsorption of QDs on MOF-5 after mixing both the materials was probably due to the coordination of the carboxyl groups that were exposed at the edge of MOF-5 to the Zn site on the surface of QDs (Figure 3-4).

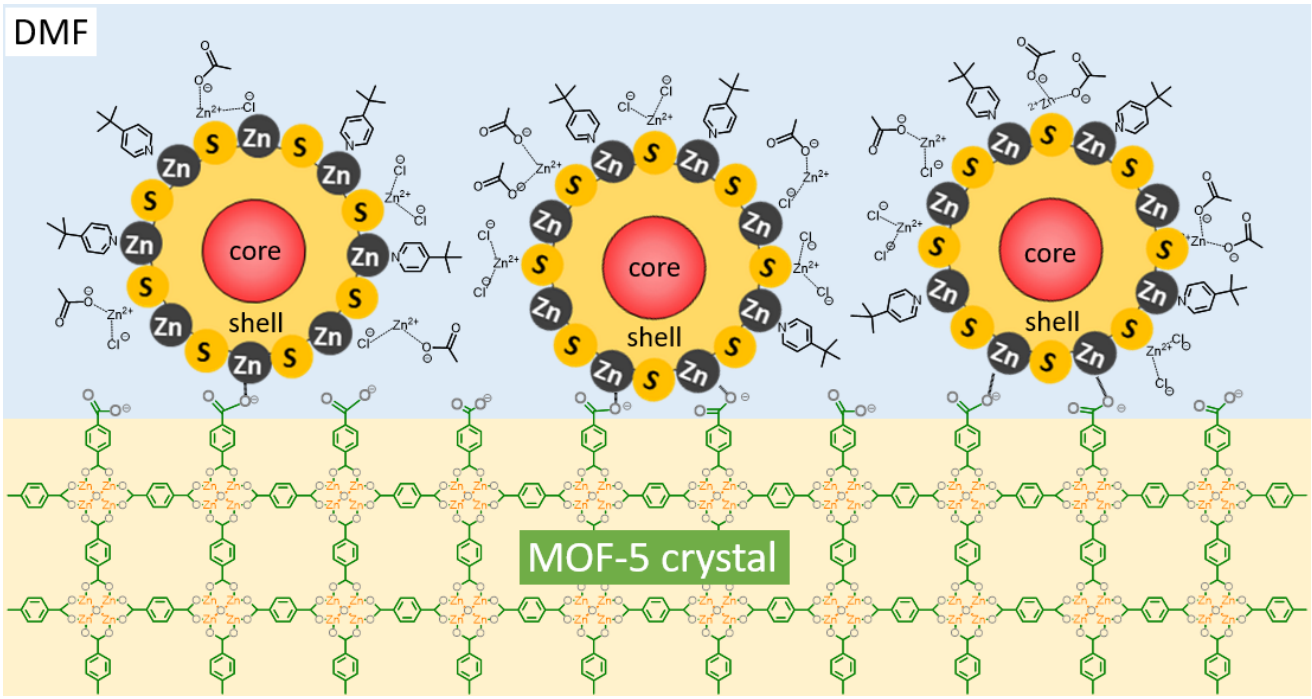

Figure 3-4. Schematic of the probable chemical interaction between quantum dots (QDs) and the nanosized cubic MOF-5. QDs can be easily adsorbed on the surface of MOF-5 via covalent bonds between the zinc atoms (QDs) and carboxylic acid (MOF-5).

3-3-2. Energy transfer from green- to red-emitting QDs (hetero-FRET)

Figure 3-5a shows the PL spectra that were normalized by the integrated intensities of the two peaks of the QDs mixture that was adsorbed on the cubic MOF-5 crystals when different amounts of the QD solution (10, 30, and 50 μL) were introduced. The ratio of the green luminescence from QD525 was substantially reduced as the amount of QDs was increased, whereas the ratio of the red luminescence from QD612 increased. Conversely, when the three volumes of the QD solution were dispersed in the same volume (0.5 mL) of DMF without MOF-5, the PL intensity ratios of the green and red luminescence were almost constant regardless of the concentration of QDs (Figure 3-5b). These results

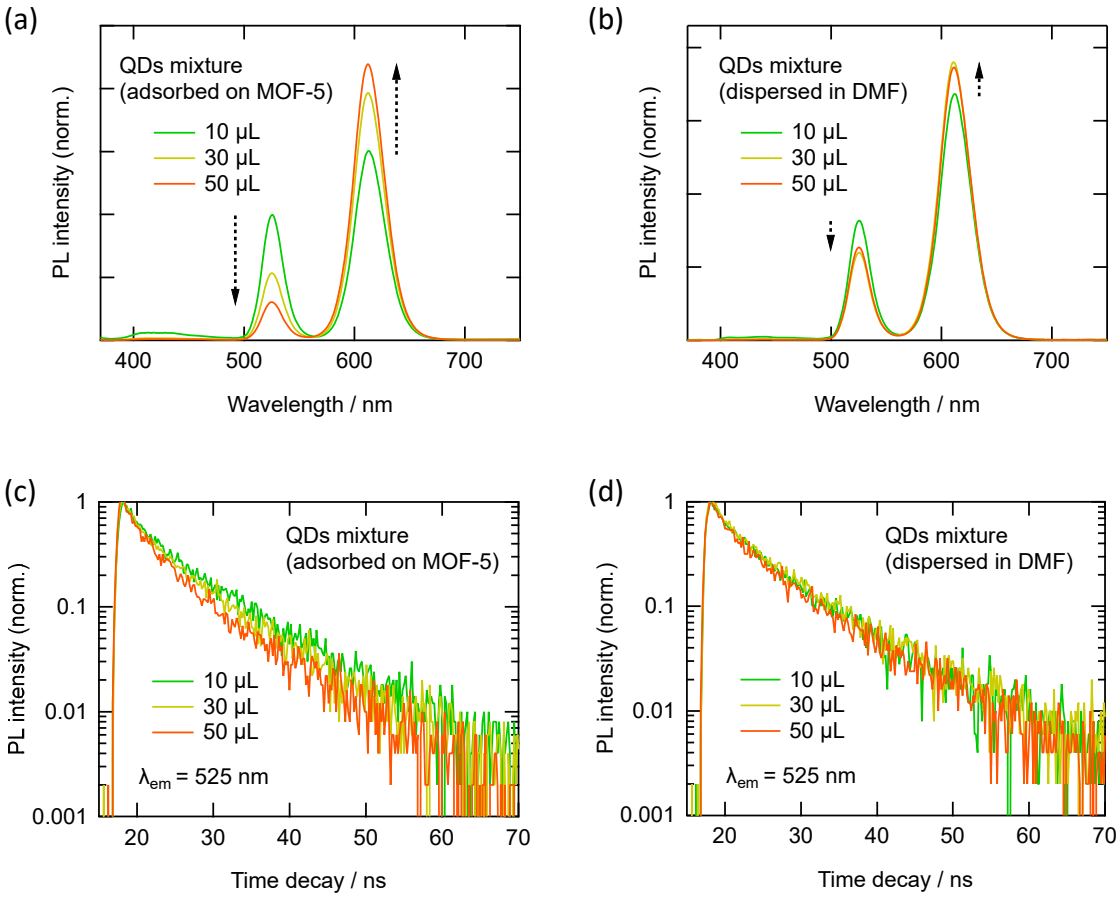

Figure 3-5. Normalized PL spectra of the QD mixture that was adsorbed on the cubic MOF-5 crystals (a) and QD mixture dispersed in DMF (b) with different densities of QDs. The excitation wavelength was 360 nm for the PL spectra. Donor PL decay curves of the QD mixture that was adsorbed on the cubic MOF-5 crystals (c) and QD mixture dispersed in DMF (d) recorded at an excitation and emission wavelength of 365 and 525 nm, respectively.

indicated that a high assembly of the QD mixture enhanced energy transfer from QD525 to QD612. Unfortunately, direct comparison of the PL intensity ratio of the 10-μL samples that were dispersed and supported on MOF-5 indicated an unexpected result, and the PL intensity ratio of QD612/QD525 was higher when QDs were dispersed in DMF than when they were supported on MOF-5, whereas the energy transfer was expected to be more favored in the latter case. Since this trend was consistent when the amount of QDs was further reduced, it was inferred that the higher ratio of the green emission was caused by light scattering by the cubic MOF-5, which typically exhibited wavelength dependency on the detection efficiency of the fluorospectrometer.

Thereafter, PL decay of the green emission from QD525 was measured to prove the occurrence of energy transfer. As expected from the results of the steady-state PL measurements, the decay rate increased when QDs were supported on MOF-5 and was almost unchanged when it was dispersed in DMF (Figures 3-5c and d). The decay curves were fitted by the following biexponential function:

$$I(t) = A_1 \exp\left(-\frac{t}{\tau_1}\right) + A_2 \exp\left(-\frac{t}{\tau_2}\right), \quad (1)$$

where, $I(t), A_i$, and τ_i are the decay curve, amplitude, and lifetime, respectively. Table 1 summarizes the results. Since QDs possess two emission components, the amplitude-weighted average lifetime was calculated by $(A_1{\tau_1}^2 + A_2{\tau_2}^2)/(A_1\tau_1 + A_2\tau_2)$ and displayed as $<\tau>$, and the values of $<\tau>$

Table 1. Fitting parameters of the PL decay curves of the QD mixture shown in Fig. 3-5c and d.

	QD amount (μL)	A_1	τ_1 (ns)	A_2	τ_2 (ns)	$<\tau>$ (ns)	χ^2
QDs dispersed in DMF	30	0.56	1.17	0.44	8.49	7.36	1.14
	10	0.53	1.35	0.47	8.36	7.29	1.08
QDs adsorbed on MOF-5	30	0.59	1.15	0.41	7.79	6.61	1.05
	50	0.67	0.82	0.33	6.86	5.67	1.02

were compared between the samples to evaluate the energy transfer. The average lifetimes of the dispersed samples containing the three volumes of the QDs were almost the same, and the 10-μL-supported sample obtained a value of $< \tau >$ very close to them. However, the lifetimes of the supported samples were substantially reduced when larger amounts of QDs (30 and 50 μL) were loaded on MOF-5, thereby demonstrating energy transfer from QD525 to QD612 at increased surface concentrations. Regarding the distance between the particles, the TEM image of the 10-μL-supported sample revealed an interparticle distance that was as large as 10 nm (Figure 3-3b), which is typically close to the distance limit for FRET. Conversely, the TEM image of the 50-μL-supported sample exhibited an almost saturated condition in the single-layer adsorption (Figure 3-3c). In other words, each particle was in contact with its neighboring particles. When QDs are so close, the occurrence of electronic coupling between QDs should be considered.[122] However, as expected, there were no traces of peak shift in the PL spectra for the green and red luminescence. Thus, the electronic coupling appeared to be negligible with minor contributions.

3-3-3. Energy transfer between the same types of QDs (homo-FRET)

Since hetero-FRET was validated in the two-dimensionally aligned QD mixtures with cubic MOF-5 crystals as a support, I investigated how energy transfer between the same types of QDs could affect the overall PL with the same MOF-5 support system. Each of the three types of QDs exhibiting emissions at different wavelengths (QD440, QD525, and QD612) were loaded on the surface of the MOF-5 crystals in the same manner as the QD mixture was loaded. As mentioned in the introduction, aggregation-induced PL quenching has been reported in many papers, and some of the reports attributed the quenching to energy transfer between QDs.[62, 123] Actually, the band-edge-emitting QDs were considered to be a system in which homo-FRET readily occurs due to relatively large spectral overlap between absorption and PL due to the minor Stokes shifts (the energy difference between the first exciton peak in the absorption spectrum and the emission peak was ~10 nm for CdSe-QDs). Figure 3-6 shows the photographs of the 50-μL supported MOF-5 under room and ultraviolet (UV) lights after the suspension was allowed to stand overnight until all the MOF-5 crystals were precipitated. The solution phase was colorless under room light (Figure 3-6a) and dark under the illumination from UV light (Figure 3-6b), which indicates that all the components of QDs were adsorbed on MOF-5. Briefly, the concentration of QDs was adjusted to be saturated on MOF-5 at 50 μL, above which a part of the components would remain in the solution phase after mixing with MOF-5.

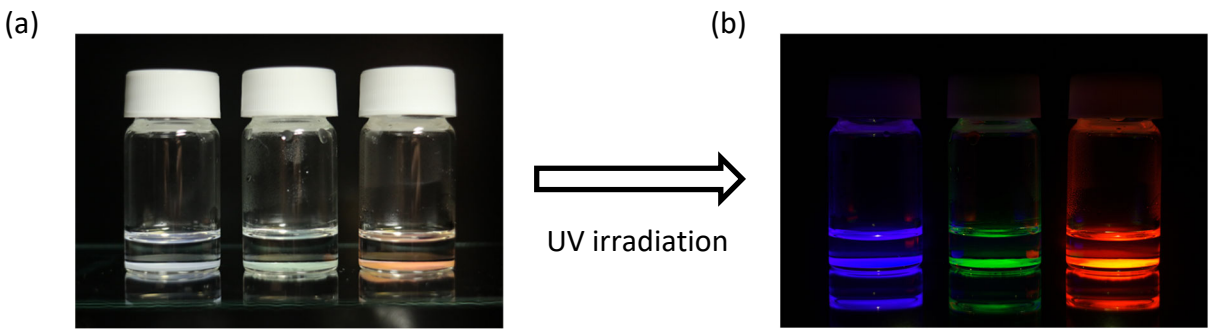

Figure 3-6. Photographs of QD-supported MOF-5 under room (a) and UV (b) lights. The samples were prepared by adsorbing 50 μL of QDs (QD440, QD525, or QD612) on cubic MOF-5 crystals.

Figure 3-7 shows the UV–Vis and PL spectra (recorded under the same conditions) of the blue-, green-, and red-emitting QD-supported MOF-5 crystals with three different loading amounts. The UV–Vis spectra for all the crystals (Figures 3-7, a–c) show monotonic increases at shorter wavelengths, and this was partly due to the Rayleigh scattering of the incident light and absorption by the supported QDs. Traces of absorption by QDs were barely noticeable as small shoulder peaks at the wavelength regions corresponding to the first exciton peak for each type of QDs. Conversely, the scattering intensity was substantially increased as the amount of QDs increased, and the amplitudes and spectral shapes regarding scattering for the three types of QDs were similar. Since almost no change was observed in the shape and size of the MOF-5 crystals via the TEM observations, I suspected that the variation of the scattering intensity was caused by the changes in the effective refractive index of the MOF-5 composites,

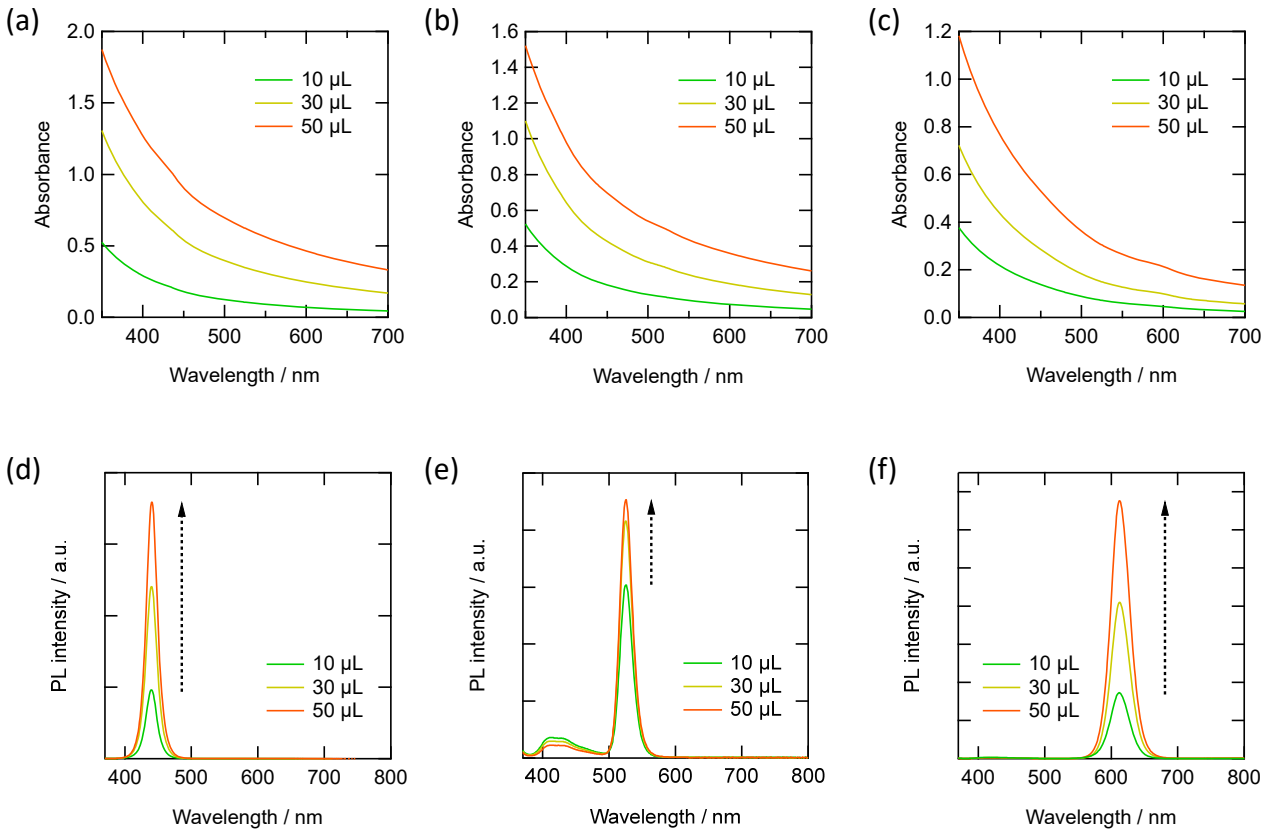

Figure 3-7. UV–vis (a, b, c) and PL (d, e, f) spectra of QD440 (a, b), QD525 (c, d), and QD612 (e, f) adsorbed on the cubic MOF-5 crystals with different QD number densities. The excitation wavelength was 360 nm for all PL spectra.

which was around $n = 1.3$ in the visible region, without an adsorbate, and expectedly increased upon adsorbing CdSe-QDs ($n = 2.5$ for the bulk CdSe). As the differences in the refractive index against DMF increased ($n = 1.4$), the scattering intensity also increased. The PL intensities of the corresponding samples (Figures 3-7, d–f), which were recorded under the same conditions (the same excitation wavelength, slit width, and applied voltage of the photomultiplier tube detector), significantly increased with increased amount of QDs loaded on MOF-5, except for green-emitting samples (Figure 3-7e). Figure 3-8 plots the PL peak intensities of the three types of QD-supported MOF-5 crystals, where the intensities were rescaled to 1 at 10 μL for each type of the QDs (blue, green, and red), i.e., the PL intensities should be proportional to the amount of QDs (dotted line in the same figure) if there is no effect of the QD assembly on the emission intensity. However, the recorded PL intensities were less than what was expected from the proportional relationships for all the types of QDs, and it was particularly remarkable for the green-emitting QD525 sample. Notably, no changes were observed in the emission peak wavelengths upon loading the samples on MOF-5 (Figure 3-9, a–c), which was more noticeable compared with the 5-nm red shift observed when each of the three types of QDs possessing

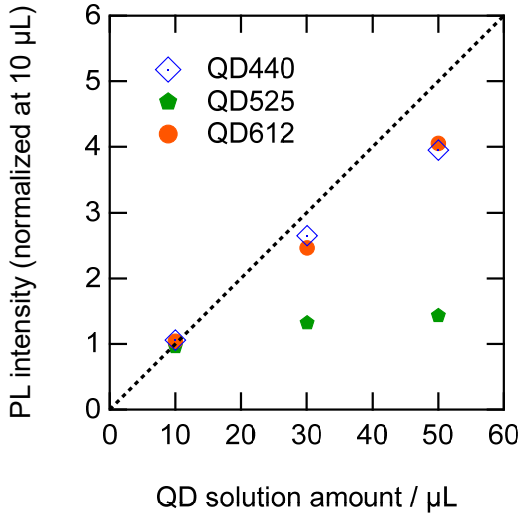

Figure 3-8. PL peak intensities of the three types of QD-supported MOF-5 crystals that were shown in Figure 3-7d-f. Intensities were rescaled to become 1 at 10 μL for each type of QDs (blue, green, and red).

original ligands was spun on glass substrates (Figure 3-9, d–f). This implied that the 2D QD assembly on MOF-5 excluded the reabsorption of light and/or the Stark effect, both of which originate from three-dimensionally close-packed cases and typically caused the red shift in luminescence.[100, 123] In other words, the reduced PL intensities than that expected were solely due to the effect of energy transfer between QDs.

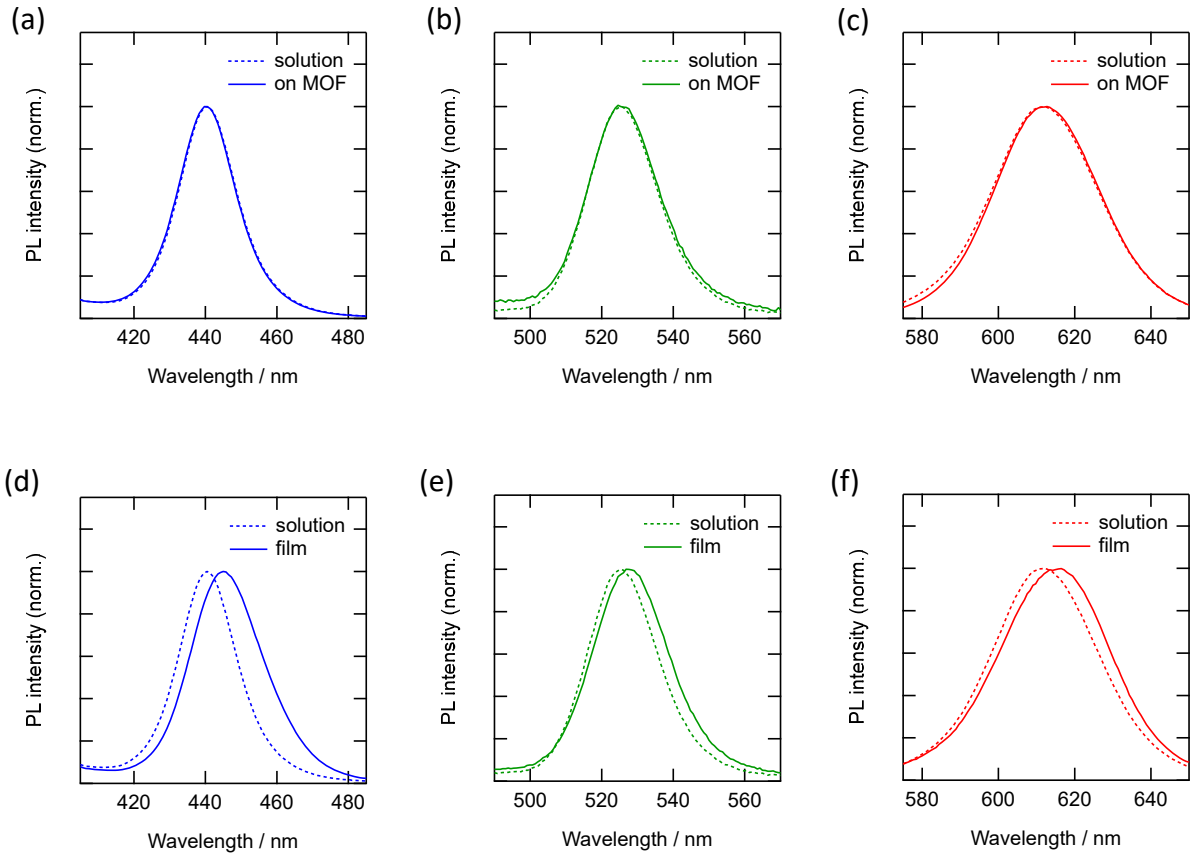

Figure 3-9. Normalized PL spectra of QD440 (a, d), QD525 (b, e), and QD612 (c, f) that were densely supported on cubic MOF-5 crystals (a, b, c) and spin-coated on glasses (d, e, f). The dotted lines in each figure show the PL spectrum of the sample that was dispersed in DMF. The excitation wavelength was 390 nm for the PL spectra.

Figure 3-10 indicate the PL decay curves for the three types of QD-supported MOF-5 with different amounts of QDs, and Table 2 summarizes the fitting parameters for the nine measurements. The lifetime of QD525 was noticeably reduced as the amount of QDs loaded on MOF-5 increased, whereas those of QD440 and QD612 were almost unchanged. Since the average PL lifetime, $< \tau >$, of the ligand-exchanged 4-*tert*-butylpyridine-capped QD525 in the DMF solution was 7.4 ns, its decrease was limited for the 10-μL sample (7.0 ns), above which it substantially reduced. When the magnitude of quenching for QD525 that was loaded on MOF-5 was calculated from the variations of $< \tau >$, the ratios of the PL lifetimes of the supported samples were 0.83 and 0.64 for the 30- and 50-μL samples, respectively. The ratios were higher than the steady-state PL intensities divided by the PL intensities that were expected from the extrapolation of the 10-μL sample (the dotted line in Figure 3-8), which were 0.46 and 0.30 for the 30- and 50-μL samples, respectively. These results suggested the existence of nonluminescent particles and/or those possessing PL lifetimes that are lower than the detection limit of the time-correlated single-photon counting setup (<100 ps). The existence of dark particles was expected if PL QY of the ligand-exchanged QD525 (21%), which is much lower than those of the other two types of QDs (65% for QD440 and 71% for QD612), was considered. In addition, an increased number of QDs appeared to switch to the dark or dim state when they were loaded on MOF-5 at high concentrations because of energy transfer between the assembled QDs.

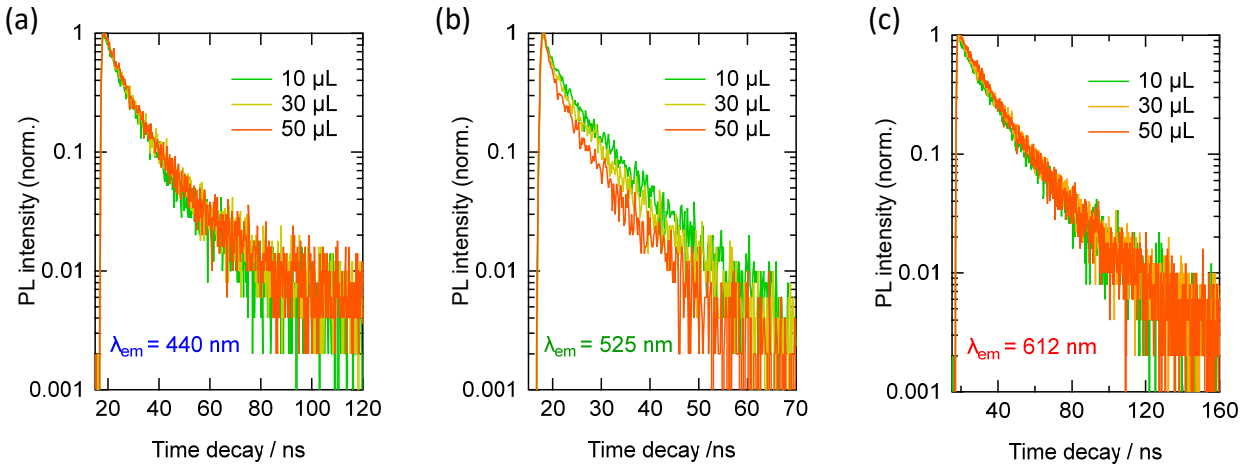

Figure 3-10. PL decay curves for QD440 (a), QD525 (b) and QD612 (c) that were adsorbed on the cubic MOF-5 crystals with different densities of QDs that were recorded at an excitation wavelength of 365 nm and emission wavelength of 440, 525, or 612 nm.

Table 2. The fitting parameters for the PL decay curves of several QDs (QD440, QD525 and QD612) adsorbed on the surface of cubic MOF-5 crystals shown in Figure 5a-c.

Sample	QD amount (µL)	PL peak (nm)	A_1	τ_1 (ns)	A_2	τ_2 (ns)	$<\tau>$ (ns)	χ^2
QD440	10	440	0.49	3.28	0.51	11.43	9.66	1.10
	30	440	0.60	4.19	0.40	13.58	10.57	1.18
	50	440	0.62	4.60	0.38	13.93	10.62	1.19
QD525	10	525	0.60	1.08	0.40	8.21	7.00	1.14
	30	525	0.65	1.12	0.35	7.55	6.15	1.02
	50	525	0.74	0.76	0.26	6.14	4.75	1.10
QD612	10	612	0.38	3.02	0.62	18.46	17.06	1.13
	30	613	0.31	3.65	0.69	19.10	17.86	0.99
	50	612	0.33	6.00	0.67	18.82	17.08	1.06

3-3-4. Theoretical evaluation for energy transfer

The affirmation of energy transfer between the same types of QDs that were supported on MOF-5 is required to explain the considerable PL quenching of QD525 in an assembled state. The Förster distances (R_o) of homo-FRET for each type of QDs were calculated according to the equation explained in chapter 2. Table 3 summarizes the photochemical properties of the three types of QDs. Owing to the large extinction coefficients and spectral overlap between the absorption and PL, the calculated R_o (the distance at which the energy transfer rate becomes equal to the internal recombination) reached 7–8 nm, which was substantially longer than the typical values for organic fluorophores (1–2 nm). Therefore, energy transfer between QDs possibly happens at a high rate when they are supported on MOF-5 at a nearly saturated concentration. However, in the first place, homo-FRET does not affect PL QY and the lifetime of a fluorophore ensemble,[101] and the existence of nonemissive or temporarily dark QDs are required to explain these phenomena (Figure 3-11). The mechanism is similar to that reported by H. Kashida *et al.*, who clarified the energy migration between two or more identical fluorophore molecules.[124] By strictly controlling the intermolecular distances in the double strand of DNA, they observed more-than-expected quenching when a quencher molecule was introduced to the system because of crosstalk of the excitation energy between the fluorophores. In addition, energy transfer, which occurred in the 2D ensemble of QD525, may contain clues to answer the question about the occurrence of energy transfer between QDs. Although QD525 possessed an average diameter of 12.9 nm, which is sufficiently larger than the R_o (7.0 nm), homo-FRET tended to occur at a detectable rate. These results led to approach the question about discussing the energy transfer of QDs by treating them as points in a manner similar to other organic fluorophores. How to define the interparticle distance for the core/shell QDs that are close to each other would elucidate the design criteria for producing good QD-based devices.

Table 3. Selected photochemical properties of QD440, QD525, and QD612

QD	QD440	QD525	QD612
Core/shell composition	CdZnS/ZnS	CdSe/ZnS	CdSe/CdS/ZnS
Diameter (nm) [a]	8.6	12.9	8.3
QY [b]	0.65	0.21	0.71
λ_{first} (nm) [c]	431	517	588
ε_{first} (M^{-1} cm^{-1}) [d]	1170000	747000	264000
Overlap integral $J \times 10^{16}$ (M^{-1} cm^{-1} nm^4)	2.5	3.9	1.8
Förster distance R_0 (nm)	7.9	7.0	7.3

[a] Representative TEM data in Figure 3-2. [b] Quantum yields of QDs that were well-dispersed in DMF. [c] Wavelength of the first exciton peak. The value was estimated by the local minimum on the second derivative of QD440. [d] Approximate molar absorption coefficient at the first exciton peak.

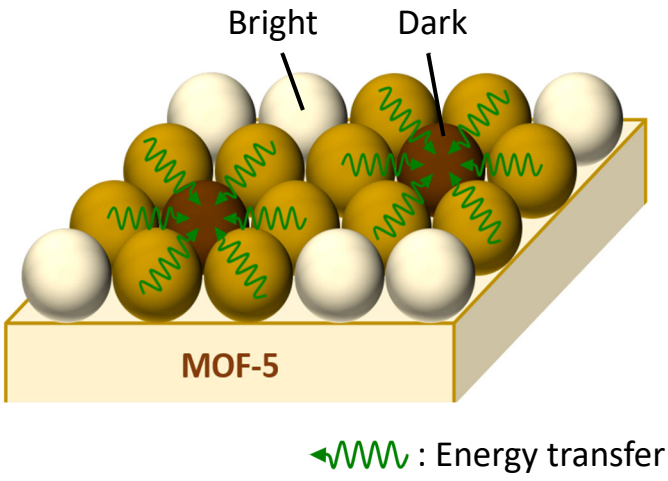

Figure 3-11. Schematic illustration of FRET-induced quenching mechanism in the two-dimensional ensemble of QDs. The PL intensity of ensemble is decreased more than necessary by energy transfer between the neighboring QDs that funnels exciton energy to dark particles.

3-4. Summary

In conclusion, this study proposed a new method for producing 2D arrays of QDs utilizing cubic MOF-5 crystals as the support. Owing to the carboxyl-terminal groups in the structure of MOF-5, QDs were instantaneously adsorbed on it (size = 60 nm) after mixing the two materials. When a mixture of two types of QDs exhibiting different emission wavelengths was adsorbed on MOF-5, energy transfer between the adsorbed QDs (hetero-FRET) occurred and the longer-wavelength PL was remarkably enhanced by an increase in the surface concentration of QDs on MOF-5. Conversely, when the same type of QDs were adsorbed on MOF-5 with various amounts of the particles, the increase in the PL intensity became less than that expected in proportional to the amount of QDs. Particularly, the green-emitting QD525 exhibited PL intensity of only 1/4 of that expected at the saturated surface concentration. The decrease in the PL intensity of the ensemble was caused by the existence of dark particles and energy transfer between the neighboring QDs (homo-FRET) that funneled the exciton energy to the dark particles and unnecessarily reduced the PL intensity of the ensemble. The observed phenomenon is one of the factors of the aggregation-induced self-quenching of QDs that has been reported before, although it has never been isolated as a single setback that is caused by homo-FRET. The differences in the effect of PL quenching of the assembly may be due to the structural differences of the three types of QDs that were synthesized here and might be related to the area of the exciton distribution in a particle, which is typically determined by the energy band structures of the core/shell QDs. This method could offer a design guideline for fabricating QD-based electronic devices that utilize the material in highly concentrated environments.

Conclusions

This thesis described the demonstration of new optical functional materials based on the technology to make contacts between semiconductor QDs and MOFs in the absence of buffer layers, which was developed for the first time in my research. The direct bonding was very favorable to exert synergetic effects of the two materials, and many advantages such as the improvement of the stability of QDs and PL enhancement by light harvesting with photoluminescent MOFs were confirmed by optical measurements. Among the attempts to make composite materials, the merits of QD/MOF core/shell type composites, which is the configuration to cover the entire surface of QDs, were outstanding since the surface is as important as the core crystals themselves for QDs and greatly affects the optical properties. Besides, I incidentally found the strong adsorptive force working between QDs and certain types of MOFs during a series of experiments, and considered a method to leverage the phenomenon. The investigations using the former materials, the QD/MOF core/shell composites, were mainly described in chapter 1 and chapter 2, while the fundamental studies on the nature of QDs and their assembly performed by using the latter phenomenon, the strong adsorptive force between QDs and MOFs, were mentioned in chapter 3.

In chapter 1, a new strategy for developing a QD/MOF core/shell composite was proposed and mentioned, which was the bonding of QDs and MOFs without using any third materials to help adhesion between them. Ligand exchange to easily detachable pyridine derivatives, as well as precise concentration control of MOF precursors in QDs solution, demonstrated the direct growth of MOFs on the surface of QDs. Complete coverage of MOFs on the QD surface was demonstrated by both TEM observation and PL quenching measurements. Owing to an insulating MOF (e.g. ZIF-8) working as a thick stabilizer for QDs, the resulting QD/ZIF-8 core/shell composite was demonstrated to emit an intense photoluminescence even in the solid state over a long period of years. These results strongly support that MOF functions well as a next-generation surface stabilizer for QDs. In addition, a direct

bond between QDs and MOFs is desirable to facilitate energy and electron transfer between two materials, which is essential for exploiting synergistic effects.

Chapter 2 describes the introduction of a fluorescent IRMOF-3 as a surface modifier for QDs in place of previous ZIF-8 to impart light harvesting effect to the core/shell composites. Photoluminescence emitted from QDs acceptor was properly enhanced (almost doubled) by efficient energy transfer from the IRMOF-3 donor surroundings QDs. The volumetric factor of IRMOF-3 from which excitation energy was transferred to QDs was estimated based on the theory of FRET, which suggested acceptor/donor core/shell structure was ideal for efficient energy transfer. This study showed MOFs can be worked not only as surface stabilizers for QDs as demonstrated in chapter 1, but also as light-harvesting materials to enhance the photoluminescence emitted from QDs. This fascinating optical function is quite beneficial when the QDs/MOF core/shell composites are introduced to optical devices such as wavelength convertor and solar cell.

In chapter 3, a new method to investigate the decrease in PL intensity of QDs ensemble was proposed and demonstrated. The basic strategy was to use a strong adsorptive force working between cubic crystals of MOF-5 and QDs. Owing to the evenly spaced adsorption sites on the MOF surface, the distance between QDs was properly controlled according to the QDs concentration. Then, two-dimensional arrays of 3-types of QDs were fabricated on the MOF with different QD number density. The PL intensity of ensemble was decreased more than the value according to the amount of the non-fluorescent particles, reducing the brightness of fluorescent particles by funneling exciton energy to nonfluorescent ones. This study enables the isolation of homo-FRET as a single problem of PL intensity variation caused by assembly, which provides useful information when using QDs at high concentrations as components for solid devices.

References

1. A. P. Alivisatos, *Science* **1996**, *271*, 933-937.
2. J. A. Smyder, T. D. Krauss, *Mater. Today* **2011**, *14*, 382-387.
3. A. M. Smith, S. Nie, *Acc. Chem. Res.* **2010**, *43*, 190-200.
4. L. A. Padilha, G. Nootz, P. D. Olszak, S. Webster, D. J. Hagan, E. W. Van Stryland, L. Levina, V. Sukhovatkin, L. Brzozowski, E. H. Sargent, *Nano Lett.* **2011**, *11*, 1227-1231.
5. Y. Yuan, H. Zhu, X. Wang, D. Cui, Z. Gao, D. Su, J. Zhao, O. Chen, *Chem. Mater.* **2019**, *31*, 2635-2643.
6. W. Nan, Y. Niu, H. Qin, F. Cui, Y. Yang, R. Lai, W. Lin, X. Peng, *J. Am. Chem. Soc.* **2012**, *134*, 19685-19693.
7. O. Chen, J. Zhao, V. P. Chauhan, J. Cui, C. Wong, D. K. Harris, H. Wei, H. S. Han, D. Fukumura, R. K. Jain, M. G. Bawendi, *Nat Mater* **2013**, *12*, 445-451.
8. I. L. Medintz, H. T. Uyeda, E. R. Goldman, H. Mattoussi, *Nat Mater* **2005**, *4*, 435-446.
9. T. Jamieson, R. Bakhshi, D. Petrova, R. Pocock, M. Imani, A. M. Seifalian, *Biomaterials* **2007**, *28*, 4717-4732.
10. E. Jang, S. Jun, H. Jang, J. Lim, B. Kim, Y. Kim, *Adv. Mater.* **2010**, *22*, 3076-3080.
11. J. McKittrick, L. E. Shea-Rohwer, D. J. Green, *J. Am. Ceram. Soc.* **2014**, *97*, 1327-1352.
12. F. Meinardi, A. Colombo, K. A. Velizhanin, R. Simonutti, M. Lorenzon, L. Beverina, R. Viswanatha, V. I. Klimov, S. Brovelli, *Nature Photonics* **2014**, *8*, 392-399.
13. J. H. Koo, D. C. Kim, H. J. Shim, T. H. Kim, D. H. Kim, *Adv. Funct. Mater.* **2018**, *28*, 1801834.
14. H. Shen, Q. Gao, Y. Zhang, Y. Lin, Q. Lin, Z. Li, L. Chen, Z. Zeng, X. Li, Y. Jia, S. Wang, Z. Du, L. S. Li, Z. Zhang, *Nature Photonics* **2019**, *13*, 192-197.
15. Z. Yang, M. Gao, W. Wu, X. Yang, X. W. Sun, J. Zhang, H.-C. Wang, R.-S. Liu, C.-Y. Han, H. Yang, W. Li, *Mater. Today* **2019**, *24*, 69-93.
16. D. A. Hines, P. V. Kamat, *ACS Appl Mater Interfaces* **2014**, *6*, 3041-3057.
17. J. Owen, *Science* **2015**, *347*, 615-616.
18. O. M. Yaghi, M. O'Keeffe, N. W. Ockwig, H. K. Chae, M. Eddaoudi, J. Kim, *Nature* **2003**, *423*, 705-714.
19. S. Kitagawa, R. Kitaura, S. Noro, *Angew. Chem. Int. Ed. Engl.* **2004**, *43*, 2334-2375.
20. H. Furukawa, K. E. Cordova, M. O'Keeffe, O. M. Yaghi, *Science* **2013**, *341*, 1230444.
21. M. Eddaoudi, J. Kim, N. Rosi, D. Vodak, J. Wachter, M. O'Keeffe, O. M. Yaghi, *Science* **2002**, *295*, 469-472.
22. H. Li, K. Wang, Y. Sun, C. T. Lollar, J. Li, H.-C. Zhou, *Mater. Today* **2018**, *21*, 108-121.
23. F. Vermoortele, B. Bueken, G. Le Bars, B. Van de Voorde, M. Vandichel, K. Houthoofd, A. Vimont, M. Daturi, M. Waroquier, V. Van Speybroeck, C. Kirschhock, D. E. De Vos, *J. Am. Chem. Soc.* **2013**, *135*, 11465-11468.
24. L. Zhu, X. Q. Liu, H. L. Jiang, L. B. Sun, *Chem. Rev.* **2017**, *117*, 8129-8176.
25. Q. Wang, D. Astruc, *Chem. Rev.* **2020**, *120*, 1438-1511.
26. B. Liu, H. Shioyama, T. Akita, Q. Xu, *J. Am. Chem. Soc.* **2008**, *130*, 5390-5391.
27. J. Zhuang, C. H. Kuo, L. Y. Chou, D. Y. Liu, E. Weerapana, C. K. Tsung, *ACS Nano* **2014**, *8*, 2812-2819.
28. D. Sheberla, J. C. Bachman, J. S. Elias, C. J. Sun, Y. Shao-Horn, M. Dinca, *Nat Mater* **2017**, *16*, 220-224.
29. D. V. Talapin, I. Mekis, S. Götzinger, A. Kornowski, O. Benson, H. Weller, *The Journal of Physical Chemistry B* **2004**, *108*, 18826-18831.
30. R. Li, W. Zhang, K. Zhou, *Adv. Mater.* **2018**, *30*, e1705512.
31. E. A. Dolgopolova, A. M. Rice, C. R. Martin, N. B. Shustova, *Chem. Soc. Rev.* **2018**, *47*, 4710-4728.
32. J. Aguilera-Sigalat, D. Bradshaw, *Coord. Chem. Rev.* **2016**, *307*, 267-291.
33. S. Hermes, M. K. Schroter, R. Schmid, L. Khodeir, M. Muhler, A. Tissler, R. W. Fischer, R. A. Fischer, *Angew. Chem. Int. Ed. Engl.* **2005**, *44*, 6237-6241.

34. M. Sabo, A. Henschel, H. Froede, E. Klemm, S. Kaskel, *J. Mater. Chem.* **2007**, *17*, 3827-3832.
35. D. W. Lim, J. W. Yoon, K. Y. Ryu, M. P. Suh, *Angew. Chem. Int. Ed. Engl.* **2012**, *51*, 9814-9817.
36. Y. Z. Chen, Q. Xu, S. H. Yu, H. L. Jiang, *Small* **2015**, *11*, 71-76.
37. J. He, Z. Yan, J. Wang, J. Xie, L. Jiang, Y. Shi, F. Yuan, F. Yu, Y. Sun, *Chem Commun (Camb)* **2013**, *49*, 6761-6763.
38. T. Wakaoka, K. Hirai, K. Murayama, Y. Takano, H. Takagi, S. Furukawa, S. Kitagawa, *J. Mater. Chem. C* **2014**, *2*, 7173-7175.
39. S. Bhattacharyya, D. Rambabu, T. K. Maji, *Journal of Materials Chemistry A* **2019**, *7*, 21106-21111.
40. T. Tsuruoka, H. Kawasaki, H. Nawafune, K. Akamatsu, *ACS Appl Mater Interfaces* **2011**, *3*, 3788-3791.
41. D. Buso, J. Jasieniak, M. D. Lay, P. Schiavuta, P. Scopece, J. Laird, H. Amenitsch, A. J. Hill, P. Falcaro, *Small* **2012**, *8*, 80-88.
42. G. Lu, S. Li, Z. Guo, O. K. Farha, B. G. Hauser, X. Qi, Y. Wang, X. Wang, S. Han, X. Liu, J. S. DuChene, H. Zhang, Q. Zhang, X. Chen, J. Ma, S. C. Loo, W. D. Wei, Y. Yang, J. T. Hupp, F. Huo, *Nat Chem* **2012**, *4*, 310-316.
43. L. He, Y. Liu, J. Liu, Y. Xiong, J. Zheng, Y. Liu, Z. Tang, *Angew. Chem. Int. Ed. Engl.* **2013**, *52*, 3741-3745.
44. P. Wang, J. Zhao, X. Li, Y. Yang, Q. Yang, C. Li, *Chem Commun (Camb)* **2013**, *49*, 3330-3332.
45. L. Chen, Y. Peng, H. Wang, Z. Gu, C. Duan, *Chem Commun (Camb)* **2014**, *50*, 8651-8654.
46. S. Saha, G. Das, J. Thote, R. Banerjee, *J. Am. Chem. Soc.* **2014**, *136*, 14845-14851.
47. W. Zhang, G. Lu, S. Li, Y. Liu, H. Xu, C. Cui, W. Yan, Y. Yang, F. Huo, *Chem Commun (Camb)* **2014**, *50*, 4296-4298.
48. J. Zhou, P. Wang, C. Wang, Y. T. Goh, Z. Fang, P. B. Messersmith, H. Duan, *ACS Nano* **2015**, *9*, 6951-6960.
49. S. Wang, Y. Fan, J. Teng, Y. Z. Fan, J. J. Jiang, H. P. Wang, H. Grutzmacher, D. Wang, C. Y. Su, *Small* **2016**, *12*, 5702-5709.
50. M. Zeng, Z. Chai, X. Deng, Q. Li, S. Feng, J. Wang, D. Xu, *Nano Research* **2016**, *9*, 2729-2734.
51. G. Li, H. Kobayashi, J. M. Taylor, R. Ikeda, Y. Kubota, K. Kato, M. Takata, T. Yamamoto, S. Toh, S. Matsumura, H. Kitagawa, *Nat Mater* **2014**, *13*, 802-806.
52. Y. Chen, O. Sakata, Y. Nanba, L. S. R. Kumara, A. Yang, C. Song, M. Koyama, G. Li, H. Kobayashi, H. Kitagawa, *Communications Chemistry* **2018**, *1*, 61.
53. K. Pechstedt, T. Whittle, J. Baumberg, T. Melvin, *J Phys Chem C* **2010**, *114*, 12069-12077.
54. C. Galland, Y. Ghosh, A. Steinbruck, M. Sykora, J. A. Hollingsworth, V. I. Klimov, H. Htoon, *Nature* **2011**, *479*, 203-207.
55. Y. Zhao, C. Riemersma, F. Pietra, R. Koole, M. Donega Cde, A. Meijerink, *ACS Nano* **2012**, *6*, 9058-9067.
56. X. H. Ji, D. Copenhaver, C. Sichmeller, X. G. Peng, *J. Am. Chem. Soc.* **2008**, *130*, 5726-5735.
57. T. Uematsu, E. Shimomura, T. Torimoto, S. Kuwabata, *The Journal of Physical Chemistry C* **2016**, *120*, 16012-16023.
58. Y. Chen, J. Vela, H. Htoon, J. L. Casson, D. J. Werder, D. A. Bussian, V. I. Klimov, J. A. Hollingsworth, *J. Am. Chem. Soc.* **2008**, *130*, 5026-5027.
59. K. S. Park, Z. Ni, A. P. Cote, J. Y. Choi, R. Huang, F. J. Uribe-Romo, H. K. Chae, M. O'Keeffe, O. M. Yaghi, *Proc Natl Acad Sci U S A* **2006**, *103*, 10186-10191.
60. J. Cravillon, R. Nayuk, S. Springer, A. Feldhoff, K. Huber, M. Wiebcke, *Chem. Mater.* **2011**, *23*, 2130-2141.
61. C. M. Johnson, K. M. Pate, Y. Shen, A. Viswanath, R. Tan, B. C. Benicewicz, M. A. Moss, A. B. Greytak, *J. Colloid Interface Sci.* **2015**, *458*, 310-314.
62. T. Uematsu, *Electrochemistry* **2017**, *85*, 543-551.
63. P. Maity, T. Debnath, H. N. Ghosh, *The Journal of Physical Chemistry C* **2015**, *119*, 26202-26211.
64. K. Boldt, N. Kirkwood, G. A. Beane, P. Mulvaney, *Chem. Mater.* **2013**, *25*, 4731-4738.

65. Q. Liu, J. M. Yang, L. N. Jin, W. Y. Sun, *Chemistry* **2014**, *20*, 14783-14789.
66. G. Boschloo, L. Haggman, A. Hagfeldt, *J. Phys. Chem. B* **2006**, *110*, 13144-13150.
67. M. C. So, G. P. Wiederrecht, J. E. Mondloch, J. T. Hupp, O. K. Farha, *Chem Commun (Camb)* **2015**, *51*, 3501-3510.
68. X. Li, J. Yu, D. J. Gosztola, H. C. Fry, P. Deria, *J. Am. Chem. Soc.* **2019**, *141*, 16849-16857.
69. X. Zhang, W. Wang, Z. Hu, G. Wang, K. Uvdal, *Coord. Chem. Rev.* **2015**, *284*, 206-235.
70. Q. Zhang, C. Zhang, L. Cao, Z. Wang, B. An, Z. Lin, R. Huang, Z. Zhang, C. Wang, W. Lin, *J. Am. Chem. Soc.* **2016**, *138*, 5308-5315.
71. L. H. Cao, H. Y. Li, H. Xu, Y. L. Wei, S. Q. Zang, *Dalton Trans* **2017**, *46*, 11656-11663.
72. M. Gutierrez, M. Lopez-Gonzalez, F. Sanchez, A. Douhal, *Phys. Chem. Chem. Phys.* **2017**, *19*, 17544-17552.
73. Y. Yang, M. Ishida, Y. Yasutake, S. Fukatsu, C. Fukakusa, M. A. Morikawa, T. Yamada, N. Kimizuka, H. Furuta, *Inorg. Chem.* **2019**, *58*, 4647-4656.
74. M. Li, Z. Zheng, Y. Zheng, C. Cui, C. Li, Z. Li, *ACS Appl Mater Interfaces* **2017**, *9*, 2899-2905.
75. A. R. Clapp, I. L. Medintz, H. Mattoussi, *Chemphyschem* **2006**, *7*, 47-57.
76. X. Liu, J. Qiu, *Chem. Soc. Rev.* **2015**, *44*, 8714-8746.
77. S. Melle, O. G. Calderón, M. Laurenti, D. Mendez-Gonzalez, A. Egatz-Gómez, E. López-Cabarcos, E. Cabrera-Granado, E. Díaz, J. Rubio-Retama, *The Journal of Physical Chemistry C* **2018**, *122*, 18751-18758.
78. L. Protesescu, S. Yakunin, M. I. Bodnarchuk, F. Krieg, R. Caputo, C. H. Hendon, R. X. Yang, A. Walsh, M. V. Kovalenko, *Nano Lett.* **2015**, *15*, 3692-3696.
79. J. Song, T. Fang, J. Li, L. Xu, F. Zhang, B. Han, Q. Shan, H. Zeng, *Adv. Mater.* **2018**, *30*, e1805409.
80. Z. Pan, H. Rao, I. Mora-Sero, J. Bisquert, X. Zhong, *Chem. Soc. Rev.* **2018**, *47*, 7659-7702.
81. T. Kang, K. Um, J. Park, H. Chang, D. C. Lee, C.-K. Kim, K. Lee, *Sensors and Actuators B: Chemical* **2016**, *222*, 871-878.
82. A. Loiudice, S. Saris, E. Oveisi, D. T. L. Alexander, R. Buonsanti, *Angew. Chem. Int. Ed. Engl.* **2017**, *56*, 10696-10701.
83. Y. Liu, F. Li, Q. Liu, Z. Xia, *Chem. Mater.* **2018**, *30*, 6922-6929.
84. B. Mashford, J. Baldauf, T. L. Nguyen, A. M. Funston, P. Mulvaney, *J. Appl. Phys.* **2011**, *109*, 094305.
85. H. Sun, Z. Yang, M. Wei, W. Sun, X. Li, S. Ye, Y. Zhao, H. Tan, E. L. Kynaston, T. B. Schon, H. Yan, Z. H. Lu, G. A. Ozin, E. H. Sargent, D. S. Seferos, *Adv. Mater.* **2017**, *29*, 1701153.
86. J. Ko, B. G. Jeong, J. H. Chang, J. F. Joung, S. Y. Yoon, D. C. Lee, S. Park, J. Huh, H. Yang, W. K. Bae, S. G. Jang, J. Bang, *Npg Asia Materials* **2020**, *12*, 19.
87. K. Kumagai, T. Uematsu, T. Torimoto, S. Kuwabata, *CrystEngComm* **2019**, *21*, 5568-5577.
88. S. Jin, H. J. Son, O. K. Farha, G. P. Wiederrecht, J. T. Hupp, *J. Am. Chem. Soc.* **2013**, *135*, 955-958.
89. J. Kwak, W. K. Bae, D. Lee, I. Park, J. Lim, M. Park, H. Cho, H. Woo, D. Y. Yoon, K. Char, S. Lee, C. Lee, *Nano Lett.* **2012**, *12*, 2362-2366.
90. A. Ranft, S. B. Betzler, F. Haase, B. V. Lotsch, *Crystengcomm* **2013**, *15*, 9296-9300.
91. S. R. Venna, J. B. Jasinski, M. A. Carreon, *J. Am. Chem. Soc.* **2010**, *132*, 18030-18033.
92. C. E. Rowland, I. Fedin, H. Zhang, S. K. Gray, A. O. Govorov, D. V. Talapin, R. D. Schaller, *Nat Mater* **2015**, *14*, 484-489.
93. V. Stavila, A. A. Talin, M. D. Allendorf, *Chem. Soc. Rev.* **2014**, *43*, 5994-6010.
94. K. F. Chou, A. M. Dennis, *Sensors (Basel)* **2015**, *15*, 13288-13325.
95. R. E. Treharne, A. Seymour-Pierce, K. Durose, K. Hutchings, S. Roncallo, D. Lane, *J Phys Conf Ser* **2011**, *286*, 012038.
96. M. Debenham, *Appl. Opt.* **1984**, *23*, 2238.
97. C. Chen, C. Midelet, S. Bhuckory, N. Hildebrandt, M. H. V. Werts, *The Journal of Physical Chemistry C* **2018**, *122*, 17566-17574.
98. M. Noh, T. Kim, H. Lee, C.-K. Kim, S.-W. Joo, K. Lee, *Colloids and Surfaces A:*

Physicochemical and Engineering Aspects **2010**, *359*, 39-44.
99. N. Reitinger, A. Hohenau, S. Köstler, J. R. Krenn, A. Leitner, *physica status solidi (a)* **2011**, *208*, 710-714.
100. U. T. D. Thuy, P. T. Thuy, N. Q. Liem, L. Li, P. Reiss, *Appl. Phys. Lett.* **2010**, *96*, 073102.
101. H. Sahoo, *Journal of Photochemistry and Photobiology C: Photochemistry Reviews* **2011**, *12*, 20-30.
102. T. Franzl, T. A. Klar, S. Schietinger, A. L. Rogach, J. Feldmann, *Nano Lett.* **2004**, *4*, 1599-1603.
103. C. Y. Chen, C. T. Cheng, C. W. Lai, P. W. Wu, K. C. Wu, P. T. Chou, Y. H. Chou, H. T. Chiu, *Chem Commun (Camb)* **2006**, 263-265.
104. D. Kim, S. Okahara, M. Nakayama, Y. Shim, *Physical Review B* **2008**, *78*, 153301.
105. U. O. Seker, T. Ozel, H. V. Demir, *Nano Lett.* **2011**, *11*, 1530-1539.
106. R. Gui, A. Wan, H. Jin, *Analyst* **2013**, *138*, 5956-5964.
107. K. Zheng, K. Zidek, M. Abdellah, N. Zhu, P. Chabera, N. Lenngren, Q. Chi, T. Pullerits, *J. Am. Chem. Soc.* **2014**, *136*, 6259-6268.
108. P. Roy, G. Devatha, S. Roy, A. Rao, P. P. Pillai, *J Phys Chem Lett* **2020**, *11*, 5354-5360.
109. E. A. Jares-Erijman, T. M. Jovin, *Nat. Biotechnol.* **2003**, *21*, 1387-1395.
110. F. T. Chan, C. F. Kaminski, G. S. Kaminski Schierle, *Chemphyschem* **2011**, *12*, 500-509.
111. D. P. Shepherd, K. J. Whitcomb, K. K. Milligan, P. M. Goodwin, M. P. Gelfand, A. Van Orden, *The Journal of Physical Chemistry C* **2010**, *114*, 14831-14837.
112. K. J. Whitcomb, D. P. Ryan, M. P. Gelfand, A. Van Orden, *The Journal of Physical Chemistry C* **2013**, *117*, 25761-25768.
113. D. P. Ryan, P. M. Goodwin, C. J. Sheehan, K. J. Whitcomb, M. P. Gelfand, A. Van Orden, *The Journal of Physical Chemistry C* **2018**, *122*, 4046-4053.
114. M. Lunz, A. L. Bradley, W. Y. Chen, V. A. Gerard, S. J. Byrne, Y. K. Gun'ko, V. Lesnyak, N. Gaponik, *Physical Review B* **2010**, *81*, 205316.
115. N. Liu, B. S. Prall, V. I. Klimov, *J. Am. Chem. Soc.* **2006**, *128*, 15362-15363.
116. A. Dhir, A. Datta, *The Journal of Physical Chemistry C* **2016**, *120*, 20125-20131.
117. C. Chen, B. Corry, L. Huang, N. Hildebrandt, *J. Am. Chem. Soc.* **2019**, *141*, 11123-11141.
118. M. Shahnawaz Khan, M. Khalid, M. Shahid, *Materials Advances* **2020**, *1*, 1575-1601.
119. K. H. Lee, J. H. Lee, H. D. Kang, B. Park, Y. Kwon, H. Ko, C. Lee, J. Lee, H. Yang, *ACS Nano* **2014**, *8*, 4893-4901.
120. F. Wu, Y. Zhang, Z. Zhang, G. Li, M. Li, X. Lan, T. Sun, Y. Jiang, *Langmuir* **2017**, *33*, 7124-7129.
121. X. G. Wang, Q. Cheng, Y. Yu, X. Z. Zhang, *Angew. Chem. Int. Ed. Engl.* **2018**, *57*, 7836-7840.
122. Y. E. Panfil, D. Shamalia, J. Cui, S. Koley, U. Banin, *J. Chem. Phys.* **2019**, *151*, 224501.
123. J. Liu, Y. Liu, X. Yang, K. Wang, Q. Wang, H. Shi, L. Li, *Anal. Chem.* **2013**, *85*, 11121-11128.
124. H. Kashida, H. Kawai, R. Maruyama, Y. Kokubo, Y. Araki, T. Wada, H. Asanuma, *Communications Chemistry* **2018**, *1*, 91.

Acknowledgements

The author would like to express his sincerest gratitude to Prof. Dr. Susumu Kuwabata at Department of Applied Chemistry, Graduate School of Engineering, Osaka University who provided continuous guidance, valuable suggestions, accurate feedback, and warm encouragement throughout this work. The author would like to thank Prof. Dr. Hiroshi Uyama and Prof. Dr. Akinori Saeki, at Department of Applied Chemistry, Graduate School of Engineering, Osaka University for their careful reviews and valuable suggestions.

The author also would like to express his special thanks to Associate Prof. Dr. Taro Uematsu at Department of Applied Chemistry, Graduate School of Engineering, Osaka University, who provide enthusiastic guidance, invaluable feedback, fruitful discussion and warm encouragement throughout this work. The author would like to show his deeply appreciation to Associate Prof. Dr. Tetsuya Tsuda at Department of Applied Chemistry, Graduate School of Engineering, Osaka University, for his helpful support and kind feedback throughout research activity. The author is deeply grateful to Dr. Hajime Matsumoto at Department of Energy and Environment, Research Institute of Electrochemical Energy, National Institute of Advanced Industrial Science and Technology, his expert advice and warm encouragement. The author is deeply grateful to Prof. Dr. Paul Mulvaney and Dr. Nicholas Kirkwood at Nanoscience laboratory, School of Chemistry, the University of Melbourne, for their valuable discussion, accurate guidance and heartfelt support over the three months spent in Australia. The author would like to express sincere gratitude to Ms. Miwa Shimizu, Ms. Yasuko Ueda and Special-appointment Prof. Dr. Kenji Iijima for their great cooperation in the activities in the Interactive Materials Science Cadet Program

The author would like to appreciate Dr. Eiko Mochizuki, Ms. Michiko Ebukuro and Ms. Miyuki Takahama for helping with the office works in the laboratory. The author is grateful to Dr. Kazuki Iwasaki, Dr. Reiko Izumi, Dr. Hiroshi Tenmyo, Dr. Kei Hosoya and Dr. Yao Yu, who are respected seniors, for their helpful comments and encouragements. The author is also grateful to all members of both Applied Electrochemistry Laboratory and Nanoscience Laboratory for their warm support and invaluable memories. The author gratefully appreciates Interactive Materials Science Cadet Program and Japan Society for the Promotion of Science for their scholarship supports.

Finally, the author would like to express his sincere gratitude to his father Yuichi Kumagai, his mother Chiaki Kumagai, his younger sister Sachiho Kumagai, his grandfather Masaru Ito, his grandmother Akiko Ito, his uncle Kazuya Ito for their hearty support and warm encouragements.

Kohei Kumagai
March, 2021